







Université du Québec  
à Rimouski

**Enregistrements sédimentaires associés à la dynamique de la  
calotte glaciaire Penny (Île de Baffin, Nunavut, Canada) au  
cours de l'Holocène tardif**

Mémoire présenté  
dans le cadre du programme de maîtrise en océanographie  
en vue de l'obtention du grade de maître ès sciences

PAR

© María-Emilia Rodríguez-Cuicas

Juin 2022



**Composition du jury :**

**André Pellerin, examinateur interne, ISMER-UQAR**

**Matt O'Regan, examinateur externe, Stockholm University**

**Jean-Carlos Montero-Serrano, directeur de recherche, ISMER-UQAR**

**Guillaume St-Onge, codirecteur de recherche, ISMER-UQAR**

**Alexandre Normandeau, codirecteur de recherche, Commission Géologique du Canada**

Dépôt initial le [06-04-2022]

Dépôt final le [08-06-2022]

UNIVERSITÉ DU QUÉBEC À RIMOUSKI  
Service de la bibliothèque

Avertissement

La diffusion de ce mémoire ou de cette thèse se fait dans le respect des droits de son auteur, qui a signé le formulaire « *Autorisation de reproduire et de diffuser un rapport, un mémoire ou une thèse* ». En signant ce formulaire, l'auteur concède à l'Université du Québec à Rimouski une licence non exclusive d'utilisation et de publication de la totalité ou d'une partie importante de son travail de recherche pour des fins pédagogiques et non commerciales. Plus précisément, l'auteur autorise l'Université du Québec à Rimouski à reproduire, diffuser, prêter, distribuer ou vendre des copies de son travail de recherche à des fins non commerciales sur quelque support que ce soit, y compris Internet. Cette licence et cette autorisation n'entraînent pas une renonciation de la part de l'auteur à ses droits moraux ni à ses droits de propriété intellectuelle. Sauf entente contraire, l'auteur conserve la liberté de diffuser et de commercialiser ou non ce travail dont il possède un exemplaire.





## **REMERCIEMENTS**

Tout d'abord, je souhaite remercier mon directeur de recherche, Jean-Carlos Montero-Serrano pour la confiance et son aide tout au long de ce processus et pour l'exemple constant de travail et d'excellence. Je remercie également mes co-directeurs de recherche, Guillaume St-Onge et Alexandre Normandeau pour leur implication dans le projet et pour éclairer ma démarche. Je voudrais aussi remercier à Matt O'Regan pour leur contribution à la révision du mémoire.

Merci au capitaine et à l'équipage du NGCC Amundsen pour les trois incroyables expéditions en Arctique. Merci à mes amies Anne Corminboeuf, Jade Brossard et au professeur André Pellerin pour l'esprit d'équipe et pour les belles expériences passées en mer.

Merci aussi à tous les techniciens et techniciennes de laboratoire ; Quentin Beauvais, Dominique Lavallée, et Claude Belzile pour la formation et l'aide à la manipulation des instruments de laboratoire à l'ISMER.

Un grand merci à mes amis vénézuéliens Omnain Kutos, Yetzy Ramírez et Iliana Aguilar pour leur soutien, mots d'encouragement et pour m'avoir fait me sentir proche de chez moi. Finalement, un gros merci à mes parents, mes frères et mon époux Asdrúbal Díaz pour être toujours à mes côtés, quelles que soient les circonstances.

## AVANT-PROPOS

Ce mémoire de maîtrise est présenté en trois parties : une introduction générale rédigée en français, d'un chapitre principal rédigé en anglais sous la forme d'article scientifique en prévision d'être soumis pour publication à la revue internationale « *Journal of Quaternary Science* », et une brève conclusion générale rédigée en français.

L'article présenté dans ce mémoire de maîtrise : Rodríguez-Cuicas, M-E., Montero-Serrano, J.-C., St-Onge, G., Normandeau, A. *Sedimentary records associated with the dynamics of the Penny Ice Cap (Baffin Island, Nunavut, Canada) during the Late Holocene*, et a été rédigé par moi-même avec la supervision de Jean-Carlos Montero-Serrano et Guillaume St-Onge de l'ISMER-UQAR et d'Alexandre Normandeau de la Commission Géologique du Canada. En tant que premier auteur, ma contribution fut la réalisation des analyses de laboratoire des différents traceurs minéralogiques, géochimiques et paléomagnétiques et la rédaction de l'article. Jean-Carlos Montero-Serrano, Guillaume St-Onge et Alexandre Normandeau ont fourni l'idée originale, l'implémentation du développement de la méthode et la formation nécessaire pour réaliser les analyses de laboratoires et ont contribué à la rédaction et révision de l'article. Quentin Beauvais (ISMER-UQAR) à effectuer les analyses de propriétés physiques des carottes, Pascal Rioux (ISMER-UQAR) et Michael E. Ketterer (Northern Arizona University) ont fait les mesures de  $^{210}\text{Pb}$  et  $^{239+240}\text{Pu}$  sur la carotte 05BC, respectivement, alors que les mesures de  $^{210}\text{Pb}$  sur la carotte 12TWC ont été effectués par Vladislav Carnero-Bravo au Geotop. Les datations au  $^{14}\text{C}$  ont été effectuées à Alfred Wegener Institute (AWI-MICADAS) et KECK carbon cycle AMS facility.

Au cours ma maîtrise, j'ai eu l'opportunité de présenter les principaux résultats de mon projet de recherche lors de divers congrès nationaux et internationaux :

- Rodríguez-Cuicas, M.-E., Montero-Serrano, J.-C., St-Onge, G., Normandeau, A., 2020. Enregistrements sédimentaires associés à la dynamique de la calotte glaciaire Penny (Île de Baffin, Nunavut, Canada) au cours de l'Holocène. Réunion Scientifique Annuelle de Québec-Océan, 9 au 11 Mars Château Mont-Sainte-Anne, Beaupré, Canada. (Affiche).
- Rodríguez-Cuicas, M.-E., Montero-Serrano, J.-C., St-Onge, G., Normandeau, A., 2020. Dynamique sédimentaire holocène de la calotte glaciée Penny (Île de Baffin, Nunavut, Canada). Congrès annuel du Geotop, 20 au 22 Mars. Annulé à cause de la pandémie de COVID-19. (Affiche).
- Rodríguez-Cuicas, M.-E., Montero-Serrano, J.-C., St-Onge, G., Normandeau, A., 2020. Enregistrement sédimentaire associé à la dynamique de la calotte glaciaire Penny (Île de Baffin, Canada) au cours de l'Holocène tardif. Journées Climat et Impacts 2020, 23-25 Novembre, événement en ligne. (Oral).
- Rodríguez-Cuicas, M.-E., Montero-Serrano, J.-C., St-Onge, G., Normandeau, A., 2020. Sediment composition and lithofacies along the Coronation Fjord (Baffin Island, Nunavut, Canada). International Arctic Change Conference, 7-10 Decembre, événement en ligne. (Affiche).
- Rodríguez-Cuicas, M.-E., Montero-Serrano, J.-C., St-Onge, G., Normandeau, A., 2021. Sédimentation glaciomarine le long du fjord Coronation (Île de Baffin, Nunavut, Canada) au cours de l'Holocène tardif. Réunion Scientifique Annuelle de Québec-Océan, 8 -11 février, événement en ligne. (Oral).
- Rodríguez-Cuicas, M.-E., Montero-Serrano, J.-C., St-Onge, G., Normandeau, A., 2021. Late Holocene dynamics of the Penny Ice Cap reconstructed from two sediment cores of the Coronation Fjord (Baffin Island, Nunavut, Canada). Congrès annuel du Geotop, 16 au 18 Mars. Événement en ligne. (Affiche).

-Rodríguez-Cuicas, M.-E., Montero-Serrano, J-C., St-Onge, G., Normandeau, A., 2021. A 400-year record of glaciomarine sedimentation associated with the dynamics of the Penny Ice Cap (Baffin Island, Nunavut, Canada). Annual EGU General Assembly, 19-30 Avril. Événement en ligne. (Oral & Affiche).

J'ai également eu l'opportunité d'embarquer à bord du NGCC Amundsen à l'été 2018, 2019 et 2021 dans l'Arctique canadien, et à l'hiver 2020 dans l'estuaire du Saint-Laurent, pour fournir mon aide pour les opérations de carottage et pour les échantillonnages de rivières et de glaciers. J'ai aussi donné formations aux étudiants et stagiaires dans l'ouverture et la description des carottes sédimentaires, la préparation d'échantillons et l'analyse minéralogique et chimique des sédiments marins.



## RÉSUMÉ

Deux séquences sédimentaires composites échantillonnées dans l'environnement glaciaire proximal (12CS) et distal (02CS) du fjord Coronation (île de Baffin, Nunavut, Canada) ont été étudiées à l'aide de propriétés physiques, granulométriques, minéralogiques, géochimiques et magnétiques afin de reconstituer les changements à long terme dans les transferts de sédiments de la calotte glaciaire Penny (CGP) liés à la variabilité climatique de l'Holocène tardif. Les chronologies des carottes ont été établies par des analyses au plomb-210 ( $^{210}\text{Pb}$ ), au plutonium 239 et 240 ( $^{239+240}\text{Pu}$ ), au radiocarbone ( $^{14}\text{C}$ ) et paléomagnétiques. Les signatures minéralogiques révèlent un apport détritique homogène avec une composition caractéristique du batholite de Cumberland. Les traceurs détritiques et les analyses sédimentologiques révèlent que les couches déposées rapidement (RDL) sont fréquentes dans l'environnement glaciaire proximal en raison de l'avancé des glaciers pendant les périodes de croissance, des déversements d'eau de fonte glaciaire et/ou des perturbations des icebergs sur le fond marin pendant le vêlage. Les RDL dans l'environnement glaciaire distal impliquent la décharge de crues météorologiques en provenance des trois fjords adjacents (Nord de Pangnirtung, Coronation et Maktak). Les sédiments stratifiés avec des débris délestés par les icebergs (IRD) enregistrés pendant la Petit Âge Glaciaire dans la carotte 12CS révèlent que les conditions plus froides ont favorisé la croissance des glaciers, des épisodes successifs de panaches turbides d'eau de fonte pendant la saison de printemps/été et une augmentation dans le vêlage d'icebergs dans le fjord Coronation. L'augmentation du taux de sédimentation ( $>0.9 \text{ cm an}^{-1}$ ), les variations brusques de la minéralogie et de la taille des grains, les faibles proportions d'IRD et les fréquences élevées de RDL observées dans les deux carottes depuis 1850 CE reflètent le retrait accéléré du glacier Coronation en réponse au réchauffement climatique moderne. Des tendances similaires observées entre les traceurs détritiques des carottes 12CS et 02CS et les taux de fonte enregistrés dans la CGP, l'enregistrement de l'oscillation multidécennale de l'Atlantique et les anomalies de la température de l'air à la surface de l'Arctique, suggèrent une forte connectivité entre les variations de la température atmosphérique et la dynamique de la CGP au cours des 600 dernières années.

Mots clés : Île de Baffin; péninsule de Cumberland; calotte glaciaire Penny; Holocène tardif; sédimentologie; minéralogie; géochimie; dynamique des glaciers; dynamique des sédiments.

## ABSTRACT

Two composite sedimentary sequences sampled in the ice-proximal (12CS) and ice-distal (02CS) areas of Coronation Fjord (Baffin Island, Nunavut, Canada) were investigated. Physical, grain size, mineralogical, geochemical, and magnetic properties were used to reconstruct long-term changes in sediment transfers from the Penny Ice Cap (PIC) related to late Holocene climate variability. The core chronologies were established by lead-210 ( $^{210}\text{Pb}$ ), plutonium 239 and 240 ( $^{239+240}\text{Pu}$ ), radiocarbon ( $^{14}\text{C}$ ) and paleomagnetic analyses. The mineralogical signatures reveal a homogeneous detrital input with a composition characteristic of the Cumberland batholith. Detrital proxies and physical and sedimentological analyses reveal that rapidly deposited layers (RDLs) are frequent in ice-proximal settings because of glacier thrust during growth periods, glacial meltwater stream discharges and/or iceberg disturbances on the fjord floor during calving. RDLs in ice-distal settings involve the release of large outburst floods coming from three fjords (North of Pangnirtung, Coronation and Maktak). Laminated sediments with ice-rafted debris (IRD) throughout the Little Ice Age (LIA) interval in core 12CS reveal that colder LIA conditions promoted glacier growth, successive episodes of turbid hyperpycnal meltwater plumes during spring/summer and iceberg calving activity in Coronation Fjord. Sedimentation rate increases ( $>0.9 \text{ cm yr}^{-1}$ ), abrupt mineralogical and grain size proxy variations, low IRD proportions and high frequencies of RDLs observed in the two cores since 1850 CE correspond to the accelerated Coronation Glacier retreat to its present-day extent in response to modern warming. Similar trends between the detrital proxies of cores 12CS and 02CS and melt features recorded in the PIC, Atlantic Multidecadal Oscillation record and Arctic surface air temperature anomalies suggest high connectivity between atmospheric and sea surface temperature variations and PIC dynamics during the last 600 years.

Keywords: Baffin Island; Cumberland Peninsula; Penny Ice Cap; late Holocene; sedimentology, mineralogy; geochemistry; glacier dynamics; sediment dynamics.



## TABLE DES MATIÈRES

REMERCIEMENTS.....	vii
AVANT-PROPOS .....	viii
RÉSUMÉ .....	xii
ABSTRACT.....	xiii
TABLE DES MATIÈRES .....	xv
LISTE DES TABLEAUX .....	xvii
LISTE DES FIGURES .....	xviii
LISTE DES ABRÉVIATIONS, DES SIGLES ET DES ACRONYMES .....	xxi
INTRODUCTION GÉNÉRALE .....	1
1. CONTEXT SCIENTIFIQUE ET PROBLEMATIQUE.....	1
2. OBJECTIFS DE RECHERCHE ET APPROCHE MÉTHODOLOGIQUE .....	4
3. PRÉSENTATION DE LA ZONE D'ETUDE .....	6
3.1 Circulation océanique.....	7
3.2 Sédimentation et géologie .....	8
CHAPITRE 1 ENREGISTREMENTS SÉDIMENTAIRES ASSOCIÉS À LA DYNAMIQUE DE LA CALOTTE GLACIAIRE PENNY (ÎLE DE BAFFIN, NUNAVUT, CANADA) AU COURS DE L'HOLOCÈNE TARDIF .....	10
1. <b>Introduction</b> .....	10
2. <b>Regional setting</b> .....	13
2.1 Geology, physiography and fjord circulation .....	13
2.2 Sedimentation .....	15
3. <b>Materials and methods</b> .....	16
3.1 Sediment cores.....	16
3.2 Laboratory analyses.....	17
3.2.1 Multisensor Core Longer analyses .....	17
3.2.2 Grain-size and end member modeling analyses .....	17
3.2.3 Quantitative bulk mineralogy .....	18

3.3	Chronology .....	19
3.3.1	$^{210}\text{Pb}$ and $^{239+240}\text{Pu}$ analyses .....	19
3.3.2	Paleomagnetic analyses .....	19
3.3.3	Radiocarbon analyses .....	20
3.3.4	Age modelling .....	22
3.4	Statistical approach.....	23
4.	<b>Results and interpretations.....</b>	23
4.1	General grain-size, mineralogical and geochemical characteristics.....	23
4.2	Rapidly deposited layers (RDL) and magnetic properties .....	26
4.3	Chronology .....	29
4.4	Sedimentary units .....	32
4.4.1	Core 12CS .....	32
4.4.2	Core 02CS .....	35
5.	<b>Discussion .....</b>	36
5.1	Sediment provenance.....	36
5.2	Sedimentological interpretation of rapidly deposited layers .....	37
5.3	Depositional processes during the Late Holocene.....	40
6.	<b>Conclusions .....</b>	46
7.	<b>Acknowledgments.....</b>	48
CONCLUSION GÉNÉRALE.....		49
ANNEXES .....		53
RÉFÉRENCES BIBLIOGRAPHIQUES.....		60

## **LISTE DES TABLEAUX**

Table 1. Location of the sampling sites, water depth, and length of the cores used in this study. ....	16
Table 2. Accelerator mass spectrometry (AMS) radiocarbon dates and calibrations for cores 12PC, 05BC and 02PC, with different reservoir ages. ....	21
Table 3. Paleomagnetic chronostratigraphical markers (tie points) based on the correlation between the 12CS and 02CS cores presented in this study, with other paleomagnetic records (Nettilling Lake, Beaudoin et al. 2016) and geomagnetic field models (GUMF1, Jackson et al., 2000; and CALS3k.4, Korte and Constable, 2011) calculated for the study area.....	32

## LISTE DES FIGURES

<p>Figure 1. (A) Localisation de la calotte glaciaire Penny sur l'île de Baffin. Les flèches représentent le courant relativement chaud de l'ouest du Groenland (WGC), et le courant froid de l'île de Baffin (BBC), (B) sites de collecte des carottes 05BC, 02PC/TWC (étoile rouge), et les carottes 12PC/TWC (étoile jaune).....4</p> <p>Figure 2. Cartes du bilan de masse des glaciers et calottes glaciaires de l'Île de Baffin et de la calotte glaciaire Penny (A), moyennées pour les périodes 1958–1995 (B) et 1996–2015 (C). SMB = bilan de masse de la surface (Nöel et al., 2018).....7</p> <p>Figure 3. Carte géologique de la péninsule Cumberland sur l'île de Baffin (adapte de Dyke et al., 1982). .....9</p> <p>Figure 4. Regional geology and location of the Penny Ice Cap (PIC) on Baffin Island. The arrows represent the relatively warm West Greenland Current (WGC) and the cold Baffin Island Current (BIC). Abbreviations are as follows: Broughton Trough (BT), Barnes Ice Cap (BaIC), Divide Ice Cap (DIC), Naqsaq Glacier (NG), and Nettilling Lake (NL).....12</p> <p>Figure 5. (A-C) MODIS satellite image from 11 May 2020 showing a snapshot of Maktak, Coronation, and North Pangnirtung Fjords, as well as the bathymetry and the location of the cores in this study (source: NASA Worldview). (D-E) Sub-bottom profiles across coring stations. S= sandur surface; GL= grounding line.....14</p> <p>Figure 6. (A) Frequency curves of raw grain size data for cores 12CS and (B) 02CS; (C) boxplot of the grain size distribution (%) for both cores. .....24</p> <p>Figure 7. Results of mineralogical and chemical composition for cores 12CS and 02CS. (A) Boxplot of the distribution of the main minerals (wt.%); (B) boxplot of the chemical composition distribution (%); Note that the relative intensities of pXRF sensor were converted to percentage (1%=10000 ppm); (C) biplots of the PCA of the bulk mineralogical data; (D) biplots of the PCA of geochemical data. .....25</p> <p>Figure 8. Downcore variations in cores 12PC and 02PC, showing X-CT images, high-resolution core photography, grain size parameters, IRD counts (&gt;2 mm fraction), wet bulk density, magnetic susceptibility (kLF) and magnetic properties (inclination, MAD, MDF and kARM/kLF). RDLs are numbered</p>	<p>.....4</p> <p>.....7</p> <p>.....9</p> <p>.....12</p> <p>.....14</p> <p>.....24</p> <p>.....25</p>
--	---

and highlighted in yellow. The vertical red line delineates a MAD value of 5°. The black vertical line represents the median of the data for each proxy. ....	28
Figure 9. X-CT scan image, high-resolution core photography and grain size trend (D90) for the fining-upward turbidite and hyperpycnal deposit sequences. ....	29
Figure 10. Comparison of the inclination values from sediment cores (D) 12PC and (J) 02PC compared to (A, G) Nettilling Lake (Beaudoin et al., 2016), (B, H) the GUMF1 (Jackson et al., 2000), and (C, I) CALS3k.4 (Korte and Constable, 2011) geomagnetic field models. (D, J) Composite age model using 210Pb, 239+240Pu, and 14C ages and paleomagnetic tie points. The Bayesian age-depth model was constructed using the R package BACON (Blaauw and Christen, 2011). The red dashed line shows the best age model, and the gray shading represents the chronological uncertainties (95% confidence interval). Black arrows show the RDL ages. (E, J) Estimated sedimentation rates in cm.a-1.....	31
Figure 11. X-CT scan image, high-resolution core photography, grain size distribution, D90, mean size of sortable silt fraction SS, mineralogical and chemical tracers and sedimentary units of cores 12CS and 02CS. RDLs are numbered and highlighted in yellow. The black vertical line represents the median of the data for each proxy. Black boxes indicate sections of the sortable silt record that do not pass the reliability test of a downcore correlation coefficient>0.5 between SS and SS% (McCave and Andrews 2019a).....	33
Figure 12. Summary of the physical characteristics, average grain size and interpretation of the depositional processes of lithofacies identified in cores 12CS and 02CS. ....	34
Figure 13. Quartz (Qz) – chlorite+biotite (Chl+Bt) – K-feldspar+Plagioclase (Kfs+Pl) ternary plot, including sediment samples of cores 12CS and 02CS. The Coronation, Maktak and Pangnirtung mineralogical data are from Andrews et al. (2018) and Andrews (2019). .....	37
Figure 14. Co Comparison of detrital proxies used in this study for cores 12CS and 02CS during the Late Holocene with paleoenvironmental proxies. (A) Thickness of RDL (blue bars: 12CS; red bars: 02CS); (B-C) Chl+Bt/Kfs+Pl; (D-E) log(Zr/Zn), (F) IRD count in core 12CS (>2 mm); (G) Ti (kcps) measured in core sediment from Nettilling Lake (Beaudoin et al., 2016); (H) melt feature (MF) anomalies from the Penny Ice Cap (PIC; Fisher et al., 1998); (I) reconstructed Atlantic Multidecadal Oscillation (AMO) index (Lapointe et al., 2020); (J) surface air temperature (SAT) anomalies in the Arctic (Kaufman et al., 2009). (K) inferred ice margin elevation of the Divide Ice Cap (DIC) located close to the Coronation Fjord (Pendleton et al., 2017). The position of the DIC margin was interpreted from radiocarbon ages of	

plants (black circles), aerial photography (triangle), and observed 2015 position (circle). The Neoglacial maximum DIC extent is also shown (square). asl = above sea level. The black vertical line represents the median of the data for each proxy.....42

Figure 15. Comparison of the (A) historical air temperature data of Pangnirtung Nunavut (source: <https://climat.meteo.gc.ca>) and (B) melt feature (MF) anomalies from the Penny Ice Cap (PIC; Zdanowicz et al., 2012), with (C) Chl+Bt/Kfs+Pl, (D) log(Zr/Zn) profiles from core 05BC (top of 02CS). The horizontal line represents the median of the data for each proxy. The log(Zr/Zn) scale was inverted for better comparison with the other proxies. Note that the difference in the timing between of peaks of melt feature anomalies from the PIC and the sedimentary records can reflects uncertainties in the individual chronology methods and/or a lag of the sediment response .....43

Figure 16. Schematic models of sedimentary processes and environmental conditions in Coronation Fjord during (A) the LIA, in which colder conditions generated increased iceberg calving activity, increasing the concentration of IRD and turbidite deposits in an ice-proximal setting; successive episodes of high seasonal meltwater discharge resulted in outburst floods deposited in an ice-distal setting; and (B) MW, in which warmer conditions promote the input of glacial meltwater outwash, sediment-laden transport and turbid hyperpycnal flow formation in ice-proximal and ice-distal settings.....46

## **LISTE DES ABRÉVIATIONS, DES SIGLES ET DES ACRONYMES**

<b>AMO</b>	Atlantic Multidecadal Oscillation, Oscillation multidécennale de l'Atlantique.
<b>ASL</b>	Above sea level, au-dessus du niveau de la mer.
<b>BaIC</b>	Barnes Ice Cap, calotte glaciaire Barnes.
<b>BIC</b>	Baffin Island Current, Courant de l'île de Baffin.
<b>BT</b>	Broughton Trough, fosse de Broughton
<b>CAA</b>	Canadian Arctic Archipelago, Archipel Arctique Canadien.
<b>CCGS</b>	Coastal Canadian Guard Ship, navire de la Garde-Côtière canadienne.
<b>DIC</b>	Divide Ice Cap, calotte glaciaire Divide.
<b>IPCC</b>	Intergovernmental Panel on Climate Change, comité intergouvernemental sur le changement climatique.
<b>IRD</b>	Ice Rafted Debris, vêlage d'icebergs.
<b>IRM</b>	Isothermal Remanent Magnetization, aimantation isothermale rémanente.
<b>ISMER</b>	Institut des sciences de la mer de Rimouski.
<b>kLF</b>	Low field magnetic susceptibility, susceptibilité magnétique mesurée à champ faible.
<b>LGM</b>	Last Glacial Maximum, Dernier maximum glaciaire.
<b>LIA</b>	Little Ice Age, petit âge glaciaire.
<b>MDF<sub>NRM</sub></b>	Median Destructive Field of the Natural Remanent Magnetization, champs destructif médian de l'aimantation naturelle rémanente.
<b>MSCL</b>	Multi-Sensor Core Logger, banc de mesure à senseurs multiples.

<b>MW</b>	Modern Warming, réchauffement moderne
<b>NG</b>	Nasqsaq Glacier, glacier Nasqsaq.
<b>NL</b>	Nettilling Lake, lac Nettilling
<b>NRM</b>	Natural Remanent Magnetization, aimantation naturelle rémanente.
<b>PCA</b>	Principal component analysis, analyse en composantes principales.
<b>PIC</b>	Penny Ice Cap, calotte glaciaire Penny.
<b>RDL</b>	Rapidly deposited layers.
<b>SAT</b>	Surface air temperature, température de l'air en surface.
<b>SIRM</b>	Saturation Isothermal Remanent Magnetization, aimantation rémanente isothermale de saturation.
<b>SPG</b>	Subpolar gyre, gyre subpolaire.
<b>UQAR</b>	Université du Québec à Rimouski.
<b>WGC</b>	West Greenland Current, courant ouest groenlandais.
<b>XCT</b>	X-ray Computed Tomographic, radiographie à rayons X.
<b>XRD</b>	X-Ray diffraction, diffraction à rayons X.
<b>XRF</b>	X-ray fluorescence, fluorescence à rayons X.

## **INTRODUCTION GÉNÉRALE**

L'introduction générale de ce mémoire présente dans un premier temps la problématique du projet de recherche et une revue de littérature sur les enregistrements des conditions paléoclimatiques de l'Holocène sur l'île de Baffin. Dans un second temps, les objectifs de recherche, l'approche méthodologique et une présentation de la zone d'étude sont exposés.

### **1. CONTEXTE SCIENTIFIQUE ET PROBLEMATIQUE**

Les activités humaines ont eu un impact majeur sur le fonctionnement des géosystèmes. Après la révolution industrielle (1760 EC, ère commune), l'avènement des changements climatiques anthropiques a suscité l'intérêt de la communauté scientifique pour comprendre les conséquences de l'accélération du réchauffement climatique global. L'un des impacts les plus notables est lié à la cryosphère. En effet, l'augmentation de la température au niveau mondial (-0.6 à 1.2 °C entre 1980-2020 EC, IPCC, 2014 ; 2019) a eu un impact direct et néfaste sur le bilan de masse des principaux glaciers et calottes glaciaires du monde (ex. Kaser et al., 2006). La fonte de ces énormes masses de glace entraîne une hausse rapide du niveau marin eustatique. Bien que ces effets puissent actuellement être observés dans les régions polaires, la région arctique a été fortement sensible à ces changements (ex. Serreze et Francis, 2006 ; Cohen et al., 2014). Dans l'ensemble de l'Arctique, les températures augmentent beaucoup plus rapidement que la moyenne mondiale ; par exemple, entre 1880 et 2012, l'Arctique s'est réchauffé d'environ 3,5 °C, contre 0,85 °C pour l'ensemble de la Terre (1880-2012 ; IPCC, 2014 ; Overland et al., 2016). Cette différence est due à la transformation directe de l'énergie solaire en réchauffement atmosphérique à hautes latitudes, tandis qu'aux basses latitudes le processus d'évaporation domine (McBean et al., 2005 ; Serreze et Francis,

2006). Cela se traduit notamment par la fonte de la glace de mer, des glaciers et des calottes glaciaires de cette région à un rythme alarmant (IPCC, 2019).

Après le Groenland et l'Antarctique, l'archipel Arctique canadien (AAC) présente la plus grande zone de glaciers continentaux, avec une superficie d'environ 146 000 km<sup>2</sup> (Sharp et al., 2014). La plupart des glaciers se situe sur les îles d'Ellesmere, de Devon, d'Axel Heiberg, de Meighen, Baffin et Bylot (Noël et al., 2018). Des études récentes indiquent qu'entre 2006 et 2009, les glaciers de cette région ont perdu de la glace à un taux de  $92 \pm 12$  Gt an<sup>-1</sup> et les projections indiquent que le taux d'augmentation du niveau marin global sera de  $0,35 \pm 0,24$  mm an<sup>-1</sup> à la fin du 21<sup>e</sup> siècle (Lenaerts et al., 2013), faisant de cette région l'un des plus grands contributeurs à l'élévation mondiale du niveau marin (Radic & Hock, 2010 ; Gardner et al., 2011 ; Harig & Simons, 2016 ; Noël et al., 2018). Plus précisément, les calottes glaciaires Barnes et Penny, sur l'Île de Baffin, sont considérées comme les derniers vestiges de l'Inlandsis laurentidien (Zdanowicz et al., 2012). La calotte glaciaire de Penny (CGP) est le corps de glace le plus au sud de l'AAC, ce qui la rend très sensible aux changements climatiques (Zdanowicz et al., 2012).

Bien que les grandes masses de glace de l'Arctique réagiraient au réchauffement climatique à des échelles de temps millénaires, principalement par une fonte accrue de la surface, les changements dans le flux de glace ne se produiraient qu'à des échelles de temps centenaires ou plus (Greve, 2000 ; Huybrechts et al., 1991). Cependant, les études publiées au cours des deux dernières décennies ont montré une réduction des délais de réponse des glaciers à réagir à un changement du bilan de masse (Joughin et al., 2010 ; Rignot et al., 2008 ; van den Broeke et al., 2009). En fait, on sait que certains des événements climatiques du dernier cycle glaciaire n'étaient pas synchrones, comme le moment de l'avancée maximale des glaciers à différentes latitudes (Hughes et Woodward, 2008, Clark et al., 2009), mais les causes restent inexpliquées. Pour répondre ces questions, il est nécessaire d'évaluer le synchronisme ou la relation entre différentes archives paléoclimatiques. Toutefois, il existe peu de données à haute résolution temporelle disponibles pour étudier la réponse à long terme

des glaciers de l'AAC aux changements climatiques et océanographiques (Miller et al., 2010).

Les enregistrements des conditions paléoclimatiques de l'Holocène sur l'île de Baffin ont été étudiés principalement à partir de carottes de glace (Fisher, 1998 ; Zdanowicz et al., 2012), de la télédétection (Van Wychen et al., 2015 ; Schaffer et al., 2017), et des sédiments lacustres (Briner et al., 2006 ; Thomas et Briner, 2009 ; Briner et al., 2009 ; Thomas 2011 ; Narancic et al., 2021). Il y a moins de clarté concernant la reconstruction des changements environnementaux passés dans les sédiments des fjords. Notamment, les fjords représentent la transition entre l'environnement terrestre et l'environnement marin de la plupart des glaciers qui drainent les calottes glaciaires (Syvitski et al., 1989). Divers processus sédimentaires dans des environnements des fjords peuvent être liés à des processus de la fonte du glacier tels que les débris délestés par les icebergs, les coulées de débris glaciogéniques et les courants de turbidité (Shaw, 1987 ; Syvitski et al., 1989). Ainsi, la configuration et les caractéristiques sédimentologiques de ces dépôts peuvent être utilisés pour identifier les périodes d'activité glaciaire (Dowdeswell et al., 2015 ; Jenner et al., 2018 ; Lévesque et al., 2020). De même, les caractéristiques géomorphologiques et les taux de sédimentation élevés ont le potentiel de faire des fjords des environnements de dépôt idéaux pour préserver des enregistrements continus des changements climatiques et environnementaux avec une résolution temporelle élevée (Syvitski et al., 1989 ; Howe et al., 2010). Le présent projet de maîtrise vise donc à reconstituer la dynamique de la CGP à partir de l'étude des séquences sédimentaires prélevées le long du fjord Coronation afin de compléter et d'approfondir les connaissances des mécanismes climatiques et océanographiques qui interviennent dans la régulation de la dynamique de cette calotte glaciaire.

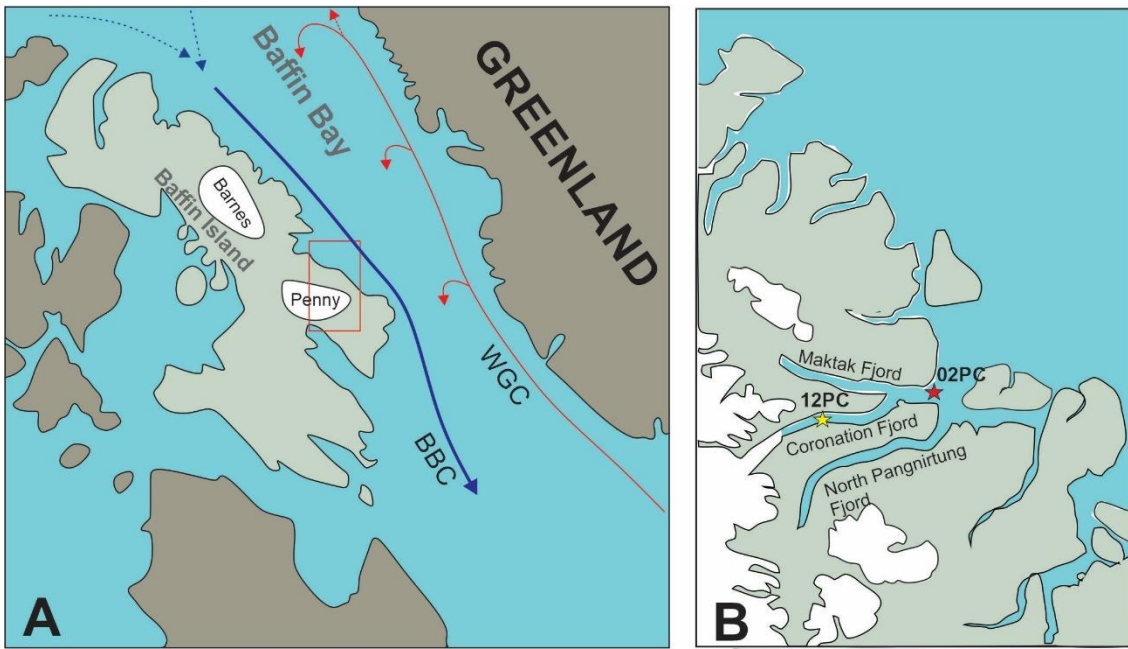


Fig. 1. (A) Localisation de la calotte glaciaire Penny sur l'île de Baffin. Les flèches représentent le courant relativement chaud de l'ouest du Groenland (WGC), et le courant froid de l'île de Baffin (BBC), (B) sites de collecte des carottes 05BC, 02PC/TWC (étoile rouge), et les carottes 12PC/TWC (étoile jaune).

## 2. OBJECTIFS DE RECHERCHE ET APPROCHE METHODOLOGIQUE

L'objectif principal de ce projet est de déterminer et d'interpréter les causes des principales variations sédimentologiques, minéralogiques, géochimiques et magnétiques de deux séquences de sédiments marins prélevées à proximité de la CGP, afin de documenter l'influence des changements climatiques et océanographiques au cours de l'Holocène tardif sur la dynamique du glacier. Pour ce faire, ce projet de recherche s'appuie sur deux objectifs spécifiques : **1)** reconstituer les transferts sédimentaires en provenance de la CGP au cours de l'Holocène tardif en utilisant la distribution granulométrique, la minéralogie et la géochimie élémentaire des sédiments, et **2)** documenter l'influence des changements climatiques et océanographiques holocènes sur la dynamique de la CGP en utilisant les analyses et la datation des sédiments pour placer la variabilité des propriétés

sédimentologiques, minéralogiques, géochimiques et magnétiques dans un cadre chronologique précis.

Les carottes sédimentaires ont été récoltées à bord du brise-glace de la Garde côtière canadienne (NGCC) Amundsen lors de la mission ArcticNet de 2018 (Leg 2b ; Montero-Serrano et al., 2018) et 2019 (Leg 3 ; Normandeau et al., 2019). Un carottier à boîte (AMD1803-05BC ; 43cm) et un carottier à piston plus un carottier de déclenchement (AMD1803-02PC-TWC ; 228 et 64cm) ont été prélevés à la jonction de trois fjords (Nord de Pangnirtung, Coronation et Maktak ; 67.284 ° N ; 63.909 ° W ; 609 m de profondeur). Tandis qu'un carottier à piston (AMD2019-804-12PC-TWC ; 619 et 277 cm) a été échantillonné dans le fjord Coronation (67.21934 ° N ; -64.71831 ° W ; 189 m de profondeur). Les profils sismiques et la bathymétrie multifaisceaux ont été utilisés pour sélectionner les sites d'échantillonnage (Fig. 1). Les carottes à boîte (BC) et à déclenchement (TWC) ont été sous-échantillonnées chaque centimètre et tous les 3 cm dans la carotte à piston (PC). Les carottes ont été analysées au tomodensitomètre utilisant les rayons X (X-ray Computed Tomography; X-CT) et au Multi Sensor Core Logger (MSCL) de GEOTEK pour mesurer des paramètres physiques et chimiques (densité, susceptibilité magnétique, couleur, et composition chimique ; St-Onge et al., 2007). La chronologie des carottes a été déterminée par l'analyse du  $^{210}\text{Pb}$  et  $^{239+240}\text{Pu}$  dans les carottes 05BC et 12TWC (Ketterer et al. 2004 ; Sánchez-Cabeza & Ruiz-Fernández, 2012) et avec des mesures paléomagnétiques ainsi que des âges  $^{14}\text{C}$  pour les carottes 02PC et 12PC (ex. Barletta et al., 2010 ; Deschamps et al., 2018 ; Caron et al., 2018). Les carottes BC, TWC et PC ont été combinées en une séquence composite afin d'obtenir une séquence sédimentaire complète (Fig. S1). Une approche bayésienne a été utilisée pour créer un modèle chronostratigraphique de la séquence composite, en utilisant le logiciel BACON (Blaauw and Christen, 2011). Les analyses granulométriques ont été réalisées à l'aide d'un granulomètre laser Beckman Coulter LS13320 et la distribution granulométrique et les paramètres statistiques ont été calculés avec le logiciel GRADISTAT (Blott & Pye, 2001). La composition minéralogique a été analysée par diffraction des rayons X (XRD ; Eberl, 2003) et le programme macro Excel ROCKJOCK v11 a été utilisé pour la quantification des principales composantes minéralogiques. Finalement, l'ensemble des

données sera archivé dans le système de gestion des données PANGAEA (<https://www.pangaea.de/>).

### **3. PRESENTATION DE LA ZONE D'ETUDE**

L'île de Baffin est la plus grande île de l'AAC avec 507 451 km<sup>2</sup> et contient environ 22 % de la glace des glaciers de l'AAC (calottes glaciaires Penny et Barnes ; Fig.1). Ces glaciers ont perdu un volume de glace à un rythme de 23.8 Gt an<sup>-1</sup>, ce qui a contribué à une élévation du niveau de la mer global de 0,07 mm an<sup>-1</sup> au cours des dernières décennies (Gardner et al., 2012 ; Van Wychen et al., 2015 ; Schaffer et al., 2017). La CGP est composée d'une grande masse de glace centrale de ~6,500 km<sup>2</sup>. La perte de masse sur la CGP a augmenté rapidement au cours des deux dernières décennies, passant de  $-1.3 \pm 0.7$  Gt an<sup>-1</sup> entre 1995 et 2000 à  $-2.9 \pm 1.1$  Gt an<sup>-1</sup> entre 2000 et 2005 à  $-5.4 \pm 1.9$  Gt an<sup>-1</sup> entre 2005 et 2013 (Abdalati et al., 2004 ; Gardner et al., 2012 ; Nöel et al., 2018 ; Schaffer et al., 2020). Cela implique que la CGP a perdu environ 1.7 Gt de glace par °C de réchauffement (Nöel et al., 2018 ; Fig. 2). L'accélération du taux de perte de masse est associée à des anomalies de température de l'air de plus en plus positives durant l'été et l'hiver dans l'Arctique oriental, après 1980, augmentant ainsi la fonte de la glace (Zdanowicz et al., 2012).

La CGP alimente plusieurs glaciers dont deux sont à terminaison marine. L'un d'entre eux est le glacier Coronation, qui a montré une diminution moyenne de la vitesse des glaces de 25 % par décennie pour la période 1985-2010 (Heid and Kääb, 2012b). De plus, ce glacier présente la plus grande contribution de décharge d'icebergs avec un taux de 10.6Mt an<sup>-1</sup> qui représentait 0,2 % de la perte de masse totale (par fonte et vêlage) sur la CGP en 2011 (Van Wychen et al., 2012 ; 2015). Ces hautes vitesses d'écoulement des glaciers suggèrent une forte activité liée au réchauffement climatique, ce qui en fait un lieu stratégique pour reconstituer les changements à long terme des transferts de sédiments à partir de la CGP.

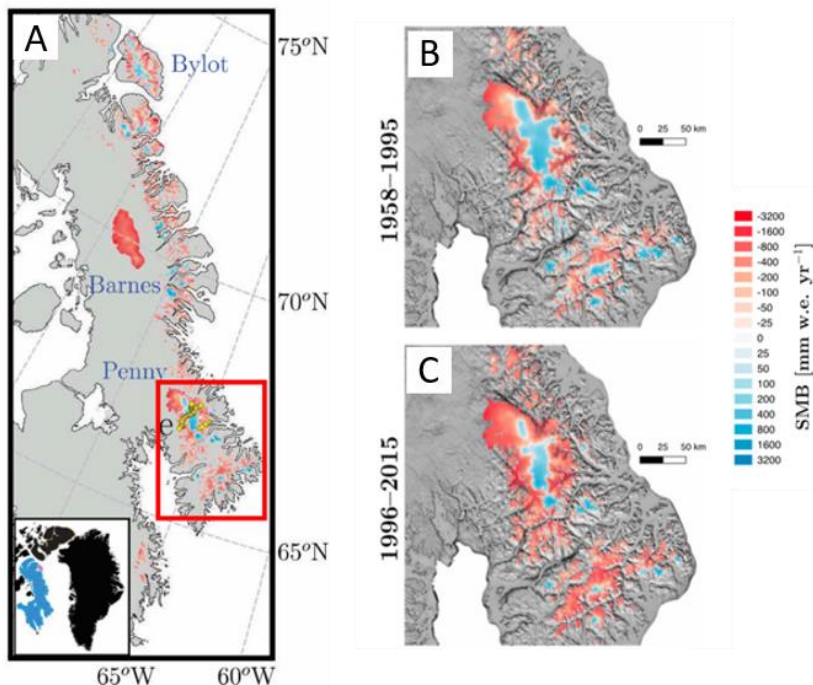


Fig. 2. Cartes du bilan de masse des glaciers et calottes glaciaires de l'Île de Baffin et de la calotte glaciaire Penny (A), moyennées pour les périodes 1958–1995 (B) et 1996–2015 (C). SMB = bilan de masse de la surface (Nöel et al., 2018).

### 3.1 Circulation océanique

La baie de Baffin forme un bassin océanique étroit situé entre l'AAC et le Groenland, qui est caractérisé par une circulation océanique dans le sens inverse des aiguilles d'une montre (Fig. 1). Ce bassin implique le courant de l'île de Baffin (BIC) et le courant de l'ouest du Groenland (WGC). Le courant de l'île de Baffin est originaire des eaux froides ( $> -1^{\circ}\text{C}$ ) et douces de l'Arctique et s'écoule vers le Sud, longeant la partie est de l'île de Baffin (Münchow et al., 2015 ; Zweng and Münchow, 2006 ; Tang et al., 2004). Le courant de l'ouest du Groenland est un mélange d'eaux froides et de faible salinité provenant de l'Est du Groenland en tant que des eaux chaudes et salées provenant du courant Irminger. En conséquence, le courant de l'ouest du Groenland est relativement plus chaud et salé comparativement au courant de l'île de Baffin, ( $> 2^{\circ}\text{C}$  ; Zweng and Münchow, 2006). Donc, l'advection d'eaux subarctiques relativement chaudes dans la baie de Baffin par le courant de

l'ouest du Groenland transporte la chaleur vers la baie de Baffin et régule fortement le climat de la région (Tang et al., 2004 ; Holland et al., 2008 ; Münchow et al., 2015).

Les fjords à l'est de l'île de Baffin sont des bassins semi-fermés. Par conséquent, la circulation dans les fjords et les échanges d'eau avec la baie de Baffin peuvent être limités aux courants de marée, l'activité des vagues, la force de Coriolis et le drainage latéral influencent également la circulation et les processus sédimentaires dans ces bassins (Gilbert, 1982a ; Gilbert et al., 1989).

### **3.2 Géologie et sédimentation**

Au début de l'ère tertiaire, le Groenland s'est séparé de l'Amérique du Nord et, par la suite, le bord oriental de l'île de Baffin a été soulevé, atteignant des hauteurs de 2000 mètres (Miller, 1973). Ensuite, l'érosion fluviale et glaciaire a disséqué le terrain montagneux, générant les fjords qui représentent l'environnement de transition entre le plateau intérieur et l'océan. Les fjords Maktak, Coronation et North Pangnirtung ont été creusés dans le substratum rocheux de Cumberland, constitué principalement de gneiss précambrien, de granite-tonalite et de monzonite quartzique (Clarke et Upton, 1971 ; Jackson et Berman, 2000 ; St-Onge et al, 2009 ; Fig. 3).

La sédimentation quaternaire dans les bassins des fjords a été contrôlé par le transport des sédiments en suspension, par les plumes d'eau de fonte dans les fjords provenant des glaciers, par des débris délestés par des icebergs (IRD), les écoulements gravitaires tels que les courants de turbidité, les écoulements de débris et les écoulements fluidisés, et par le transport éolien (Gilbert, 1982).

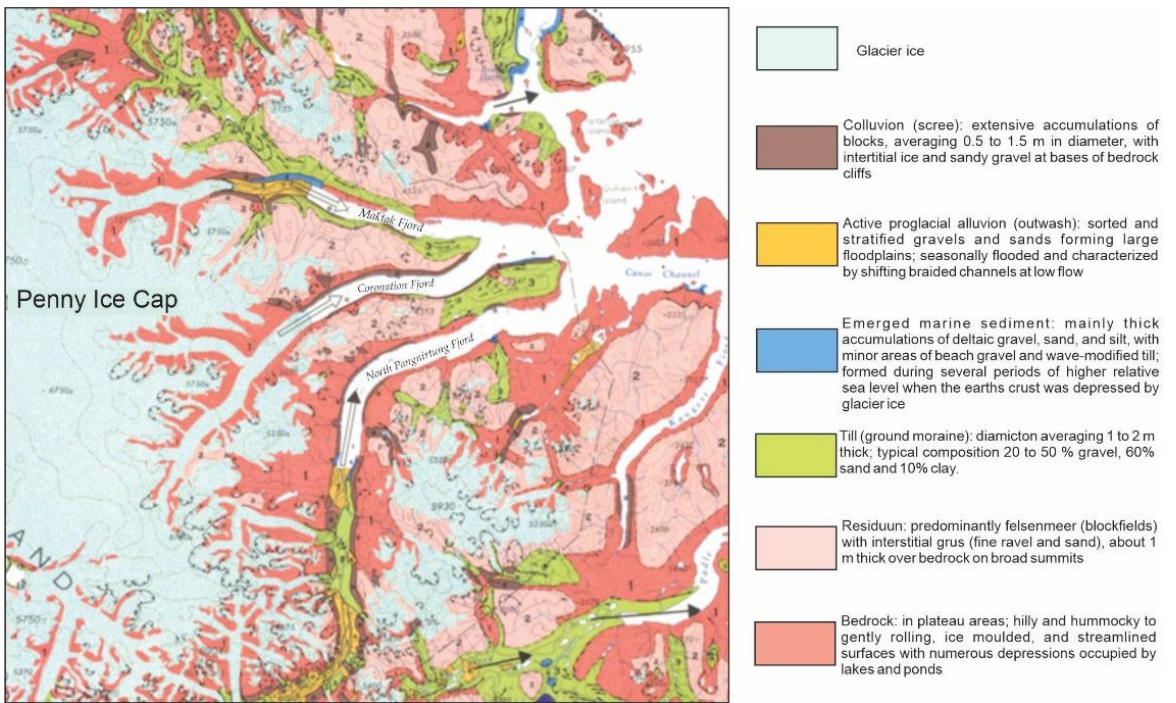


Fig. 3. Carte de géologie superficielle de la péninsule Cumberland sur l'île de Baffin (adapté de Dyke et al., 1982).

## CHAPITRE 1

### SEDIMENTARY RECORDS ASSOCIATED WITH THE DYNAMICS OF THE PENNY ICE CAP (BAFFIN ISLAND, NUNAVUT, CANADA) DURING THE LATE HOLOCENE

María-Emilia Rodríguez-Cuicas<sup>1</sup>, Jean-Carlos Montero-Serrano<sup>1</sup>, Guillaume St-Onge<sup>1,2</sup>, Alexandre Normandeau<sup>3</sup>

<sup>1</sup>Institut des sciences de la mer de Rimouski (ISMER), Université du Québec à Rimouski (UQAR), Québec-Océan, Geotop, Rimouski, Québec, Canada.

<sup>2</sup>Canada Research chair in Marine Geology, Rimouski, Quebec, Canada.

<sup>3</sup>Geological Survey of Canada (Atlantic), Bedford Institute of Oceanography, Dartmouth, Nova Scotia, Canada.

#### 1. Introduction

The Canadian Arctic Archipelago (CAA) has suffered one of the largest glacier volume losses in the past decade, making this region one of the largest contributors to global sea level rise (Radić and Hock., 2010; Gardner et al., 2011; Harig and Simons, 2016; Noël et al., 2018; Ciraci et al., 2020). Lenaerts et al. (2013) estimated that the CAA glacier mass loss by the end of the 21st century will contribute  $\sim 0.35 \pm 0.24 \text{ mm yr}^{-1}$  to global sea level rise. Approximately 22% of glacier ice in the CAA is contained on Baffin Island (Penny and Barnes Ice Caps) and is considered the last vestiges of the Laurentide Ice Sheet (Zdanowicz et al. 2012; Fig. 4). Glaciers and ice caps on Baffin Island have lost approximately 23.8 Gt  $\text{yr}^{-1}$  of ice, which has contributed to a rise of  $0.07 \text{ mm yr}^{-1}$  in the global sea level during recent decades (Gardner et al. 2012; Van Wychen et al., 2015; Schaffer et al., 2017).

Penny Ice Cap (PIC) on the Cumberland Peninsula has a total area of  $6,410 \text{ km}^2$  and is the most southerly part of the CAA, which makes it highly sensitive to climate change (Zdanowicz et al., 2012). Instrumental data have shown that the velocity of the tidal glaciers of the PIC decelerated from  $53$  to  $32 \text{ m yr}^{-1}$  between 1985 and 2011 (Van Wychen et al.,

2015; Schaffer et al., 2017), and the greatest iceberg discharge contribution occurred from Coronation Glacier (Coronation Fjord) at rates of 8-12 Mt yr<sup>-1</sup> (Van Wychen et al., 2015). However, studies of glacier dynamics in the CAA are still debating whether the observed variations are unprecedented during the long-term Holocene evolution (Oerlemans, 2005; Schaffer et al., 2017).

Although records of Holocene paleoclimatic conditions on Baffin Island exist (ice cores: Fisher, 1998; Zdanowicz et al., 2012; remote sensing: Van Wychen et al., 2015; Schaffer et al., 2017; lacustrine sediments: Briner et al., 2006; Thomas and Briner, 2009; Briner et al., 2009; Thomas 2011; Narancic et al., 2021), reconstructions of past environmental changes in sediment records of fjords are less abundant. Only a few sedimentological studies have been carried out in the fjords from south Baffin Island (e.g., Syvitski and Schafer, 1985; Syvitski, 1989). Fjords represent transitions from the terrestrial to the marine environment for most glaciers that drain ice caps. Similarly, geomorphological features and high sedimentation rates have the potential to make fjords ideal depositional environments to preserve records of climate and environmental changes with high temporal resolution (Syvitski et al., 1989; Howe et al., 2010). In addition, the sedimentary dynamics of glaciers and ice sheets can generate considerable temporal and spatial variability in glaciogenic depositional processes (e.g., Dowdeswell et al., 2015). Indeed, a variety of sedimentary processes in glacial environments can be linked to glacier melt processes, such as iceberg-delivered debris, glaciogenic debris flows, and turbidity currents (Shaw, 1987; Syvitski et al., 1989). Thus, the configuration and sedimentological characteristics of these deposits can be used to identify periods of glacial activity (Dowdeswell et al., 2015; Jenner et al., 2018; Lévesque et al., 2020).

In this context, studying the long-term sedimentary records along Coronation Fjord will help us to better understand the dynamics of the PIC beyond the instrumental record. Therefore, this study focuses on two composite sediment cores (AMD1803-02CS and AMD2019-804-12CS) collected along Coronation Fjord in southeastern Baffin Bay (Fig. 5). These sedimentary sequences represent a good location to record glacial sediment discharges from

the northeastern sector of the PIC.  $^{210}\text{Pb}$ ,  $^{239+240}\text{Pu}$ , paleomagnetic and radiocarbon analyses, together with physical, sedimentological, mineralogical and elemental geochemical properties are combined in these composite sediment cores to 1) reconstruct changes in sediment transfers from the PIC related to the late Holocene climate variability and 2) assess the significance of recent glaciological changes in the northeastern PIC. The results of this study will help place the recent ice mass loss in the PIC in context of longer-term variability.

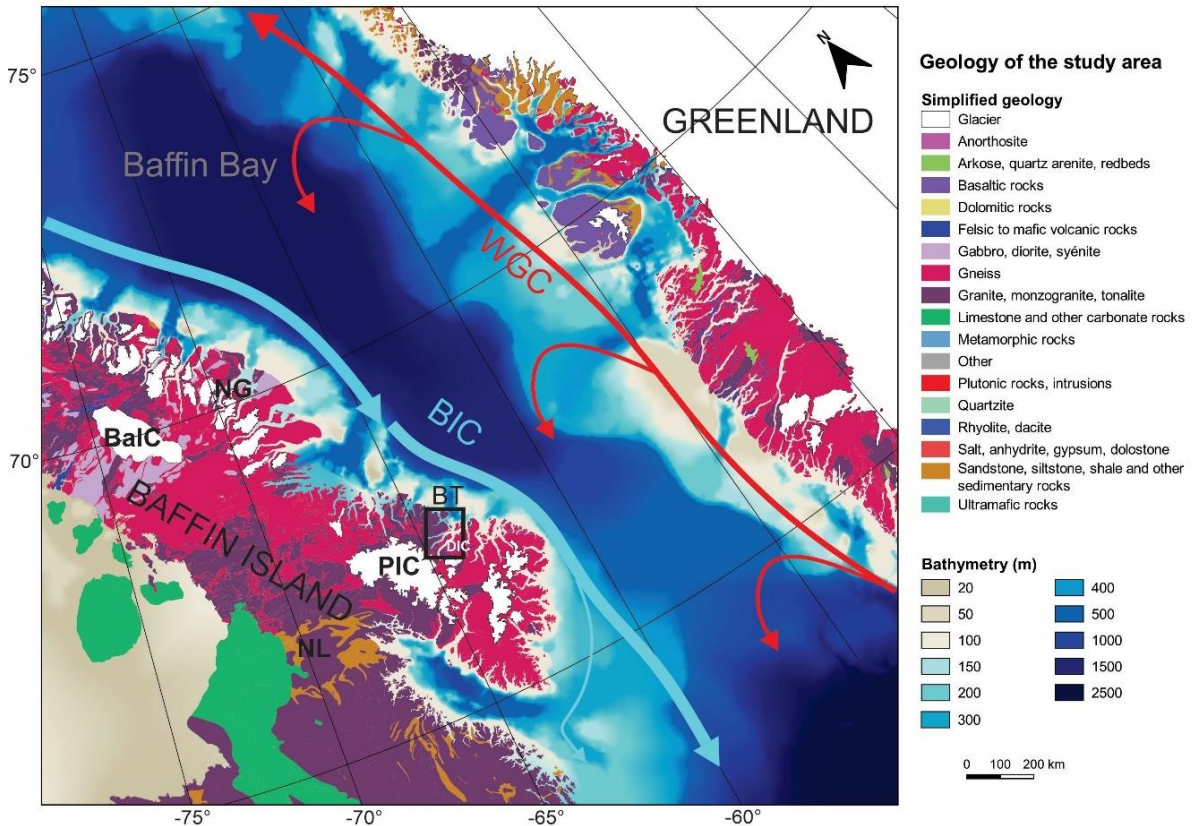


Fig. 4. Regional geology and location of the Penny Ice Cap (PIC) on Baffin Island. The arrows represent the relatively warm West Greenland Current (WGC) and the cold Baffin Island Current (BIC). Abbreviations are as follows: Broughton Trough (BT), Barnes Ice Cap (BaIC), Divide Ice Cap (DIC), Naqsaq Glacier (NG), and Nettilling Lake (NL).

## **Regional setting**

### 2.1. Geology, physiography and fjord circulation

Maktak, Coronation and North Pangnirtung Fjords are situated in the Cumberland Peninsula and were carved into bedrock during early Pleistocene or even the Pliocene glaciations (Gilbert, 1982a; Syvitski and Piper, 1990). The bedrock on the eastern Cumberland Peninsula consists of Precambrian gneiss, granite-tonalite, and quartz monzonite, while carbonate rocks are absent (Fig. 4; Clarke & Upton, 1971; Jackson and Berman 2000; St-Onge et al. 2009). The fjords were carved to a maximum water depth of 320 m in Maktak Fjord, 606 m in Coronation Fjord, and 479 m in North Pangnirtung Fjord (Fig. 5; Gilbert, 1985). They have served as channels for glacial ice originating from the PIC, which discharges through the Broughton Trough into Baffin Bay (Fig. 4; Gilbert, 1982a; Schatz et al., 2013).

Locally, circulation in the fjords and exchange of water with Baffin Bay may be restricted (Gilbert et al., 1989). These fjords are dominated by freshwater input at their heads. However, tidal currents, wave activity, the Coriolis force and side entry drainage also influence the circulation and sedimentary processes in these basins (Gilbert, 1982b; Syvitski, 1989; Schatz et al., 2013). Tidal activity allows seawater to penetrate into the fjord for little more than 100 meters (Gilbert, 1982a). The Coriolis force is very influential in controlling the deposition of suspended particles, causing a noticeably higher accumulation of sediment along the southern side of the fjords compared to the north side (Gilbert, 1982a; Gilbert, 1983; Syvitski, 1989; Syvitski and Shaw, 1995).

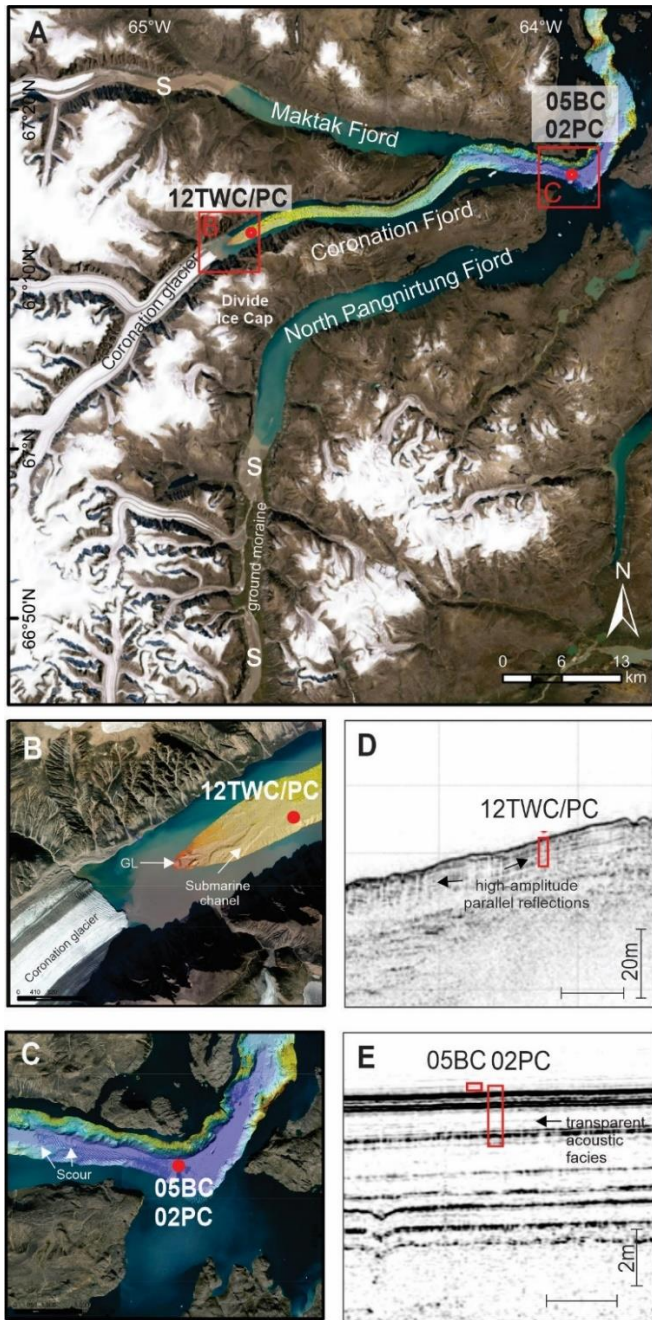


Fig. 5. (A-C) MODIS satellite image from 11 May 2020 showing a snapshot of Maktak, Coronation, and North Pangnirtung Fjords (source: NASA Worldview), as well as the bathymetry and the location of the cores in this study. The bathymetric data are from Normandeau et al., (2019). (D-E) Sub-bottom profiles across coring stations. S= sandur surface; GL= grounding line.

At the regional level, the climate of the east coast of Baffin Island has been strongly modulated by patterns of ocean circulation in Baffin Bay during the Holocene (Munchow et al., 2015). This basin contains the Baffin Island Current (BIC), which flows southward in the western part of Baffin Bay and originates from cold Arctic waters, and the West Greenland Current (WGC), which flows northward along the western coast of Greenland before mixing with the BIC in Smith Sound (Fig. 4; Tang et al., 2004). The WGC is fed by Irminger Current (IC) water, becoming the northern limb of the North Atlantic subpolar gyre (Tang et al. 2004). Thus, changes in the balance between the relatively warm salty WGC and the outflow of cold low-salinity surface water from the BIC directly impact both temperature and the amount of precipitation in Cumberland Peninsula.

## 2.2. Sedimentation

Maktak, North Pangnirtung and Coronation Fjords have been filled with glaciomarine sediments (58 m, 36 m and 94 m thick, respectively; Gilbert, 1985). Contemporary sedimentary processes in these basins are characterized by 1) ice-rafted debris (IRD); 2) suspension fall-out of fine-grained sediment from meltwater plumes; 3) deposition of graded sand beds from gravity flows, such as turbidity currents and hyperpycnal flows, and 4) aeolian transport from sandy surfaces, mainly from Maktak and North Pangnirtung Fjords (Gilbert, 1982b). IRD deposition is common in the sedimentary record within Coronation Fjord due to the presence of outlet tidewater glaciers and calving icebergs (Gilbert, 1982b; Syvitski, 1989). Meltwater plumes are the main transport agents and suppliers of fine-grained sediments (Gilbert, 1982b; Syvitski, 1989). During periods of high meltwater discharge, gravity flows lead to sediment accumulation in zones proximal to Coronation Glacier (Gilbert, 1982b; Syvitski, 1989). A similar process may also occur over the delta slopes at the heads of Maktak and North Pangnirtung Fjords (Gilbert, 1983). Turbidity current deposits have been identified as several distinct intervals of 1–5 cm thick normally graded layers in Maktak Fjord (Schatz et al., 2013). Finally, aeolian sediments are deposited relatively close to glacier margins and are typically represented by well-sorted medium-grained sand (Gilbert, 1983; McKenna-Neuman and Gilbert, 1986). Superficial seabed sediments are

predominantly composed of marine grayish-brown silts and clays with high alkali feldspar (>20%), plagioclase (>20%), clay mineral (<20%), amorphous silica (~15%), and quartz (~10%) contents (Andrews et al 2018; Andrews, 2019).

### 3. Materials and methods

#### 3.1. Sediment cores

Sediment cores were recovered onboard the Canadian Coast Guard Ship (CCGS) icebreaker *Amundsen* along Coronation Fjord during the 2018 and 2019 ArcticNet expeditions (Table 1; Fig. 5). Cores AMD1803-05BC (box core) and AMD1803-02PC (piston core), hereafter referred to as 05BC and 02PC, were recovered at the junction of three fjords (north of Pangnirtung, Coronation and Maktak). Cores AMD2019-804-12PC/TWC (piston core and companion trigger weight core), hereafter referred to as 12PC/TWC, were collected at the head of Coronation Fjord. Both coring sites were identified using high-resolution seismic profiles and multibeam-bathymetry data (Montero-Serrano et al. 2018; Normandeau et al., 2019). Subbottom profiles were acquired using a Knudsen 3260 CHIRP sonar at a frequency of 3.5 kHz. The multibeam-bathymetry data were obtained from a Kongsberg EM302 multibeam echosounder (30 kHz) operated with the Seafloor Information System (SIS). All the acquired data were postprocessed using CARIS HIPS&SIPS 11.1 software. Cores 05BC and 12TWC (first 50 cm) were evenly sampled at 1 cm intervals, whereas cores 02PC and 12PC were sampled at 3-4 cm intervals. Cores 02PC and 12PC/TWC, were subsampled with u-channels (1.5-m-long u-shaped plastic liners with a 2x2 cm cross-section) for paleomagnetic analyses.

Table 1. Location of the sampling sites, water depth, and length of the cores used in this study.

Core	Latitude (°N)	Longitude (°W)	Zone	Water depth (m)	Core length (cm)
AMD1803-05BC	67.28412	-63.91034	Ice-distal	609	43
AMD1803-02PC	67.28464	-63.90958	Ice-distal	609	222
AMD2019-804-12PC/TWC	67.21934	-64.71831	Ice-proximal	189	619/277

### 3.2. Laboratory analyses

#### 3.2.1. Multi-sensor core logger analyses (physical and chemical properties)

All whole cores were X-radiographed using a GEOTEK X-ray Computed Tomography (X-CT) system. The digital X-ray images obtained by X-CT are useful to visualize different facies and sedimentary structures (St-Onge et al. 2007). Next, and prior to core splitting, wet bulk densities (determined from gamma ray attenuation) were measured at 1 cm intervals using a GEOTEK Multi-Sensor Core Logger (MSCL). Subsequently, the cores were split, described and digitally photographed. The low-field volumetric magnetic susceptibilities ( $k_{LF}$ ), diffuse spectral reflectance and chemical composition via portable X-ray fluorescence (pXRF) were then measured using a GEOTEK MSCL system at 0.5 cm intervals for core 05BC and 1 cm intervals for cores 02PC/TWC and 12PC/TWC. The reflectance was obtained by using a hand-held Minolta CM-2600d spectrophotometer coupled to the MSCL, and the sediment color is expressed according to the L\*, a\* and b\* color space of the International Commission of Light (e.g., St-Onge et al. 2007). Only the L\* and a\* indexes are used in this study. L\* is a black-to-white scale (0–100), and a\* is a green–red scale (-60 to +60) (St-Onge et al. 2007; Debret et al. 2011). The pXRF scans were made using an energy-dispersive Olympus Innov-X DELTA portable X-ray fluorescence analyzer integrated with the MSCL and equipped with a 40 kV rhodium anode X-ray tube. pXRF analysis was conducted using GeoChem with two beams (40 and 10 kV) with a 60-second exposure time per beam.

#### 3.2.2. Grain-size

Sediment grain size analyses (<2 mm fraction) were performed using a Beckman Coulter LS13320 laser diffraction grain size analyzer, with a detection range of 0.04–2000  $\mu\text{m}$  (at a 1 cm resolution in core 05BC and 3 cm resolution in cores 02PC and 12PC/TWC). The sediment samples were pretreated with 10 mL hydrogen peroxide ( $\text{H}_2\text{O}_2$ ; 30% v/v) to remove organic matter. Samples were deflocculated by successive washing with distilled water and subsequently disaggregated using an in-house rotator for 12 h prior to particle size measurements. The grain size distribution and statistical parameters were calculated using GRADISTAT software version 9.1 (Blott and Pye 2001). The grain size distributions can

help to characterize lithologic changes and document changes in sediment transport regimes over time (e.g., Casse et al. 2017; Gamboa et al. 2017; Deschamps et al. 2018). Furthermore, the gravel-sized clast abundance was determined using the method described by Grobe (1987), which consists of counting the >2 mm fraction on the X-CT scan images of the core in contiguous 2-cm windows. The abundance of gravel-sized clasts is used here to identify intervals in the cores influenced by abundant ice rafting (e.g., IRD and sea ice transport; Andrews 2000). In addition, the sortable silt mean size ( $\overline{SS}$ ) flow speed proxy, which corresponds to the mean grain size of the non-cohesive silt fraction (10–63  $\mu\text{m}$ ) and the percentage of sortable silt (SS%) in the <63  $\mu\text{m}$  fraction (McCave et al. 1995) was calculated for both cores using the approach developed by McCave and Andrews (2019a).

### 3.2.3. Quantitative bulk mineralogy

Quantitative X-ray diffraction mineralogy (qXRD) of the <2 mm sediment fraction was studied according to the method developed by Eberl (2003). For this, ~1 g of each sample was spiked with 0.25 g of corundum and then ground in a McCrone micronizing mill using 5 ml of ethanol to obtain a homogenous powder. Next, 0.5 ml of Vertrel was added to the mixture to prevent the possible agglomeration of finer particles. The powder sample was then sieved (<300  $\mu\text{m}$ ), back-loaded into the holders, and analyzed on a PANalytical X'Pert powder diffractometer. Samples were scanned from 5° to 65° two-theta in steps of 0.02° two-theta, with a counting time of 2 seconds per step. For the quantification of the major mineralogical components, sediment X-ray diffraction (XRD) scans were converted into mineral weight percent (wt.%) using the Excel macro program ROCKJOCK v11 (Eberl, 2003). This program uses a full-pattern fitting method that permits the quantification of whole-sediment mineralogy with a precision of  $\pm 3$  wt.% (Eberl, 2003). The calculated total mineral wt.% was normalized to a sum of 100%. The principal minerals that were analyzed by this method were quartz (Qz), K-feldspar (Kfs), plagioclase (Pl), dolomite (Dol), amphibolite (Am), pyroxene (Px), Fe-bearing (Fe-b) minerals, smectite (Sme), illite (Ill, including muscovite), chlorite (Chl), and biotite (Bt).

### 3.3. Chronology

#### 3.3.1. $^{210}\text{Pb}$ and $^{239+240}\text{Pu}$ analyses

The chronology of core 05BC was assessed by lead ( $^{210}\text{Pb}$ ) and plutonium ( $^{239+240}\text{Pu}$ ) measurements. Sediment samples from the top 25 cm of core 05BC (at 1 cm intervals) were freeze-dried, homogenized, and sealed in petri dishes for >21 days to allow secular equilibrium. Next, the measurements of radioisotope  $^{210}\text{Pb}$  were performed at the Institut des sciences de la mer de Rimouski (ISMER) by gamma spectrometry following Reyss et al. (1995). The counting error was evaluated at  $1\sigma \sim 5\%$ . The  $^{210}\text{Pb}$  excess activities were calculated by subtracting the  $^{226}\text{Ra}$ -supported activity from the total  $^{210}\text{Pb}$  activity. A constant rate supply  $^{210}\text{Pb}$  model was used to determine sedimentation rates and to estimate ages (Appleby and Oldfield, 1983). In addition, freeze-dried sediment samples (2 g) from the top 25 cm of core 05BC (at 1 cm intervals) were analyzed at Northern Arizona University for  $^{239+240}\text{Pu}$  concentrations using a Thermo X2 quadrupole inductively coupled plasma–mass spectrometry system and following the method described in Ketterer et al. (2004). The age model from core 05BC (Fig. S1), including  $^{210}\text{Pb}$ ,  $^{239+240}\text{Pu}$  and accelerator mass spectrometry (AMS)  $^{14}\text{C}$  data, was developed with the ‘serac’ R package (Bruel and Sabatier, 2020). The results of the  $^{210}\text{Pb}$  dating will also be used to build the age model of the composite sequence that includes the 05BC and 02PC cores.  $^{210}\text{Pb}$  measurements from the top 123 cm of core 12TWC were performed at the Geotop Research Center (Montréal, Canada) by alpha spectrometry (Fig. S2). Before the analysis, all samples were sieved through a 150- $\mu\text{m}$  Nitex® mesh to prevent biases in  $^{210}\text{Pb}$  data linked to bulk grain size variations; the samples were then oven-dried (70°C), crushed and homogenized with an agate mortar.

#### 3.3.2. Palaeomagnetic analysis

Paleomagnetic data were acquired at 1-cm intervals on u-channel samples using a 2G Enterprises™ u-channel cryogenic magnetometer model 755 SRM and a pulse magnetizer for the induction of isothermal remanent magnetizations (IRMs). Due to the finite spatial resolution of the magnetometer’s pickup coils, each measurement integrates a stratigraphic interval of 7-8 cm (Philippe et al., 2018) and to eliminate edge effects the data points from

the upper and lower 4 cm of each u-channel were not used (Weeks et al., 1993). The natural remanent magnetization (NRM) was measured and then stepwise demagnetized by alternating field (AF) demagnetization at peak fields of 0 to 85 mT at 5-mT increments. Later, a continuous field of 50 µT (direct current or DC bias field) and a 100 mT alternating field were applied to the sample to impart anhysteretic remanent magnetization (ARM). Subsequently, DC pulse fields of 300 mT (IRM) and 950 mT (saturated isothermal remanent magnetization; SIRM) were applied, and the IRM progressively demagnetized following the same procedure used for ARM. SIRM was demagnetized at peak fields of 0, 10, 30 and 50 mT.

The magnetic inclination of the characteristic remanent magnetization (ChRM) was calculated using a least squares line fitting procedure (Kirschvink, 1980) with the Excel macro developed by Mazaud (2005). This computation also provided the maximum angular deviation (MAD) values and the median destructive field (MDF). The MAD values provide a quantitative measurement of the analytical uncertainty and an estimation of the quality of the paleomagnetic data. MAD values lower than 5° are indicative of high-quality directional data (Stoner & St-Onge 2007). These analyses allow us to identify possible rapidly deposited layers such as turbidites and debrites, which are characterized by low-quality paleomagnetic data and shallow inclinations (e.g., St-Onge et al. 2004; Tanty et al. 2016; Philippe, 2019). Finally, the median destructive field (MDF) of the NRM was also calculated. The MDF represents the required demagnetization field necessary to reduce the initial magnetic remanence by half of its initial intensity. The MDF is an indicator of magnetic mineralogy, reflects the mean coercivity state of the magnetic grain assemblage and depends on both the grain size and the mineralogy (e.g., Stoner & St-Onge 2007).

### 3.3.3. Radiocarbon analysis

To support the chronostratigraphical framework derived from the paleomagnetic data, we used eight AMS radiocarbon ( $^{14}\text{C}$ ) ages (Table 2). Six samples (five in core 12PC and one in core 05BC) of well-preserved marine shell fragments (mainly *Portlandia arctica*) were measured, while one sample of mixed benthic foraminiferal species from core 02PC was

measured (Table 2). AMS  $^{14}\text{C}$  measurements were performed at the Keck Carbon Cycle AMS laboratory at the University of California - Irvine (California, USA) and the Alfred Wegener Institute Helmholtz Centre for Polar and Marine Research (Bremerhaven, Germany). Note that very few foraminifera (<0.02 mg) were recovered from core 02PC, which was not enough to perform AMS analysis. In the Arctic, this recoverable amount is related to the poor preservation of foraminifera and mollusks due to calcium carbonate dissolution in bottom waters (Aksu 1983; de Vernal et al. 1992; Azetsu-Scott et al. 2010). The local marine reservoir age correction ( $\Delta\text{R}$ ) from AMS  $^{14}\text{C}$  ages was calculated from paired  $^{14}\text{C}$  and paleomagnetic dates using the online program *deltar* (Reimer and Reimer, 2017; <http://calib.org/deltar/>) based on the new Marine20 calibration curve (Heaton et al. 2020). Next, the conventional  $^{14}\text{C}$  ages obtained in this study were calibrated using the Marine20 curve by assuming a regional reservoir age correction of  $\Delta\text{R} = -154 \pm 56$  years for core 12PC and  $\Delta\text{R} = 15 \pm 169$  years for core 02PC (Fig. S3). The difference between the two  $\Delta\text{R}$  estimates and the large  $2\sigma$  uncertainties illustrate the inherent variability in the local marine  $\Delta\text{R}$  of glacier-influenced fjords (e.g., Russell et al., 2011).

Table 2. Accelerator mass spectrometry (AMS) radiocarbon dates and calibrations for cores 12PC, 05BC and 02PC, with different reservoir ages.

Laboratory number	Core	Material dated	Depth (cm)	$^{14}\text{C}$ age (a BP)	Error	$\Delta\text{R}=-162\pm68$			$\Delta\text{R}=15\pm169$		
						Median (CE)	Range	$2\sigma$	Median (CE)	Range	$2\sigma$
UCIAMS-233572	12PC	Shell fragment	151	440	30	1835	1730-1950				
UCIAMS-233573	12PC	Shell fragment	168	525	15	1809	1669-1950				
UCIAMS-233566	12PC	Shell fragment	238	685	15	1645	1476-1830				
UCIAMS-233568	12PC	Shell fragment	404	750	15	1586	1438-1759				
UCIAMS-233570	12PC	Shell fragment	482	900	15	1458	1317-1622				
AWI-5664.1.1	05BC	Shell fragment	14.5	103.8	0.9	pMC*			modern (>1962 CE)*		
AWI-6309.1.1	02PC	Mixed-benthic foraminifera	39	1046	63				1489	1159-1871	

\* Date constrained by  $^{239+240}\text{Pu}$  dates (1952 and 1963 CE corresponding with the dates of atmospheric nuclear testing; Ketterer et al., 2002, 2004).

### 3.3.4. Age modelling

Prior to the construction of age-depth models, the correlation of the  $k_{LF}$  and  $\log(\text{Zr/Zn})$  profiles of cores 12TWC/PC, 05BC and 02PC was conducted to estimate the absence and deformation of sediments at the tops of the piston cores (Fig. S4). These correlations suggest that i) approximately 3 cm of sediments at the top of core 02PC were lost during piston coring; ii) no sediments were lost due to coring at the top of core 12PC; and iii) the uppermost parts of cores 12PC and 02PC show deformations at approximately 50 cm and 42 cm, respectively, which is related to the cumulative action of compaction and stretching during piston coring (Fig. S1). Thus, the depths of the piston cores were adjusted accordingly. In this context, since the box and trigger weight corers are designed to recover a relatively undisturbed sample of the sediment–water interface, cores 12PC/TWC and 05BC and 02PC were combined into two composite sequences (hereafter referred to as 12CS and 02CS) based on the correlation of the  $k_{LF}$  and  $\log(\text{Zr/Zn})$  profiles (Fig. S4). Indeed, the upper 50 cm of core 12CS corresponds to core 12TWC, and the rest of the sequence corresponds to core 12PC (50 to 609 cm). In contrast, in core 02CS, the upper 42 cm corresponds to core 05BC, and the rest corresponds to core 02PC (42 to 228 cm). The depths of these composite sequences were adjusted, and the age-depth models were generated using the corrected composite depths. To derive the best age-depth model, we used the R package ‘rbacon’ version 2.5.7 (Blaauw and Christen 2011), as this program allows i) the incorporation of other chronostratigraphic markers (such as  $^{210}\text{Pb}$  and  $^{239+240}\text{Pu}$  dating obtained from ‘serac’ R package and paleomagnetic tie points) and ii) the estimation of the best fit or weighted mean age for each depth with a 95% confidence interval using a Bayesian approach. Although ‘rbacon’ produces a robust age model for cores 12CS and 02CS, we recognize the difficulties associated with establishing accurate age-depth models in marine sediment cores (e.g., Telford et al., 2004; Trachsel and Telford, 2017; Lacourse & Gajewski, 2020).

### 3.4. Statistical approach

The qXRD and pXRF data were analyzed using a compositional data approach, which allows evaluation of data subjected to a constant-unit sum (Aitchison, 1982). For statistical analysis, we followed the approach presented in Montero-Serrano et al. (2010), Schmidt et al. (2019) and Corminboeuf et al. (2021a-b). R software (R Core Team, 2021) was used to perform all statistical analyses. First, values below the detection limit were imputed via multiplicative lognormal replacement with the ‘zCompositions’ package (Palarea-Albaladejo and Martin-Fernandez, 2015) to preserve the geometry of the compositional data while accounting for corresponding detection limit thresholds. Second, a log-centered (clr) transform was applied to the data with the ‘compositions’ package (van den Boogaart and Tolosana-Delgado, 2008) to allow the valid application of classical (Euclidean) statistical methods to the compositional data (Aitchison, 1982, 1990; Montero-Serrano et al., 2010). Next, principal component analysis (PCA) was performed on qXRD and pXRF data to identify mineral and chemical associations with similar relative variations (e.g., von Eynatten et al. 2003; Montero-Serrano et al. 2010). PCA was conducted with the ‘compositions’ (van den Boogaart and Tolosana-Delgado, 2008) and ‘factoextra’ packages (Kassambara and Mundt, 2020).

## 4. Results and interpretation

### 4.1. General grain size, mineralogical and geochemical characteristics

The grain size distributions of cores 12CS and 02CS indicate a composition that is generally dominated by silts and clays, with some intervals composed of medium to coarse sand (Fig. 6). The grain size frequency distributions of these coarse-grained samples show a unimodal shift toward higher values, indicating better sorted sediments and different depositional regimes (Fig. 6A,B). The vertical profiles of D90 show that these coarse-grained intervals are characterized by values of up to 67 µm and 120 µm in cores 12CS and 02CS, respectively (Fig. 11). IRD are abundant in core 12CS, with the highest concentrations in the interval between 250 and 500 cm, while core 02CS shows very low IRD counts.

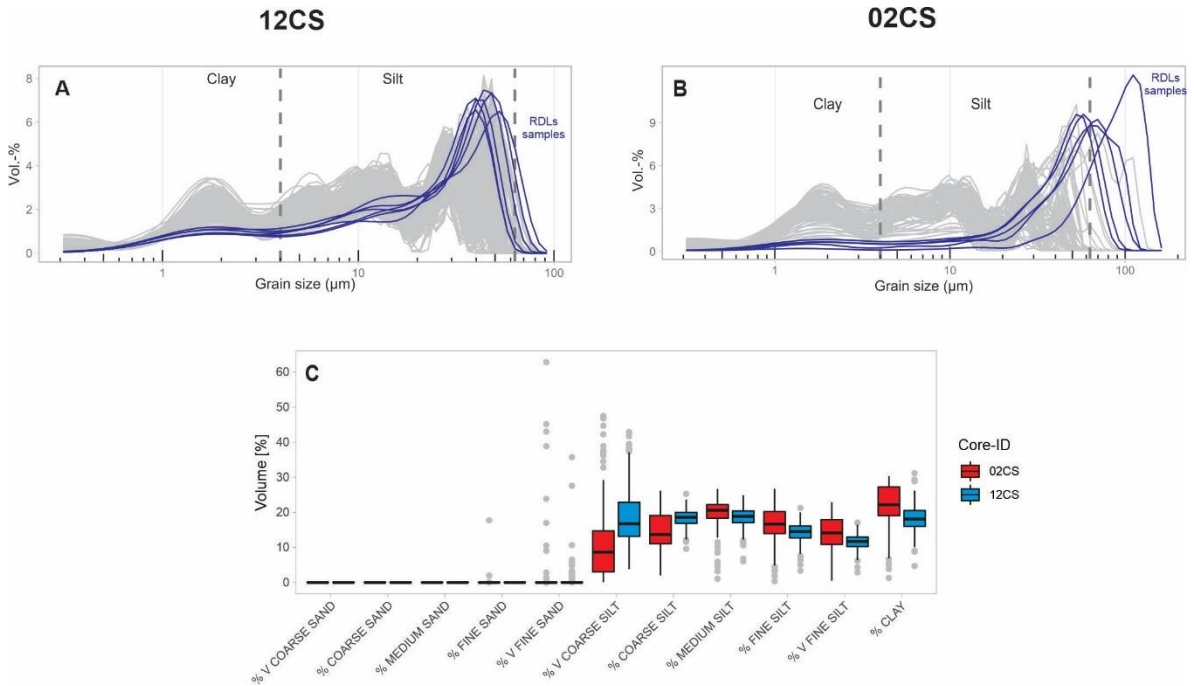


Fig. 6. (A) Frequency curves of raw grain size data for cores 12CS and (B) 02CS; (C) boxplot of the grain size distribution (%) for both cores.

We tested the correlation between  $\overline{\text{SS}}$  and SS% to evaluate whether the sortable silt record in cores 12CS and 02CS was sufficiently current sorted to provide a reliable bottom flow history (McCave and Andrews, 2019a,b). A good positive coefficient of correlation was obtained for both composite sequences ( $r = 0.86$ ,  $n = 240$  for 12CS and  $r=0.94$ ,  $n=89$  for 02CS) (Fig. S6A,C). Likewise, 90% of the data have a five-point running downcore correlation ( $r_{\text{run}}$ ) between  $\overline{\text{SS}}$  and SS% of  $>0.5$  (Fig. S6B,D). These results suggest that much of the sortable silt records in cores 12CS and 02CS are current sorted, mainly driven by changes in the hyperpycnal flow speed.

The boxplot of bulk mineralogical and geochemical data from cores 12CS and 02CS are shown in Figs. 7A,B. The mineralogy of the bulk sediment fraction from Coronation Fjord is dominated by Pl (25–32%), Kfs (24–33%), Qz (13–35%), Chl (1.5–14%), Bt (0.5–10%) and by lower proportions (<5%) of detrital carbonates, Fe-bearing minerals, Am and Px (Fig.

7A). In general, Pl, Kfs, Qz, Chl and Bt represent more than 90% of the overall mineral concentration in both sediment cores. These mineralogical results are consistent with those reported for surface sediments from Coronation, Maktak and Pangnirtung Fjords (Andrews et al., 2018; Andrews, 2019). Furthermore, the major element compositions of bulk sediments in cores 12CS and 02CS are dominated by Si (~0.3–9%), Fe (~0.5–2.5%), K (~0.1–1.5%), Al (~0.3–2%), Ca (~0.2–1.5%) and Ti (~0.03–0.3%), while Mn, Zn, Rb, Y, Sr and Zr show lower concentrations (0.001–0.08%) (Fig. 7B).

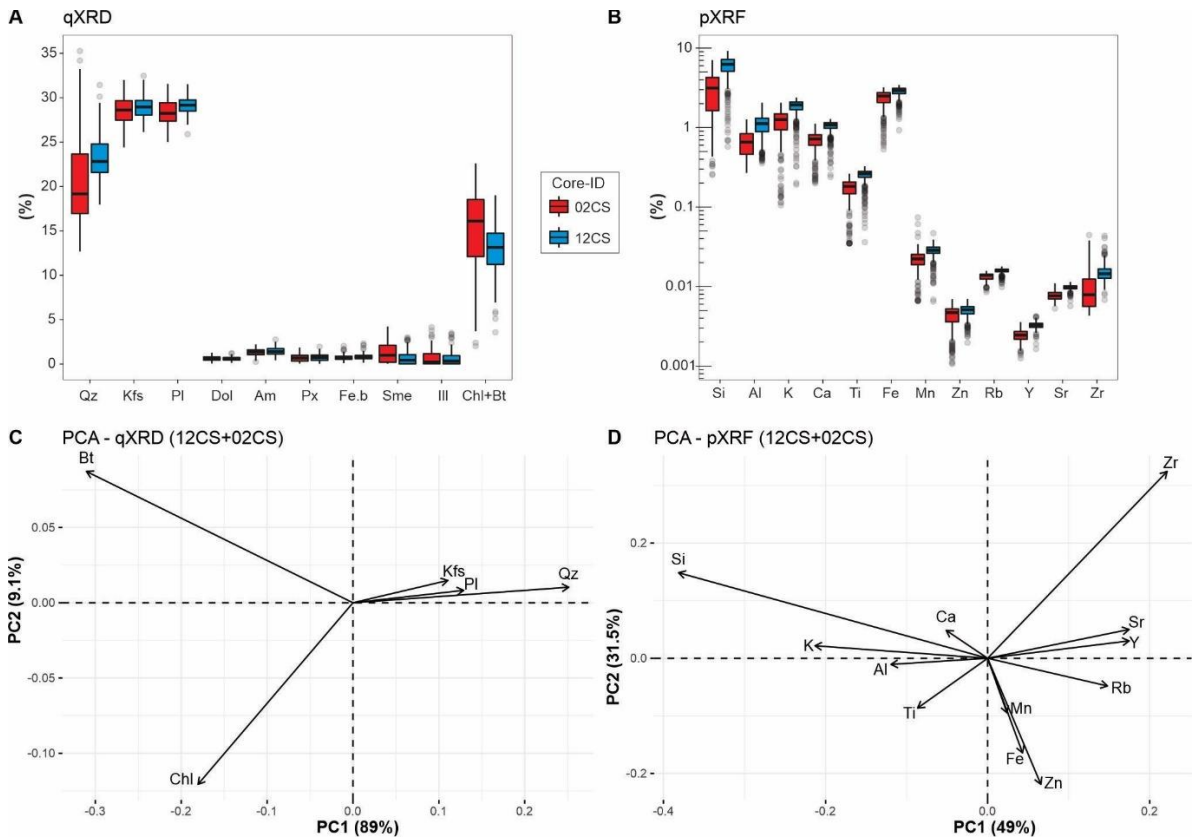


Fig. 7. Results of mineralogical and chemical composition for cores 12CS and 02CS. (A) Boxplot of the distribution of the main minerals (wt.%); (B) boxplot of the chemical composition distribution (%); Note that the relative intensities obtained with the pXRF sensor were converted to percentage (1%=10000 ppm) for better visualization; (C) biplots of the PCA of the bulk mineralogical data; (D) biplots of the PCA of geochemical data.

Because of the similarity in the mineralogical and geochemical compositions of cores 12CS and 02CS (Fig. 7A, B), PCA was conducted with both cores together (Fig. 7C, D). For the two cores, the PCA of the qXRD data indicates that PC1 (89% of the total variance) is positively associated with Pl, Kfs and Qz and negatively associated with Chl and Bt, whereas PC2 (9.1% of the total variance) is positively associated with Bt, Kfs, Pl, and Qz and negatively associated with Chl (Fig. 7C). The PCA of the pXRF data reveals that PC1 (41% of the total variance) is positively associated with Zr, Sr, Rb, Y, Zn, Fe, and Mg and negatively associated with Si, Al, K, Ti, and Ca; PC2 (31.5% of the total variance) is positively associated with Si, Zr, K, Ca, Sr, and Y and negatively associated with Zn, Fe, Rb, Ti, Al and Mg (Fig. 7D).

Based on these results, we selected Chl+Bt/Kfs+Pl and Qz/Kfs+Pl to trace changes of detrital input from the Canadian Shield over time in terms of clay and feldspar mineral inputs (Fig. 11E-F, M-N). Additionally, the log(Fe/Ca) ratio was used to represent variations in terrigenous sediment delivery based on the abundance of Fe in clay minerals and Ca in plagioclase facies (Fig. 11H, P; Adgebie et al., 2003; Croudace & Rothwell 2015). The log(Zr/Zn) ratio was used as a semiquantitative grain size indicator (von Eynatten et al. 2012; Croudace & Rothwell 2015; Wu et al. 2020) with a better vertical resolution than discrete grain size analysis. In this case, Zr is associated with coarse weathering-resistant mineral facies, and Zn is linked with fine-grained clay minerals (Fig. 11G, O). pXRF elemental ratios are presented as log ratios to mitigate the amplitude changes in elemental concentrations caused by variable water contents, grain size distributions and irregularities of the split core surface (e.g., Weltje & Tjallingii 2008).

#### 4.2.Rapidly deposited layers and magnetic properties

Based on physical, magnetic and sedimentological data, 8 rapidly deposited layers (RDLs) were identified in core 12PC, and 6 RDLs were identified in core 02PC (Fig. 8). These RDLs were recognized by low cohesive material with a soupy texture, generally coarse-grained basal layers, upward increase and then decrease in D90 and  $\overline{SS}$  values, low L\* values, peaks

in wet bulk density and  $k_{LF}$ , low basal paleomagnetic inclinations and low  $k_{ARM}/k_{LF}$  values. Lower paleomagnetic inclinations are associated with energetic depositional processes where the magnetic particles are plastered horizontally because of high flow velocity and rapid sediment accumulation (e.g., St-Onge et al., 2004). We identified two types of RDL based on digital X-radiographs and high-resolution grain size analyses (Fig. 9). The first type (RDL 1-3 in core 12CS; Figs. 8,9,11) have a thickness between 15 cm to 25 cm and is recognized by a laminated coarsening-upward unit, followed by a thick fining-upward unit. This type of deposit is interpreted as deposits from hyperpycnal turbidity currents or hyperpycnites (Mulder et al., 2003). The second type (RDL 4-8 in core 12CS and RDLs 1-6 in core 02CS; Figs. 8,9,11) consists of 3 cm to 120 cm-thick fining-upward to homogeneous clayey silt units interpreted as Bouma-type turbidites (Bouma, 1962). This transition is interpreted as the completion of the deposit due to the decrease in flow velocity.

Outside of the RDL's the inclination values oscillate around the expected value for the coring site and were calculated according to the geocentric axial dipole model ( $I_{GAD}$ , 78.17°N for Coronation Fjord), denoting a well-recorded paleomagnetic signal for both cores (Fig. 8; Stoner & St-Onge 2007). The downcore MAD values oscillate at approximately 5° (except in the RDL intervals), which indicates high-quality directional data (Stoner and St-Onge, 2007; Fig 8). The Pseudo-S ratio varies between 0.96 for core 12CS and 0.99 for core 02CS. Values >0.9 indicating low coercivity minerals like magnetite (Stoner and St-Onge 2007).

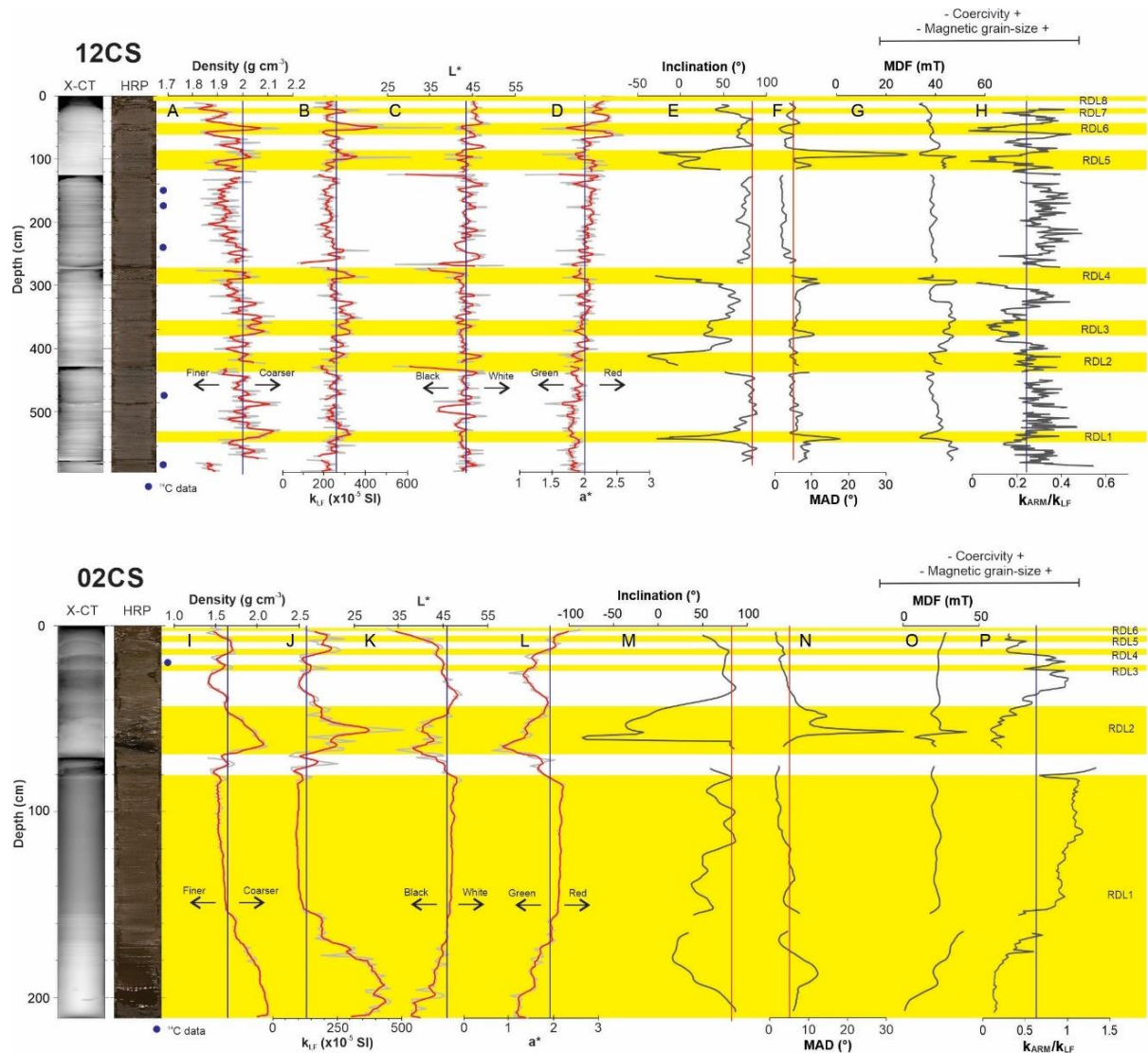


Fig. 8. Downcore variations in cores 12PC and 02PC, showing X-CT images, high-resolution core photography, grain size parameters, IRD counts ( $>2$  mm fraction), wet bulk density, magnetic susceptibility ( $k_{LF}$ ) and magnetic properties (inclination, MAD, MDF and  $k_{ARM}/k_{LF}$ ). RDLs are numbered and highlighted in yellow. The vertical red line delineates a MAD value of  $5^\circ$ . The black vertical line represents the median of the data for each proxy.

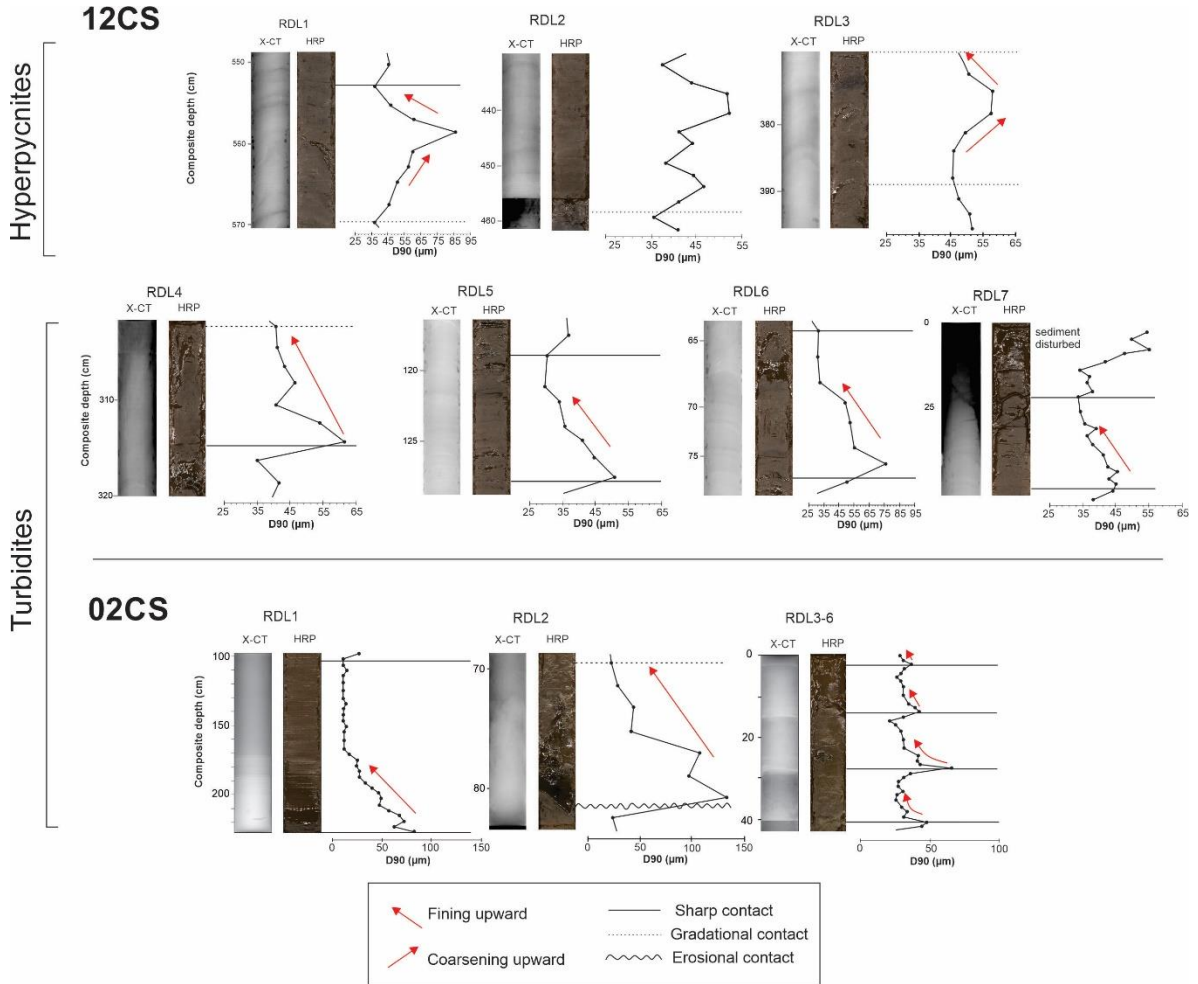


Fig. 9. X-CT scan image, high-resolution core photography and grain size trend (D90) for the fining-upward turbidite and hyperpycnal deposit sequences identified in the cores 12CS and 02CS.

#### 4.3. Chronology

The chronological framework of core 05BC is limited by the occurrence of RDLs. The log(Zr/Zn) and grain size (D90  $\mu\text{m}$ ) data led to the identification of four layers (2–3, 12–14, 23–25 and 36–40 cm; Fig. S1A). As these RDLs are considered to be instantaneous deposits, they were excluded to build an event-free sedimentary record (Fig. S1A).  $^{210}\text{Pb}_{\text{excess}}$  activities

plotted on a logarithmic scale reveal three linear trends that suggest three mean sediment accumulation rates (SARs) of  $0.67 \text{ cm yr}^{-1}$  below 16 cm,  $0.12 \text{ cm yr}^{-1}$  between 11 and 16 cm, and  $0.42 \text{ cm yr}^{-1}$  in the uppermost part of the sequence (0-11 cm; corresponding to the period from 1994 to 2018 CE; Fig. S1A). This age-depth model is well constrained by  $^{239+240}\text{Pu}$  dates and one AMS  $^{14}\text{C}$  date at 18 cm (1955-1958 CE). The  $^{239+240}\text{Pu}$  profile shows an onset of deposition at 18.5 cm and a peak at 16.5 cm (Fig. S1D), which correspond to the years where this radionuclide was introduced into the atmosphere with atmospheric nuclear testing in 1952 and peaked at the height of testing in 1963 (Ketterer et al., 2002, 2004). On this basis, core 05BC spans the last 170 years, from ~1848 to 2018 AD (Fig. S1A). The four RDLs observed in core 05BC are dated to 2013-2015, 1990-1997, 1916-1936, and 1860-1866 CE.

In core 12TWC, the total  $^{210}\text{Pb}$  activity shows “event horizons” with irregular  $^{210}\text{Pb}$  variations that could indicate varying  $^{210}\text{Pb}$  fluxes due to meltwater flood events (Fig. S2; e.g., Xu et al., 2015; Arias-Ortiz et al., 2018). Therefore,  $^{210}\text{Pb}$  data from core 12TWC were not considered in developing the composite age model of core 12CS.

Paleomagnetic chronological markers were obtained by comparing the event-free inclination profiles obtained for each core versus depth to global geomagnetic field models (GUMF1, CALS3k.4, CALS10k.2; Jackson et al., 2000; Korte and Constable, 2011; Constable et al. 2016) or previously published records (Nettilling Lake; Beaudoin et al., 2016). Based on similar shifts in the Earth’s magnetic field behavior in the different records, 6 chronostratigraphic markers (tie points) were determined (Fig. 10 A-D, F-I, Table 3). These tie points were then used in the construction of an age-depth model. The age-depth model indicates that core 12PC spans the last 600 cal a BP, and the calculated sedimentation rates range from  $\sim 0.6 \text{ cm yr}^{-1}$  (626-175 cm depth),  $\sim 0.8 \text{ cm yr}^{-1}$  (175-70cm depth) to  $0.9 \text{ cm yr}^{-1}$  (top 70 cm) (Fig. 10 D, E). Core 02PC spans the last 499 cal a BP, and the calculated sedimentation rate ranges from  $0.06 \text{ cm yr}^{-1}$  (50-20 cm depth),  $0.12 \text{ cm yr}^{-1}$  (20-10 cm depth) and increases to  $0.4 \text{ cm yr}^{-1}$  in the top 10 cm (Fig. 10 I,J).

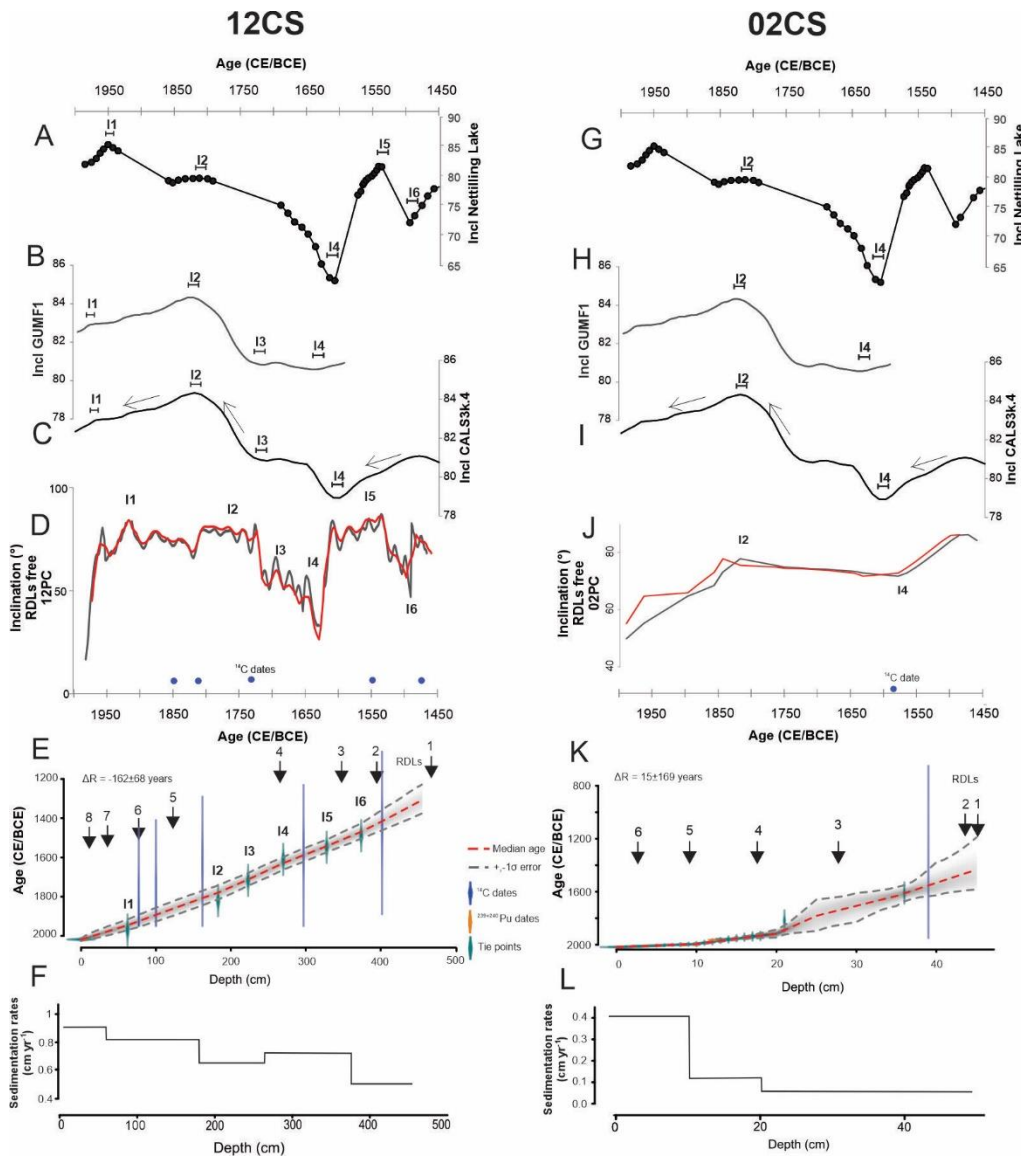


Fig. 10. Comparison of the inclination values from sediment cores (D) 12PC and (J) 02PC compared to (A, G) Nettilling Lake (Beaudoin et al., 2016), (B, H) the GUMF1 (Jackson et al., 2000), and (C, I) CALS3k.4 (Korte and Constable, 2011) geomagnetic field models. (D, J) Composite age model using <sup>210</sup>Pb, <sup>239+240</sup>Pu, and <sup>14</sup>C ages and paleomagnetic tie points. The Bayesian age-depth model was constructed using the R package BACON (Blaauw and Christen, 2011). The red dashed line shows the best age model, and the gray shading represents the chronological uncertainties (95% confidence interval). Black arrows show the RDL ages. (E, J) Estimated sedimentation rates in cm yr<sup>-1</sup>.

Table 3. Paleomagnetic chronostratigraphical markers (tie points) based on the correlation between the 12CS and 02CS cores presented in this study, with other paleomagnetic records (Nettilling Lake, Beaudoin et al. 2016) and geomagnetic field models (GUMF1, Jackson et al., 2000; and CALS3k.4, Korte and Constable, 2011) calculated for the study area.

Tie Points	Depth	Depth	Depth	Depth	Age	GUMF1	Nettilling	Median	SD
	02PC (cm)	02CS* (cm)	12PC* (cm)	12CS (cm)	Cals3K.4		Lake	Age	
	Median (cal. BP)								
I1			62	62	-20	-25	4.4	-20	10
I2	28	21	183	263	130	132.5	127.75	130	10
I3			223	343	230	236		233	10
I4	46	36	270	419	340	319.5	339.6	340	8
I5			328	517			409.1	402	6
I6			374	552			460.9	461	6

\* Depth RDLs free

#### 4.4. Sedimentary units

Sedimentary units were determined on the basis of visual core descriptions, high-resolution core photography, X-CT scan images, physical properties, grain size parameters and mineralogical and geochemical data (Fig. 11). Considering these observations, cores 12CS and 02CS show three and four distinct units, respectively. These units, labeled 1-3 in core 12CS and 02CS from base to top, are described and interpreted below according to core depths (Figs. 11 and 12).

##### 4.4.1. Core 12CS

– **Unit 1** (626-300 cm) is mainly composed of grayish brown (10YR 5/2) clayey silts with brown (10YR 5/3) silty to sandy subcentimeter-scale laminations and disseminated gravel-sized clasts (interpreted as IRD). The gravel-sized clast content decreases toward the top of the unit. Unit 1a (626-550 cm) is characterized by high Chl+Bt/Kfs+Pl and log(Zr/Zn) values and lower Qz/Kfs+Pl and log(Fe/Ca) values (Fig. 11). A cross-laminated interval is found

between 566 and 543 cm and coincides with an increase in D90 and  $\overline{SS}$  values, as well as a decrease in inclination, MDF and  $K_{ARM}/K_{LF}$  ratio values (RDL 1 interval; Fig. 8). Most of the RDLs identified in this unit are of the reverse-to-normal grading type (Fig. 9). A distinct layer with clast that is well stratified is observed between 498 and 480 cm.

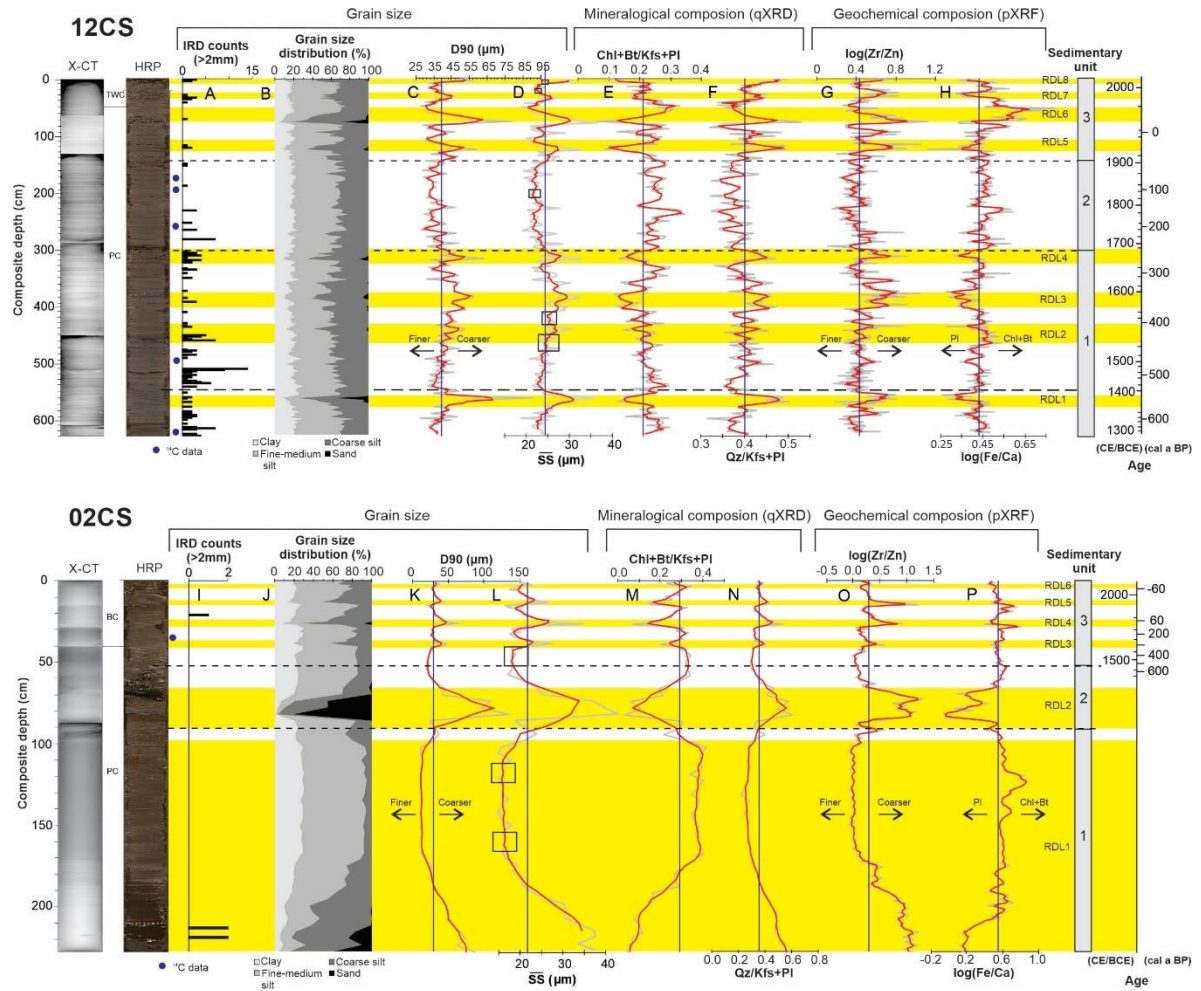


Fig. 11. X-CT scan image, high-resolution core photography, grain size distribution, D90, mean size of sortable silt fraction ( $\overline{SS}$ ), mineralogical and chemical tracers and sedimentary units of cores 12CS and 02CS. RDLs are numbered and highlighted in yellow. The black vertical line represents the median of the data for each proxy. Black boxes indicate sections of the sortable silt record that do not pass the reliability test of a downcore correlation coefficient  $>0.5$  between  $\overline{SS}$  and SS% (McCave & Andrews 2019a).

Core	Units	X-ray	Image	Lithofacies	Colour	Sedimentary structures	D90 ( $\mu\text{m}$ )	Depositional processes	
02CS	Unit 3	0cm 30cm			Mud moderately bioturbated with successions of turbidites	10YR 5/2 grayish brown	Stratified mud; moderately bioturbated	28	Turbidity currents and meltwater plume
	Unit 2	45cm 70cm			Sandy mud	2.5YR 5/2 grayish brown	-Convolute lamination? -Graded toward the top	68	Outburst flood hyperpycnal flow
	Unit 1	100cm 140cm 160cm 203cm			Homogeneous mud  Sandy mud with disseminated clasts	7.5YR 5/2 brown  Intercalations 7.5YR 5/2 brown 7.5YR 5/1 gray	Massive mud. No apparent structure, no bioturbation  -Disseminated clasts -Graded toward the top	13  44	Outburst flood hyperpycnal flow
12CS	Unit 3	60cm 120cm			Laminated mud with IRD	10YR 5/2 grayish brown	Rhythmic succession of clay and silt laminae.	38	Turbidity current, ice rafting and meltwater plume
	Unit 2	200cm 250cm			Laminated mud with absence of RDLs	10YR 5/2 grayish brown	Parallel lamination	35	Meltwater plume
	Unit 1	350cm 400cm 570 cm 590cm			Laminated mud with IRD	10YR 5/2 grayish brown	-Parallel lamination - IRD layer  -Parallel lamination -Cross-laminated -Dispersed IRD	40	Turbidity current, ice rafting and meltwater plume

Fig. 12. Summary of the physical characteristics, average grain size and interpretation of the depositional processes of lithofacies identified in cores 12CS and 02CS.

– **Unit 2** (300-140 cm) is composed of grayish brown (10YR 5/2) laminated clayey silts with brown (10YR 5/3) sediments with low IRD counts. The grain size distribution shows relatively more fine material with below-median values of bulk density, D90,  $\overline{SS}$ , Qz/Kfs+Pl,  $a^*$  and  $\log(\text{Zr/Zn})$  ratios. The unit contains no RDLs, as indicated by a stable signal in paleomagnetic parameters (inclination, MAD and MDF; Fig. 8).

– **Unit 3** (140-0 cm) is composed of grayish brown (10YR 5/2) laminated mud and low IRD abundance. In contrast to Unit 2, Unit 3 is stratified by muddy silt layers that are 1 to 2 cm thick. Unit 3 presents the largest fluctuations in the values of the various measured parameters. Detrital proxies, such as wet bulk density,  $k_{LF}$ ,  $\log(Zr/Zn)$ , and  $\log(Fe/Ca)$ , show high values with occasional spikes (Figs. 8 and 11). These variations coincide with the presence of several RDL intervals of fining-upward type.

#### 4.4.2. Core 02CS

– **Unit 1** (225-100 cm) the interval between 225 to 170 cm is composed of gray (7.5YR 5/1) sandy silts with disseminated IRD that grades toward the top to clayey silts (7.5YR 5/2 brown) that are finely laminated. The gradation in grain-size is corroborated by a decrease in parameters, such as wet bulk density,  $k_{ARM}/k_{LF}$ ,  $Qz/Kfs+Pl$  and  $\log(Zr/Zn)$ , to the top of the record (Figs. 8 and 11). The interval between 170 to 100 cm is mainly composed of homogenous brown (7.5YR 5/2) silty clay. The lower D90,  $\overline{SS}$ , wet bulk density, and  $k_{LF}$  values suggest that the grain size distribution is dominated by a high proportion of fine-grained sediments (Figs. 8 and 11). This interval is also characterized by an increase in  $Chl+Bt/Kfs+Pl$  and  $\log(Fe/Ca)$  ratios and in  $L^*$  and  $a^*$  values. All detrital proxies are constant throughout the interval between 190 to 100 cm, corroborating its homogeneous character. This unit represents the fining-upward RDL type.

– **Unit 2** (100-50 cm) is composed of grayish brown (2.5YR 5/2) sandy mud. The high D90 values dominate at the base of this unit, suggesting a high proportion of medium- to coarse-grained sediments (Fig. 11). The presence of cross-lamination at the base of this unit and normal grading suggest an instantaneous turbidite deposit (e.g., Powell, 1985). This turbidite deposit is also corroborated by a rapid upward increase and then decrease in  $\overline{SS}$  values within the unit, an increase in wet bulk density,  $k_{LF}$ ,  $Qz/Kfs+Pl$  and  $\log(Zr/Zn)$ , and the fact that these values gradually decrease toward the top of the record (Figs. 8 and 11). This interval is also accompanied by shifts to low inclination and  $k_{ARM}/k_{LF}$  values.

– **Unit 3** (50-0 cm) is composed of grayish brown (10YR 5/2) mud that is moderately bioturbated (based on the X-CT scan images). Moreover, this unit is characterized by the presence of a succession of RDLs. The coarser base of each RDL is visible on the X-CT scan images. These intervals are characterized by a rapid upward increase and then decrease in coarse silts, fine sands,  $\overline{SS}$ , Qz, Kfs+Plg and log(Zr/Zn) (Fig. 11), which can be interpreted to reflect the waxing followed by waning flow conditions during large glaciogenic meltwater discharge events. Thus, the presence of these RDLs suggests that glacial turbidite plumes dominated in this interval.

## 5. Discussion

### 5.1. Sediment provenance

In general, the ternary plot of total Qz-Chl+Bt-Kfs+Pl illustrates that sediment samples from cores 12CS and 02CS are enriched in Kfs+Plg and Qz, with lower contents of Chl+Bt. Furthermore, this ternary plot reveals a similar mineral composition in both ice-proximal (12CS) and ice-distal (02CS) zones of Coronation Fjord (Fig. 13). These results suggest a homogeneous detrital input over time with a composition that is characteristic of the Cumberland Batholith, which is composed mainly of charnockite, monzogranite and granodiorite (Clarke & Upton, 1971; Jackson and Berman 2000; St-Onge et al. 2009). This basement extends throughout the entire region, and therefore, it is not possible to discriminate the variations in the detrital contribution of each fjord in core 02CS (Fig. 5A). Although all samples are homogeneous from a mineralogical point of view, there is a slight increase in the Chl+Bio content in core 02CS, likely reflecting the greater hydrodynamic capacity of the clays to be transported to more distal zones.

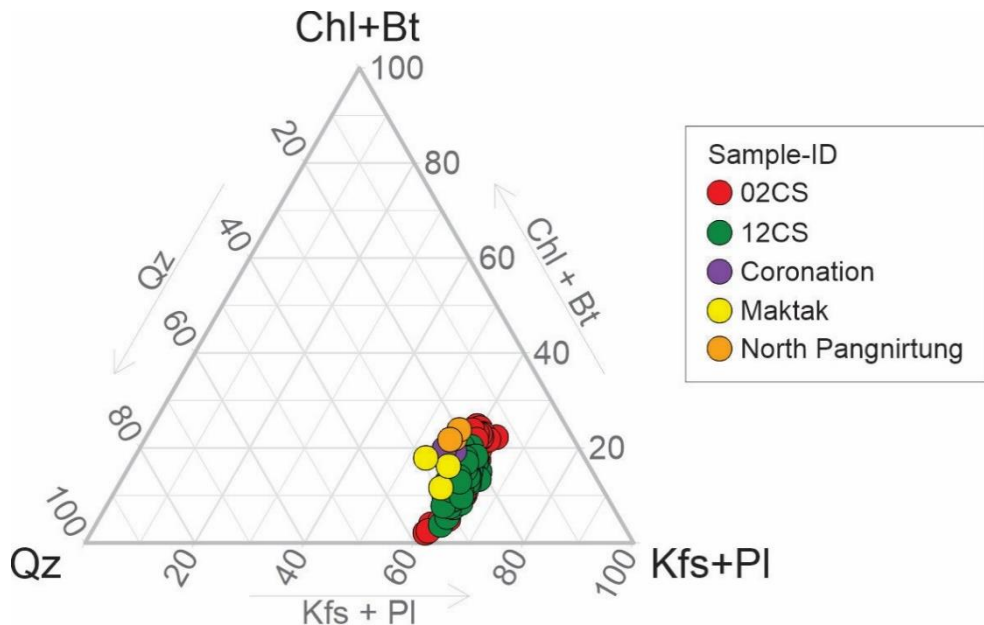


Fig. 13. Quartz (Qz) – chlorite+biotite (Chl+Bt) – K-feldspar+Plagioclase (Kfs+Pl) ternary plot, including sediment samples of cores 12CS and 02CS. The mineralogical data of surface sediments from the Coronation, Maktak and Pangnirtung fjords are from Andrews et al. (2018) and Andrews (2019).

### 5.2. Sedimentological interpretation of rapidly deposited layers

Detrital proxies from cores 12CS and 02CS suggest that RDLs occur frequently in both ice-proximal (8 RDLs) and ice-distal (6 RDLs) environments of Coronation Fjord as well as over time (Figs. 8 and 11). However, there are different triggering mechanisms that may be responsible for RDL deposition in these proximal and distal glacial settings. In the ice-proximal environment, several glacial sedimentary processes, such as glaciogenic debris flows, icebergs and sea ice rafting, meltwater plumes and turbidity currents, can influence marine sedimentation (Powell, 1985; Cowan and Powell, 1991; Ó Cofaigh et al. 2013; Dowdeswell et al. 2015). The sub-bottom profile in ice-proximal environment (Fig. 5D) is characterized by high amplitude parallel laminations, demonstrating that the sedimentation in this setting is mainly controlled by continuous sediment input from meltwater inflow. In core 12CS, all RDLs are characterized by finely laminated glaciomarine sediments that are

rich in Qz, Kfs and Pl. However, the structure of the RDLs 1-3 is typical of hyperpycnites, with a reversely graded deposit, followed by a normal graded unit (Figs. 9 and 11C-D). This type of deposit is formed from flood-induced currents carrying a high load of particles, generating a dense flow of water or a hyperpycnal flow (e.g. Mulder and Syvitski, 1995; Mulder et al., 2003; Duboc et al., 2017). These flows can occur during a single cycle of glaciogenic meltwater discharge as well as during river floods caused by seasonal and/or catastrophic events. Thus, the hyperpycnites are composed of an inversely graded (waxing flow) basal unit, followed in transition by a normally graded (waning flow) unit (e.g. Mulder et al., 2003; St-Onge et al., 2004). Conversely, the structure of the RDLs 4-8 is typical of turbidites (Figs. 9 and 11C-D). In these cases, the flood-induced currents decelerating with time, deposit the so-called normally graded Bouma sequence (Bouma, 1962). Hence, we speculate that the hyperpycnites were probably deposited by hyperpycnal flows of rock flour-laden meltwater associated with the advance and/or retreat of the Coronation Glacier. In fact, glacial erosion typically generates a large amount of glaciogenic sediment (rock flour), which can then be transported by meltwater streams and by hyperpycnal currents into the fjord (e.g., Dowdeswell et al. 2015; Stevenard et al., 2022). In addition, enhanced calving activity in an ice-proximal environment can generate turbulence in the fjord floor, which in turn promotes submarine landslides and gravity flows (Powell, 1985; Normandeau et al. 2021). This mechanism could also have influenced the sedimentary dynamics during the deposition of RDLs 1 to 4 in Unit 1 of core 12CS, where the abundance of IRD suggests enhanced calving activity (Fig. 11A).

In the ice-distal environment (core 02CS), RDLs 1 and 2 are coarser-grained deposits with low L\* and a\* values (suggesting dark sediments that are rich in organic matter; Debret et al., 2011; Fig. S7) and significant thickness (38-42 cm). The sedimentological features of these RDLs suggest the rapid deposition of a large amount of sediment in the fjord that could be associated with glacial outburst flood events (GOFs; Emmer et al., 2017). In glacier-influenced fjords, GOFs are caused by the catastrophic drainage of proglacial lakes from the retreat of ice sheets (e.g., Emmer et al., 2017; Vandekerkhove et al., 2021). These deposits are also identified in the sub-bottom profile of the ice-distal environment (Fig. 5E), which

are characterized by transparent acoustic facies, with a higher frequency towards the top. However, intense precipitation, rain-on-snow events, or high seasonal meltwater discharge can also result in sediment discharge peaks and potentially in outburst floods (Vandekerkhove et al., 2021, Liu et al., 2021). In Chilean Patagonia, recent studies show that GLOFs are recorded in downstream fjord sediments as fine-grained and organic-poor layers, representing the high amount of glacier rock flour transported during lake outbursts, whereas meteorological floods are represented by coarser and organic-enriched deposits (Vandekerkhove et al., 2021, Liu et al., 2021). Since the Coronation Fjord context is similar to Chilean Patagonia, and considering the sedimentological characteristics of RDLs 1 and 2, we speculate that the meteorological floods seem to be the main triggering mechanism of these RDL deposits. On the satellite images (Fig. 5A) it is possible to distinguish an upper sandur delta formed in North Pangnirtung Fjord, which is blocked by a large deposit, previously interpreted by Dyke (1982) as a ground moraine. This interpreted ground moraine is incised by a fluvial channel. It is possible that the sandur delta north of this deposit filled a lake, the latter episodically leading to outbursts, forming the GLOFs at the intersection of the three fjords. Alternatively, the GOFs could also originate from subglacial meltwater discharges from Coronation or Maktak Fjords. This is less evident for RDLs 3 to 6 in core 02CS (Figs. 8 and 11). Indeed, the sedimentological features (i.e., laminated muds that are rich in Qz, Kfs and Pl), low thicknesses (1-3 cm) and high frequency of these RDLs seem to indicate that turbid hyperpycnal meltwater plumes sourced from the three fjords (Coronation, Maktak and North Pangnirtung) are driving these events.

There are also some physical factors (e.g., seafloor morphology, slope, presence/absence of channels, and ice fluxes) that may favor the occurrence of outburst floods and turbidity currents in the distal environment in Coronation Fjord. The position of core 02CS at the junction of the three fjords probably records sediment inputs from all of them. Satellite images show that large sediment plumes can influence sedimentation at the location of core 02CS (Fig. 5A). Likewise, Maktak and North Pangnirtung Fjords are considered to be mature because their glaciers have receded and present large sandur surfaces (Gilbert, 1983). The exposed sediments from the sandur surfaces are susceptible to easy remobilization and

transport by freshwater inputs from winter remnant glacier melt and rain storms (Syvitski and Shaw, 1995). Therefore, sediment delivery in Maktak and North Pangnirtung Fjords may be even higher than in Coronation Fjord. This can be evidenced by the highest values of log(Fe/Ca) in the core 02CS compared to the 12CS (Fig. 11H, P). Indeed, an enhanced input of iron-bearing sediments from the sandur surface can increase the Fe concentrations in the sediments supplied to the distal zone. In this context, we hypothesize that more intense warm summer periods probably promoted large hyperpycnal flows of sediment-laden glacial meltwater in the three fjords, which in turn generated turbidite deposits in the conjunction zone (Figs. 5A and 16). Moreover, the conjunction zone is preceded by a slope of ~4.57°, which can favor the transport of gravity flows into the deeper zone of the basin (Pope et al., 2019). The formation of scour structures along the slope (Fig. 5C) indicates a significant current flow along the slope, which can also promote turbidite deposits (Ben Meftah et al., 2020). Thus, it is evident that turbidites, gravity flows and meteorological outburst floods are important sediment delivery mechanisms in Coronation Fjord. However, more studies of the bathymetry of the Maktak and North Pangnirtung Fjords are needed to determine whether other physical bathymetric features may control sediment transport into the fjord.

### 5.3. Depositional processes during the Late Holocene

The variations in the detrital proxies in the ice-proximal (12CS) and ice-distal (02CS) composite cores are used to explore the potential impacts of the Little Ice Age (LIA; ~1350–1850 CE; Jones & Mann 2004) and modern warming (MW; late 1800s CE; Jones & Mann 2004; Kaufman et al., 2009) on the sedimentary dynamics in these glacimarine environments.

Colder conditions associated with the LIA were regionally established on Baffin Island (e.g., Moore et al., 2001; Thomas and Briner, 2009; Kaufman et al., 2009; Miller et al., 2012). In core 12CS, the higher gravel-sized clast contents observed between ~1400 and ~1600 CE suggest a marked increase in the delivery of coarse-grained sediment by iceberg rafting at this time (Fig. 14F). The presence of laminated sediments and coarse ice-raftered clasts throughout the LIA interval (Unit 1 and the base of Unit 2) suggests that the sedimentary regime in Coronation Fjord was influenced by successive episodes of snowmelt runoff and

turbid hyperpycnal meltwater plumes during spring/summer, as well as by increased iceberg calving activity of the Coronation Glacier. Previous Arctic paleoclimate studies (Kaufman et al., 2009; Thomas and Briner, 2009; Beaudoin et al., 2016; Lapointe et al., 2020) and climate model simulations (Crespin et al., 2009) provide evidence for short-term warming superimposed over general LIA cooling between ~1375 and ~1575 CE that was driven by the enhanced advection of warm air and Atlantic water to the Arctic (Kinnard et al., 2011; Miller et al., 2012). In this context, we argue that warmer Arctic air temperatures together with extended melt seasons during this warm phase of the LIA promoted a substantial increase in calving activity in the Coronation Glacier (Fig. 16A). Conversely, the decreasing in IRD content observed between 1600 and 1850 CE in core 12CS (Fig. 14F) support the idea that colder LIA temperatures established during this period promoted a greater glacier growth in the region. A glaciological study performed in Divide Ice Cap (Pendleton et al., 2017), a small ice cap located close to Coronation Fjord (Fig. 5A), suggest that cold climatic conditions established before and during the LIA promoted episodic advances in this ice cap at ~1000 CE, ~1200, and ~1500 CE, which led to the maximum Neoglacial dimensions ~1900 CE, in line with our interpretations.

Furthermore, the Chl+Bt/Kfs+Pl and log(Zr/Zn) profiles in cores 12CS and 02CS show a similar pattern of variations with those of the Ti record from Nettilling Lake (Beaudoin et al., 2016), melt feature anomalies from the PIC (Fisher et al., 1998), reconstructed Atlantic Multidecadal Oscillation (AMO) index values (Lapointe et al., 2020) and surface air temperature (SAT) anomalies in the Arctic (Kaufman et al., 2009) (Fig. 14). Indeed, high Chl+Bt and Zn contents and low IRD inputs recorded in core 12CS during the LIA correspond to a dominance of the negative AMO phase, colder Arctic SAT, and reduced summer PIC melt rates (Fig. 14). This good correspondence suggests that at multidecadal to centennial timescales, the sedimentary dynamics in Coronation Fjord during the preindustrial period may have been modulated by internal coupled atmosphere-ocean-ice interactions.

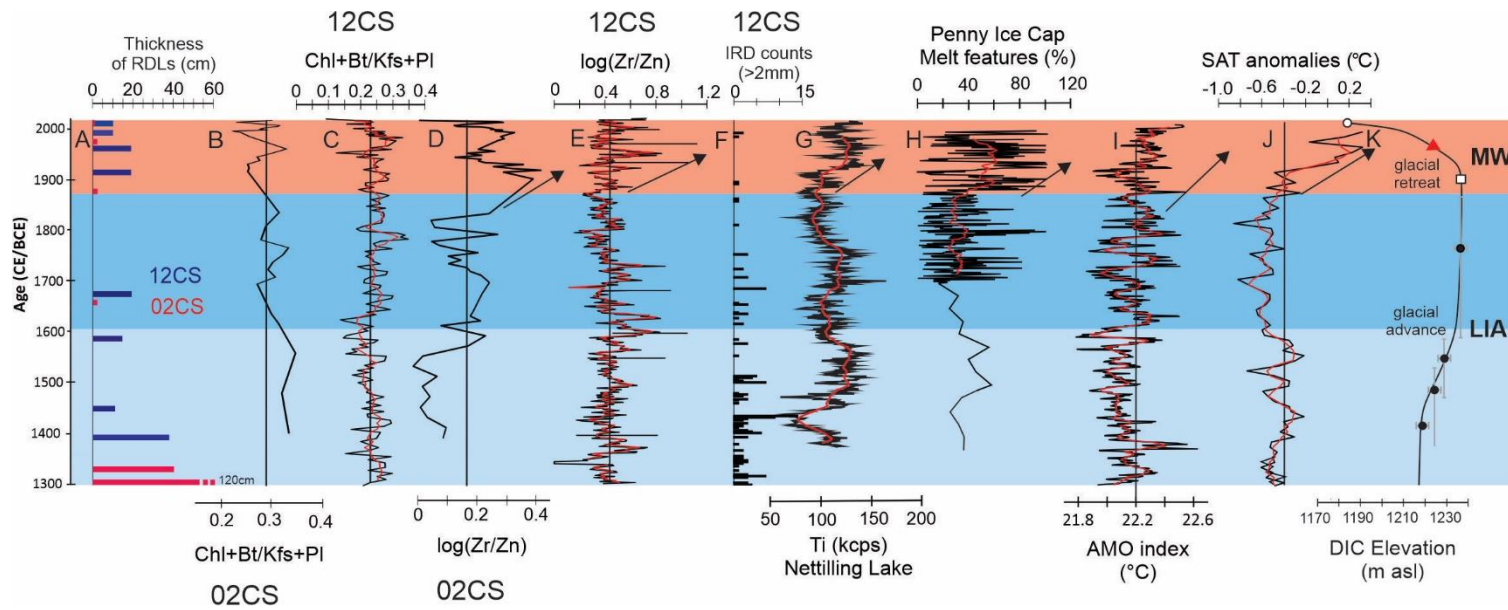


Fig. 14. Comparison of detrital proxies used in this study for cores 12CS and 02CS during the Late Holocene with paleoenvironmental proxies. (A) Thickness of RDL (blue bars: 12CS; red bars: 02CS); (B-C) Chl+Bt/Kfs+Pl; (D-E) log(Zr/Zn), (F) IRD count in core 12CS ( $>2$  mm); (G) Ti (kcps) measured in core sediment from Nettilling Lake (Beaudoin et al., 2016); (H) melt feature (MF) anomalies from the Penny Ice Cap (PIC; Fisher et al., 1998); (I) reconstructed Atlantic Multidecadal Oscillation (AMO) index (Lapointe et al., 2020); (J) surface air temperature (SAT) anomalies in the Arctic (Kaufman et al., 2009). (K) inferred ice margin elevation of the Divide Ice Cap (DIC) located close to the Coronation Fjord (Pendleton et al., 2017). The position of the DIC margin was interpreted from radiocarbon ages of plants (black circles), aerial photography (triangle), and observed 2015 position (circle). The Neoglacial maximum DIC extent is also shown (square). asl = above sea level. The black vertical line represents the median of the data for each proxy.

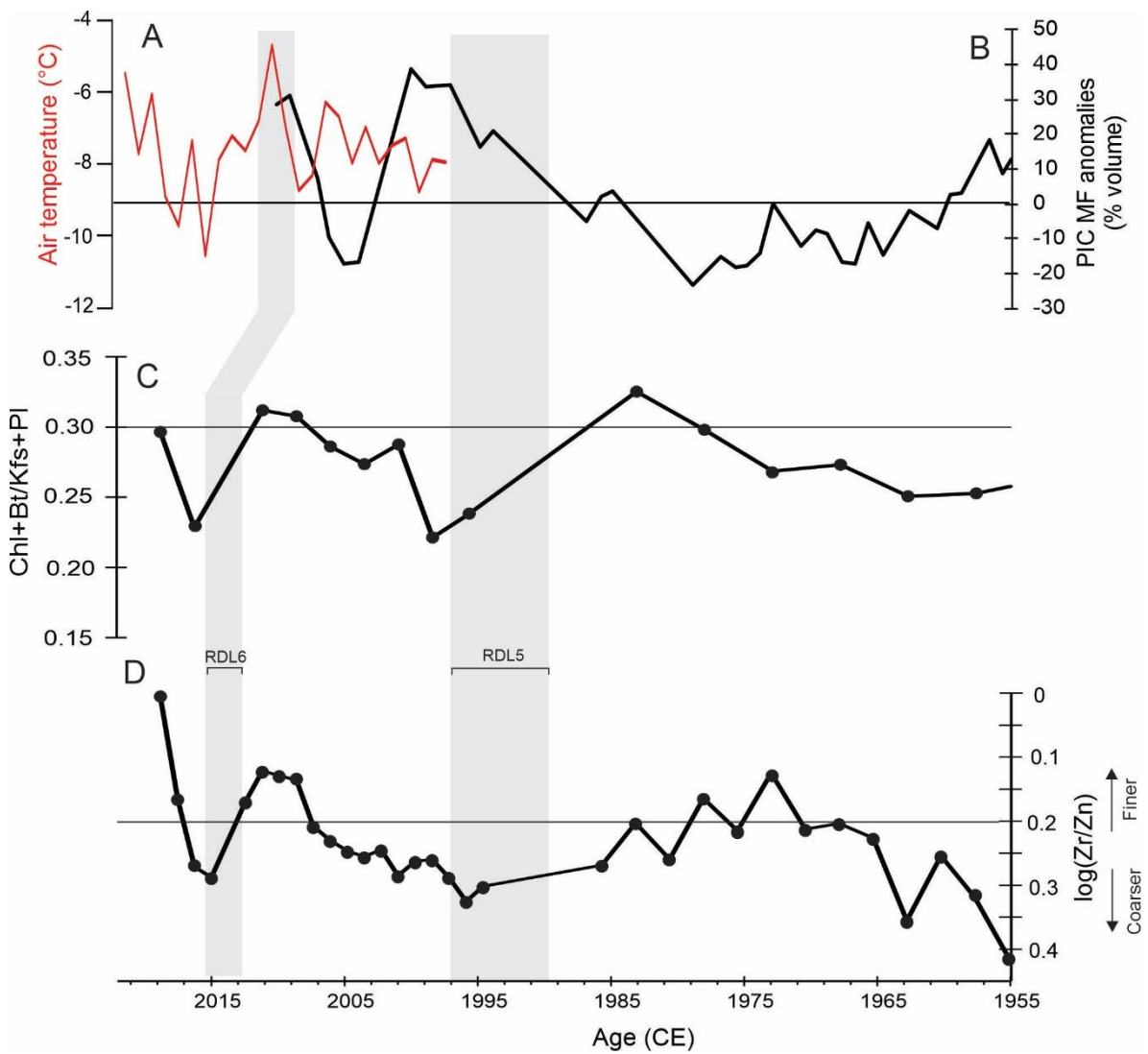


Fig. 15. Comparison of the (A) historical air temperature data of Pangnirtung Nunavut (source: <https://climat.meteo.gc.ca>) and (B) melt feature (MF) anomalies from the Penny Ice Cap (PIC; Zdanowicz et al., 2012), with (C) Chl+Bt/Kfs+Pl, (D)  $\log(\text{Zr}/\text{Zn})$  profiles from core 05BC (top of 02CS). The horizontal line represents the median of the data for each proxy. The  $\log(\text{Zr}/\text{Zn})$  scale was inverted for better comparison with the other proxies. Note that the difference in the timing between of peaks of melt feature anomalies from the PIC and the sedimentary records can reflects uncertainties in the individual chronology methods and/or a lag of the sediment response.

The higher sedimentation rates ( $\sim 0.9 \text{ cm yr}^{-1}$  in core 12CS and  $0.4 \text{ cm yr}^{-1}$  in core 02CS; Fig. 10) and the greatest variations in our detrital proxies are observed since  $\sim 1850 \text{ CE}$  (Figs. 14 and 15) and suggest an increase in snowmelt runoff and glacial meltwater plumes from the northeastern PIC margin, probably related to the influence of modern warming trend (Kaufman et al. 2009; Zdanowicz et al., 2012). The increase in the coarse silt contents and  $\log(\text{Zr/Zn})$  ratios, together with the low Chl+Bt/Kfs+Pl ratios and IRD contents since  $\sim 1850 \text{ CE}$ , suggest that glacial meltwater outwash (composed mainly of silt-sized particles) impact sedimentation in Coronation Fjord. Indeed, the landward retreat of marine-terminating glaciers promotes the formation of glacial outwash plains and deltas at the glacial front (Powell, 1981). In this setting, glacial meltwater streams can introduce a mixture of fine-grained sand and glacial flour silts over fan deltas and in more ice-distal marine locations (Powell, 1981; Dowdeswell et al., 2015; Stevenard et al., 2022). Similarly, during the winter season, rapid ice formation in shallow water areas at the head of the fjord can foster the recurrent incorporation of proglacial outwash sediments into both sea ice via suspension freezing and anchor ice (e.g., Reimnitz et al., 1987) (Fig. 16B). Then, these sediments are entrained by surface currents in the fjord during the spring season. In this context, we hypothesize that the sedimentary regime in Coronation Fjord during the industrial period (1850 CE to present) was mainly driven by both an enhanced input of glacial meltwater outwash and the transport of sediment-laden sea ice through the fjord related to a landward retreat of the northeastern PIC margin. In addition, the similar trend observed between the Chl+Bt/Kfs+Pl and  $\log(\text{Zr/Zn})$  ratios from core 05BC with summer PIC melt rates (Fig. 15) supports the idea that increased in atmospheric temperatures observed since 1980 CE (linked to anthropogenic-induced Arctic amplification; Kaufman et al., 2009) are an important factor driving the increase in summer ice melt rates of ice caps and glaciers on Baffin Island during the industrial period (e.g., Moore et al., 2001; Zdanowicz et al. 2012; Beaudoin et al., 2016; Cook et al. 2019). In addition, the most recent turbidite observed in core 02CS (RDL 6: 2013-2015 CE) may have been triggered by a marked increase in air temperature recorded for the region in 2010 (Fig. 15A). This also agrees with a decrease in the PIC mass balance for the

period 2005-2014 (Schaffer et al., 2017). Thus, our results corroborate that the sedimentary dynamics of the Coronation Fjord is high-fidelity to modern climate observations and represent a high-quality paleoclimate archive.

The occurrence of RDLs also correlates with the regional climatic variations (Fig. 14A). During the LIA, the thick RDLs in cores 12CS and 02CS (~20 to 120 cm thick) show a frequency of ~1 RDL per century, while the RDLs record in the 20<sup>th</sup> century are characterized by thinner but more frequent RDLs (~7 RDLs per century and ~10 to 20 cm thick; Fig. 14A). These results suggest an increased frequency of RDLs during the MW compared to the LIA, likely related to increased summer ice melt rates of the northeastern margin of the PIC. However, as RDLs have erosion/transport potential and may lead to erosion of underlying RDLs (particularly RDL 1 and 2 in core 02CS), this interpretation needs to be taken with caution. Regardless, these results highlight the strong glaciological and hydrometeorological component in the triggering, intensity and frequency of the RDL deposits along Coronation Fjord.

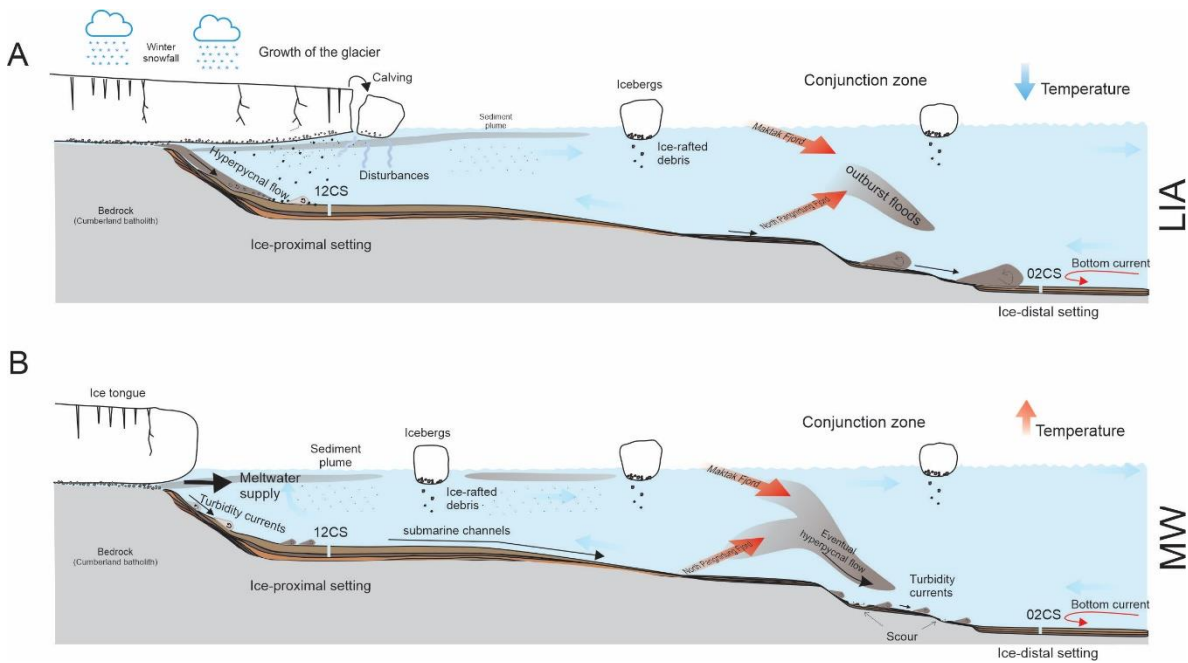


Fig. 16. Schematic models of sedimentary processes and environmental conditions in Coronation Fjord during (A) the LIA, warmer episodes during generated increased iceberg calving activity, increasing the concentration of IRD and turbidite deposits in an ice-proximal setting; successive episodes of high seasonal meltwater discharge resulted in outburst floods deposited in an ice-distal setting; and (B) MW, in which warmer conditions promote the input of glacial meltwater outwash, sediment-laden transport and turbid hyperpycnal flow formation in ice-proximal and ice-distal settings.

## 6. Conclusions

The multiproxy study on the two sediment cores (12CS and 02CS) recovered along Coronation Fjord allowed us to trace the evolution of the sedimentary dynamics of the PIC, as well as document glaciological processes and environmental conditions during the late Holocene. Overall, the results of this study yield the following generalizations and conclusions:

- The combination of radiometric ( $^{210}\text{Pb}$ ,  $^{239+240}\text{Pu}$  and  $^{14}\text{C}$ ) and paleomagnetic dating techniques allowed the establishment of a robust chronostratigraphical framework for composite cores 12CS and 02CS, which span the last 600 cal a BP, respectively. Core 12CS has a sedimentation rate that ranges from 0.6 to 0.9 cm yr $^{-1}$ , which makes it a unique high-resolution sedimentary record for the region.
- Physical, mineralogical and geochemical signatures of sediment cores revealed 8 RDLs in core 12CS and 6 in core 02CS. In the ice-proximal environment (core 12CS), these RDLs are most likely triggered by hyperpycnal flows of rock flour-laden meltwater (RDL 1 to 3) and turbidity current (RDLs 4 to 8). While in the ice-distal environment (core 02CS), the RDLs are likely to be generated by meteorological outburst floods (RDLs 1 and 2) and by turbid hyperpycnal meltwater plumes (RDLs 3 to 6) sourced from Coronation, Maktak and North Pangnirtung Fjords. The RDLs are more frequent during both the cold LIA and the warmer 19<sup>th</sup>-20<sup>th</sup> century periods and are likely the result of enhanced summer ice melt rates of the northeastern PIC margin, respectively.
- The ternary plot Qz-Chl+Bt-Kfs+Pl reveals a homogeneous detrital input with a composition that is characteristic of the Cumberland batholith, and therefore, our mineralogical proxies are unable to discriminate the sediment provenance from North Pangnirtung, Coronation and Maktak Fjords.
- The presence of laminated sediments and coarse ice-rafterd clasts throughout the LIA period in core 12CS reveal that colder LIA conditions promoted glacier growth as well as successive episodes of turbid hyperpycnal meltwater plumes during spring/summer and increased iceberg calving activity in Coronation Fjord.
- The higher sedimentation rates (~0.9 cm yr $^{-1}$  in core 12CS and 0.4 cm yr $^{-1}$  in core 02CS), the increase in the coarse silt contents and the high frequency of RDLs observed since ~1850 CE are interpreted as indicating an accelerated retreat of the Coronation Glacier and enhanced summer ice melt rates from the northeastern PIC margin due to 19<sup>th</sup>-20<sup>th</sup> century warming.

- Similar trends observed between our detrital proxies and summer melt features recorded from the PIC, AMO index values and Arctic SAT anomalies suggest high connectivity between atmospheric and ocean temperature variations and the sedimentary dynamics of the Coronation Glacier during the last 600 years.

## 7. Acknowledgments

We are grateful to the captain, officers, crew and scientists on board the CCGS Amundsen during the 2018 and 2019 ArcticNet expeditions for the recovery of cores used in this study. We also thank Quentin Beauvais (ISMER-UQAR), Dominique Lavallée, (ISMER-UQAR) and Claude Belzile (ISMER-UQAR) for their technical support and advice in the laboratory, and Camille Brice (ISMER-UQAR) for the drawing up of Fig. 1. We also thank André Pellerin (ISMER-UQAR) and Matt O'Regan (Stockholm University) for their insightful comments on an earlier version of the manuscript as well as the American Journal Experts for the support with the English editing. This research was funded by ArcticNet (a Network of Centres of Excellence Canada), Geotop, Québec-Océan, CREATE ArcTrain program, and the Natural Sciences and Engineering Research Council of Canada (NSERC) through Discovery Grants to J.-C. Montero-Serrano and G. St-Onge. All analytical data presented will be available electronically in the PANGAEA database (<https://www.pangaea.de/>).

## CONCLUSION GÉNÉRALE

Dans le cadre de ce projet de maîtrise, deux séquences sédimentaires composites (12CS et 02CS) échantillonnées le long du Fjord Coronation ont été étudiées afin de déterminer la composition des sédiments et des lithofaciès ainsi que de reconstituer les changements à long terme des transferts sédimentaires à partir de la calotte glaciaire Penny (CGP).

Les signatures minéralogiques révèlent un apport détritique homogène dominé par le feldspath (Kfs), le plagioclase (Pl) et le quartz (Qz) dont la composition est caractéristique du batholite de Cumberland, lequel est principalement composé de charnockite, de monzogranite et de granodiorite (Clarke & Upton, 1971; Jackson and Berman 2000; St-Onge et al. 2009). Par conséquent, la variation des traceurs détritiques au cours du temps a été interprétée comme des changements dans la dynamique sédimentaire directement liés aux périodes de retrait ou d'avancée du glacier Coronation et de la marge nord-est de la CGP.

Les traceurs détritiques et les propriétés magnétiques des carottes 12CS et 02CS ont permis d'identifier respectivement 8 et 6 couches déposées rapidement (rapidly deposited layers; RDLs). Cependant, il existe différents mécanismes de déclenchement responsables du dépôt de RDLs dans les environnements glaciaires proximal (12CS) et distal (02CS). Les RDLs de la carotte 12CS sont caractérisés par des sédiments glacio-marins finement laminés et riches en Qz, Kfs et Pl, probablement déposés par des écoulements hyperpycniques d'eau de fonte chargée de farine de roche associés à l'avancée et/ou au retrait du glacier Coronation. De plus, une activité de vêlage accrue dans un environnement proximal (peu profond) peut entraîner des perturbations dans le fond du fjord, ce qui pourrait favoriser les glissements de terrain sous-marins et les écoulements gravitaires. À l'inverse, dans l'environnement glaciaire

distal, les RDLs sont caractérisées par un grain plus grossier, une teneur en matière organique plus élevée et une épaisseur plus importante. Ainsi, cela suggère que des précipitations intenses, des épisodes de précipitations ou un débit élevé d'eaux de fonte saisonnières aient pu entraîner des pics de décharge de sédiments et, éventuellement, des crues météorologiques. Dans l'environnement distal du fjord Coronation il existe également des facteurs physiques qui peuvent favoriser l'apparition de crues soudaines et de courants de turbidité : 1) la conjonction et les apports sédimentaires des trois fjords adjacent (Coronation, Maktak et North Pangnirtung); 2) les fjords Maktak et North Pangnirtung ont des grandes surfaces de sandur où les sédiments subissent une remobilisation et un transport facile et 3) la zone de conjonction (carotte 02CS) est précédée d'une pente d'environ 4,57° qui peut favoriser le transport des flux gravitaires vers la zone plus profonde du bassin.

Les mesures des propriétés physiques et sédimentologiques révèlent un contraste dans les unités sédimentaires entre les carottes dans un environnement glaciaire distal (02CS) et proximal (12CS). Pendant la période de la Petit Âge Glaciaire (PAG; ~1350-1850 CE) ont été établis des conditions plus froides. La prédominance de particules détritiques à grains moyens à fins et la forte présence de débris délestés par les icebergs (ice rafted debris; IRD) dans la carotte 12CS, suggèrent que ces conditions climatiques froides ont favorisé la croissance du glacier et une augmentation du ruissellement en provenance de la fonte des neiges et des panaches d'eau de fonte pendant la saison de printemps/été ainsi qu'augmentation de l'activité de vêlage des icebergs. Finalement, de 1850 à aujourd'hui, les plus fortes variations dans les conditions de sédimentation sont caractérisées par une augmentation de la taille des grains, du rapport log(Zr/Zn) et des taux de sédimentation (~0.9 cm an<sup>-1</sup> dans la carotte 12CS et 0.4 cm an<sup>-1</sup> dans la carotte 02CS. Ces caractéristiques indiquent une augmentation de l'apport détritique associée à une accélération de la fonte de la marge nord-est de la CGP en raison du réchauffement climatique moderne. Les écoulements glaciaires chargés de sédiments forment des courants hyperpicnites et constituent probablement le mécanisme déclencheur des dépôts de RDL au cours de cette période. La covariabilité entre les traceurs détritiques des carottes 12CS et 02CS et la

variabilité de l'indice de l'oscillation multidécennale de l'Atlantique (AMO), l'enregistrement holocène de Ti du lac Nettiling, les taux de fonte de la CGP, et les anomalies de la température de l'air en surface (SAT) dans l'Arctique, sont évidentes pendant l'enregistrement instrumental. Cette bonne correspondance suggère que la dynamique sédimentaire dans le fjord Coronation pendant la période préindustrielle a pu être modulée par des interactions internes couplées atmosphère-océan-glace.

Les sédiments marins à l'extérieur du fjord de Coronation sont caractérisés par une faible concentration des carbonates biogéniques (ex., foraminifères et coquilles de mollusques), ce qui limite la construction d'un modèle d'âge dans cette partie du fjord. Dans ce contexte, l'une des contributions les plus importantes de ce travail a été le développement de deux modèles d'âges, combinant des données de  $^{210}\text{Pb}$  et  $^{239+240}\text{Pu}$  (carotte 05BC), des âges radiocarbone et des marqueurs paléomagnétiques, pour des séquences sédimentaires recueillies le long du fjord de Coronation. Ces séquences sédimentaires constituent ainsi deux nouvelles archives paléoclimatiques couvrant la période de l'Holocène tardif dans l'est de la baie Baffin.

Dans l'ensemble, cette étude multi-traceurs a permis de reconstituer l'apport des sédiments de la CGP influencé par les changements climatiques au cours de l'Holocène tardif. Cependant, des analyses similaires à la présente étude sont recommandées pour les carottes à gravité prélevées dans les fjords Maktak, Coronation et nord de Pangnirtung au cours de l'expédition « Sedimentology of Arctic Fjords Experiment (S.A.F.E.) » menée par la Commission géologique du Canada à bord du NGCC Hudson en 1982 (Syvitski et Schafer, 1985). Cela permettra de compléter les interprétations de la dynamique sédimentaire de chacun de ces fjords et d'améliorer la compréhension des apports sédimentaires de chacun d'eux dans la zone de conjonction (site de la carotte 02CS). Elle permettra également d'élargir les connaissances sur la dynamique de la marge nord-est de la CGP.

Bien que les âges réservoirs calculés dans cette étude soient en accord avec les âges réservoirs calculés pour la région (Coulthard et al., 2010), des analyses de  $^{14}\text{C}$  sur des foraminifères planctoniques et benthiques d'un même échantillon sont recommandées. Cette technique permettra de dériver un enregistrement de l'évolution dans le temps des âges réservoirs (valeurs  $\Delta^{14}\text{C}$ ) et ainsi une chronologie robuste pour les enregistrements de sédiments marins dans la région (ex. Sarnthein et al., 2015). Toutes ces recommandations pourraient améliorer le modèle d'âge pour les carottes étudiées dans ce travail de maitrise ainsi que les interprétations paléoclimatologiques dérivées de ceux-ci.

## ANNEXES

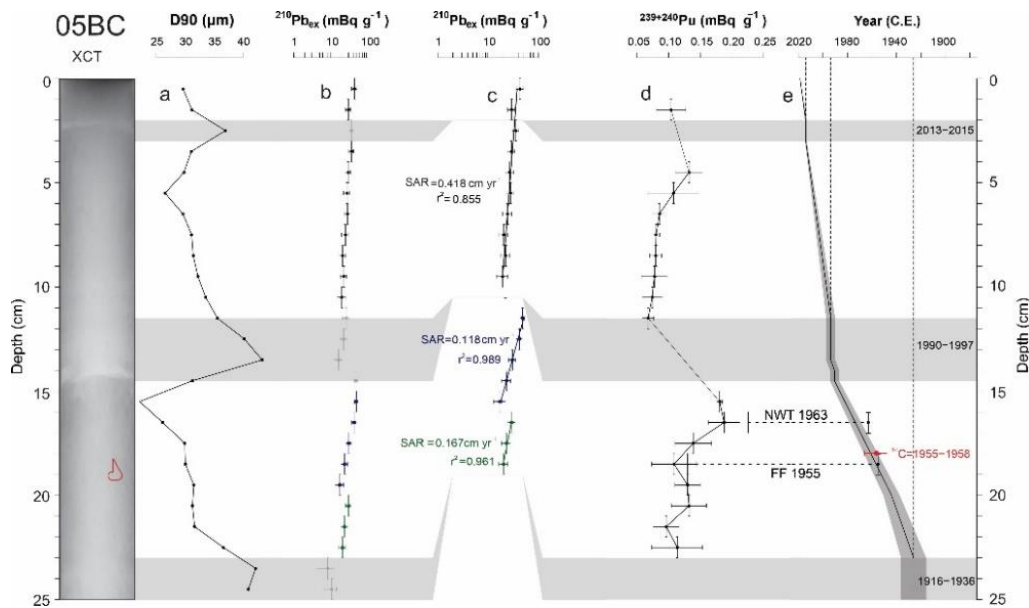


Fig. S1. a) D90, b)  $^{210}\text{Pb}$  excess profiles for core 05BC. c) Application of a CFCS model to the event-free sedimentary profile of  $^{210}\text{Pb}$  excess (without the thick graded beds, which are considered instantaneous deposits). d)  $^{239+240}\text{Pu}$  profile (FF 1955: the radionuclide was introduced with atmospheric nuclear testing; NWT 1963: the abundance peaked at the height of testing in 1963). e) Resulting age–depth model with  $1\sigma$  uncertainties.

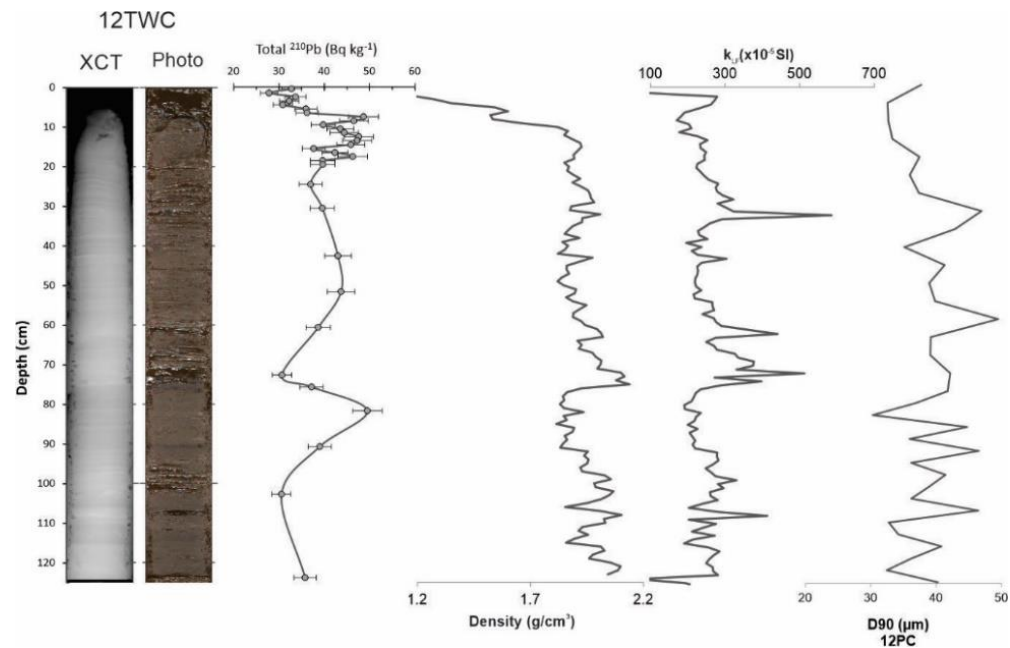


Fig. S2. Total  $^{210}\text{Pb}$ , density,  $k_{\text{LF}}$ , and  $D90$  profiles for the first 130 centimeters of core 12TWC. The  $^{210}\text{Pb}$  excess profile shows “event horizons” with irregular  $^{210}\text{Pb}$  and mineral compositions that are typical of periodic inputs of highly mobile sediment (e.g., Xu et al., 2015; Arias-Ortiz et al., 2018).

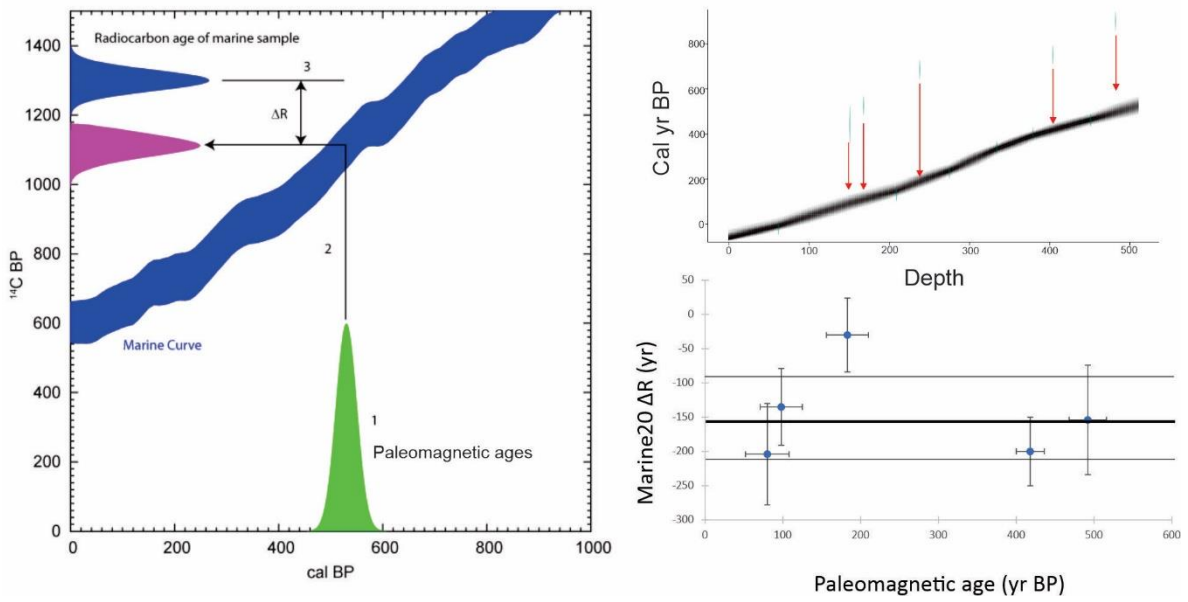


Fig. S3. A) Illustration of  $\Delta R$  and uncertainty calculation for samples with independently measured calendar ages (e.g., paleomagnetic ages). B)  $\Delta R$  over time obtained from paired  $^{14}\text{C}$  and paleomagnetic ages of core 12PC using Marine20 marine radiocarbon age calibration curves on deltar (<http://calib.org/deltar/>). Horizontal errors represent the uncertainty of paleomagnetic ages, in  $2\sigma$ ; vertical errors ( $\Delta R$ ) are  $1\sigma$ . Solid and dashed horizontal lines denote the median of  $\Delta R$  from all samples, plus or minus one standard deviation.

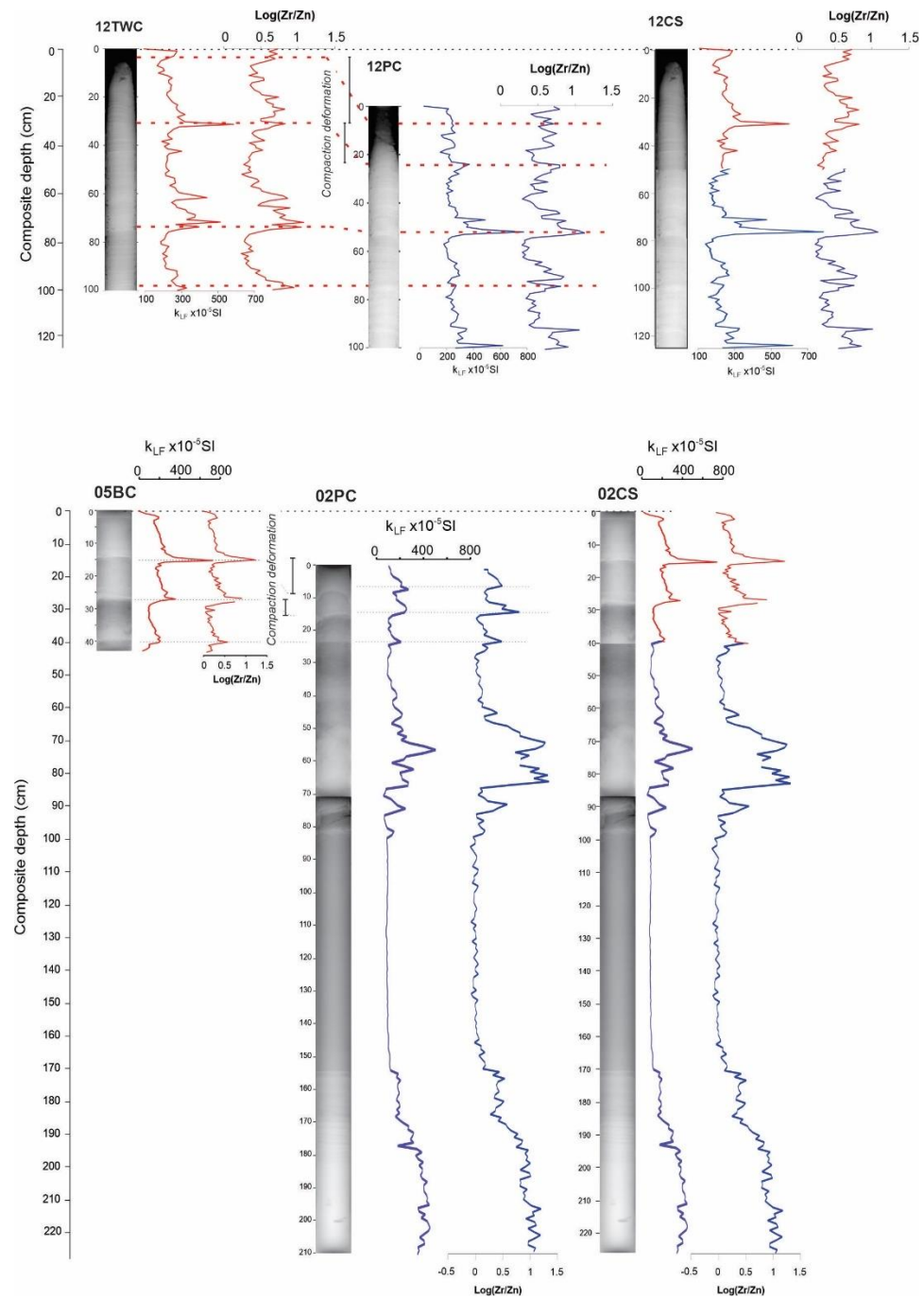


Fig. S4. Core top correlations of core 12TWC with 12PC and cores 05BC and 02PC with the help of physical and chemical parameters to obtain composite depths of the 12CS and 02CS cores.

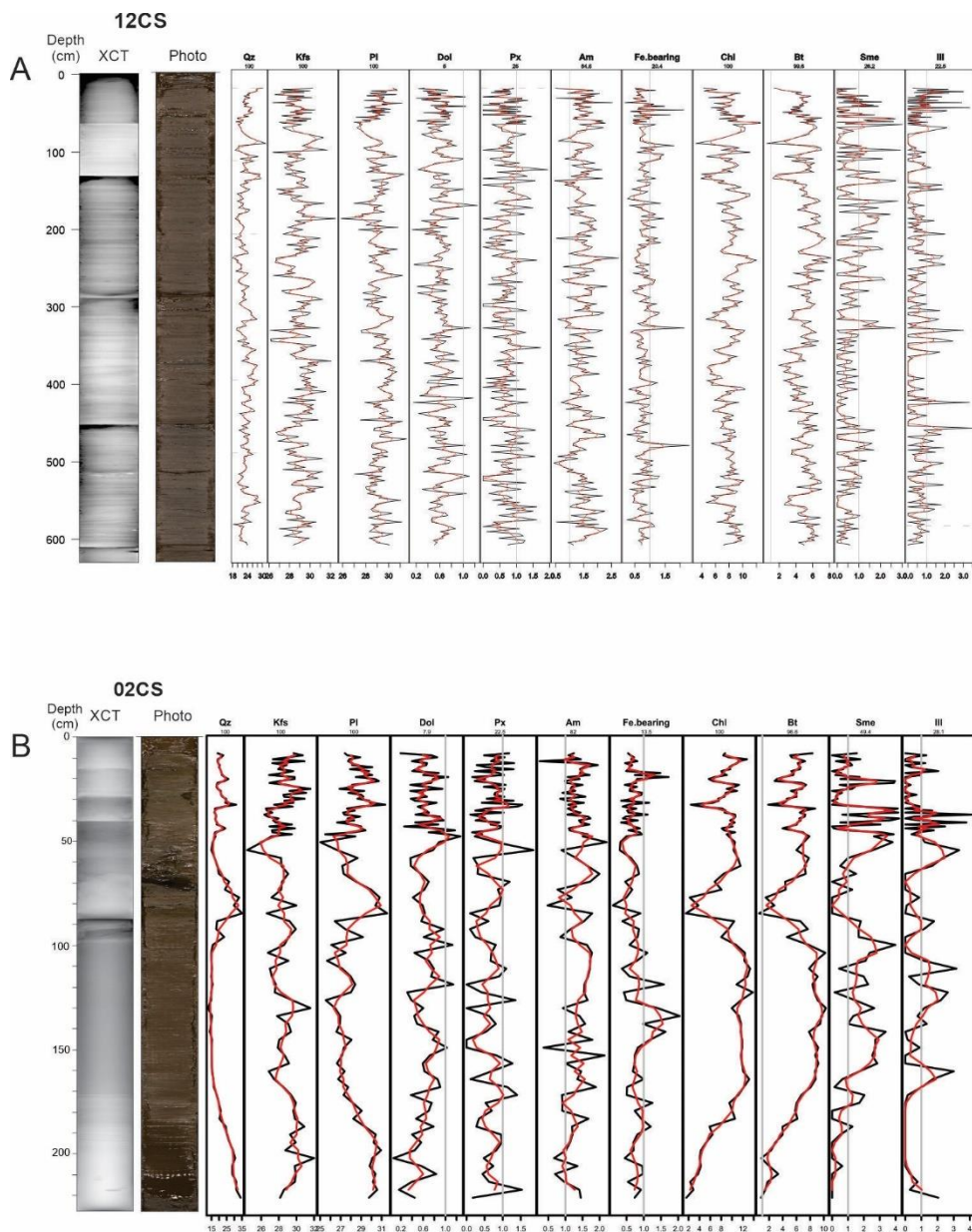


Fig. S5. Downcore mineralogical variations in cores 12CS (A) and 02CS (B). The vertical gray lines delineate the median values, and the red lines are 5-point moving averages.

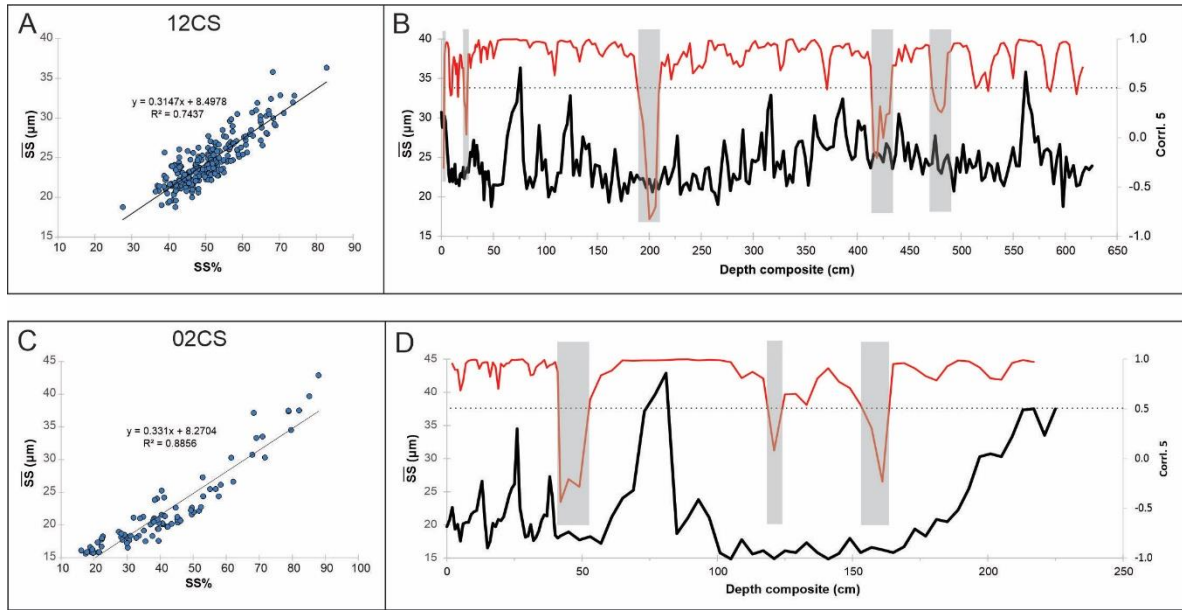


Fig. S6. (A, C) SS vs SS% for core 12CS and 02CS (B, D) sortable silt mean size and the running 5-point correlation profiles for core 12CS and 02CS. The gray areas indicate sections of the sortable silt record that do not pass the reliability test of a down core correlation coefficient  $>0.5$  between SS and SS% (McCave and Andrews, 2019a).

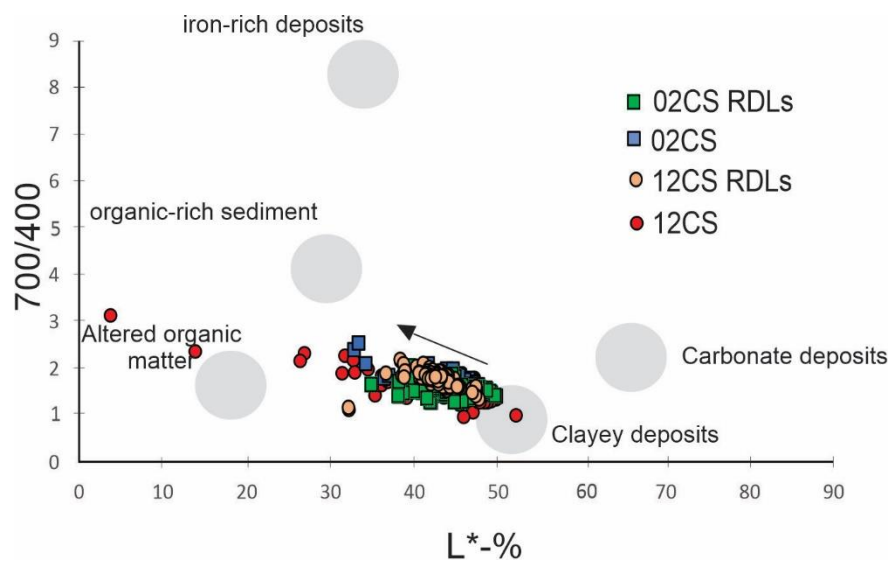


Fig. S7. Q7/4 diagram for the 12CS and 02CS cores. Five areas are distinguished (Debret et al., 2011): clayey deposits, organic-rich deposits (chlorophyll a and by-products), altered organic matter deposits, iron-rich deposits, and carbonate deposits.

## RÉFÉRENCES BIBLIOGRAPHIQUES

- Abdalati, W., Krabill, W., Frederick, E., Manizade, S., Martin, C., Sonntag, J., Swift, R., Thomas, R., Yungel, R., and Koerner, R. (2004). Elevation changes of ice caps in the Canadian Arctic Archipelago. *Journal of Geophysical Research: Earth Surface*, 109(F4).
- Adgebie A.T., Schneider R.R., Röhl U., Wefer, G. (2003) Glacial millennial-scale fluctuations in central African precipitation recorded in terrigenous sediment supply and freshwater signals offshore Cameroon. *Palaeogeogr Palaeoclimatol Palaeoecol* 197, 323–333. [https://doi:10.1016/S0031-0182\(03\)00474-7](https://doi:10.1016/S0031-0182(03)00474-7).
- Aitchison, J. (1982). The statistical analysis of compositional data. *Journal of the Royal Statistical Society: Series B (Methodological)*, 44(2), 139-160.
- Aitchison, J. (1990). Relative variation diagrams for describing patterns of compositional variability. *Mathematical Geology*, 22(4), 487–511.
- Aksu, A. E. (1983). Holocene and Pleistocene dissolution cycles in deep-sea cores of Baffin Bay and Davis Strait: Palaeoceanographic implications. *Marine Geology* 53: 331-348.
- Andrews, J. T. (2000). Icebergs and iceberg rafted detritus (IRD) in the North Atlantic: facts and assumptions. *Oceanography*, 100-108.
- Andrews, J. T. (2019). Baffin Bay/Nares Strait surface (seafloor) sediment mineralogy: further investigations and methods to elucidate spatial variations in provenance. *Canadian Journal of Earth Sciences*, 56(8), 814-828.
- Andrews, J. T., Klein, A. J., Jenner, K. A., Jennings, A. E., and Campbell, C. (2018). The variability of Baffin Bay seafloor sediment mineralogy: the identification of discrete glacial sediment sources and application to Late Quaternary downcore analysis. *Canadian Journal of Earth Sciences*, 55(6), 620-639.
- Appleby, P. G., and Oldfieldz, F. (1983). The assessment of  $^{210}\text{Pb}$  data from sites with varying sediment accumulation rates. *Hydrobiologia*, 103(1), 29-35.
- Arias-Ortiz, A., Masqué, P., Garcia-Orellana, J., Serrano, O., Mazarrasa, I., Marbà, N., Lovelock, C.E., Lavery, P. S., and Duarte, C. M. (2018). Reviews and syntheses:  $^{210}\text{Pb}$ -derived sediment and carbon accumulation rates in vegetated coastal ecosystems—setting the record straight. *Biogeosciences*, 15(22), 6791-6818.
- Azetsu-Scott, K., A. Clarke, K. Falkner, J. Hamilton, E.P. Jones, C. Lee, B. Petrie, S. Prinsenberg, M. Starr, and P. Yeats. (2010). Calcium carbonate saturation states in the

- waters of the Canadian Arctic Archipelago and the Labrador Sea. *Journal of Geophysical Research: Oceans* 115, 1-18.
- Barletta, F., St-Onge, G., Stoner, J. S., Lajeunesse, P., and Locat, J. (2010). A high-resolution Holocene paleomagnetic secular variation and relative paleointensity stack from eastern Canada. *Earth and Planetary Science Letters*, 298(1-2), 162-174.
- Beaudoin, A., Pienitz, R., Francus, P., Zdanowicz, C., and St-Onge, G. (2016). Palaeoenvironmental history of the last six centuries in the Nettilling Lake area (Baffin Island, Canada): A multi-proxy analysis. *The Holocene*, 26(11), 1835-1846.
- Ben Meftah, M., De Serio, F., De Padova, D., and Mossa, M. (2020). Hydrodynamic structure with scour hole downstream of bed sills. *Water*, 12(1), 186.
- Bouma, A.H., 1962. Sedimentology of Some Flysch Deposits. A Graphic Approach to Facies Interpretation. Elsevier, Amsterdam.
- Blaauw, M., and Christen, J. A. (2011). Flexible paleoclimate age-depth models using an autoregressive gamma process. *Bayesian Analysis* 6, 457-474.
- Blott, S. J., and Pye, K. (2001). GRADISTAT: a grain size distribution and statistics package for the analysis of unconsolidated sediments. *Earth Surface Processes and Landforms* 26, 1237-1248.
- Briner, J. P., Davis, P. T., and Miller, G. H. (2009). Latest Pleistocene and Holocene glaciation of Baffin Island, Arctic Canada: key patterns and chronologies. *Quaternary Science Reviews*, 28, 2075-2087.
- Briner, J. P., Michelutti, N., Francis, D. R., Miller, G. H., Axford, Y., Wooller, M. J., and Wolfe, A. P. (2006). A multi-proxy lacustrine record of Holocene climate change on northeastern Baffin Island, Arctic Canada. *Quaternary Research*, 65(3), 431-442.
- Bruel, R. and Sabatier, P. (2020). serac: a R package for ShortlivEd RAdionuclide Chronology of recent sediment cores. *Journal of Environmental Radioactivity* 225, 106449. <https://doi.org/10.1016/j.jenvrad.2020.106449>
- Caron, M., St-Onge, G., Montero-Serrano, J. C., Rochon, A., Georgiadis, E., Giraudeau, J., and Massé, G. (2019). Holocene chronostratigraphy of northeastern Baffin Bay based on radiocarbon and palaeomagnetic data. *Boreas*, 48(1), 147-165.
- Casse, M., Montero-Serrano, J.-C., and St-Onge, G. (2017). Influence of the Laurentide Ice Sheet and relative sea-level changes on sediment dynamics in the Estuary and Gulf of St. Lawrence since the last deglaciation. *Boreas*, 46, 541-561.
- Ciraci, E., Velicogna, I., and Swenson, S. (2020). Continuity of the mass loss of the world's glaciers and ice caps from the GRACE and GRACE Follow-On missions. *Geophysical Research Letters* 47(9), e2019GL086926.

- Coulthard, R. D., Furze, M. F., Pieńkowski, A. J., Nixon, F. C., & England, J. H. (2010). New marine  $\Delta R$  values for Arctic Canada. *Quaternary Geochronology*, 5(4), 419-434.
- Clark, P. U., Dyke, A. S., Shakun, J. D., Carlson, A. E., Clark, J., Wohlfarth, B., Mitrovica, J.X., Hostetler, S.W., and McCabe, A. M. (2009). The last glacial maximum. *science*, 325(5941), 710-714.
- Clarke, D. B., and Upton, B. G. J. (1971). Tertiary basalts of Baffin Island: field relations and tectonic setting. *Canadian Journal of Earth Sciences*, 8(2), 248-258.
- Cohen, J., Screen, J. A., Furtado, J. C., Barlow, M., Whittleston, D., Coumou, D., Francis, J., Dethloff, K., Entekhabi, D., Overland, J., and Jones, J. (2014). Recent Arctic amplification and extreme mid-latitude weather. *Nature geoscience*, 7(9), 627-637.
- Constable, C., Korte, M., and Panovska, S. (2016). Persistent high paleosecular variation activity in southern hemisphere for at least 10 000 years. *Earth and Planetary Science Letters*, 453, 78-86.
- Cook, A. J., Copland, L., Noël, B. P. Y., Stokes, C. R., Bentley, M. J., Sharp, M. J., Bingham, R. G. and van den Broeke, M. R. (2019). Atmospheric forcing of rapid marine-terminating glacier retreat in the Canadian Arctic Archipelago. *Science Advances* 5, eaau8507, <https://doi.org/10.1126/sciadv.aau8507>.
- Corminboeuf, A., Montero-Serrano, J.-C., and St-Louis, R. (2021a). Spatial and temporal distributions of polycyclic aromatic hydrocarbons in sediments from the Canadian Arctic Archipelago. *Marine Pollution Bulletin* 171, 112729. <https://doi.org/10.1016/j.marpolbul.2021.112729>.
- Corminboeuf, A., Montero-Serrano, J.-C., St-Louis, R., Dalpé, A., and Gélinas, Y. (2021b). Pre- and post-industrial levels of polycyclic aromatic hydrocarbons in sediments from the Estuary and Gulf of St. Lawrence (eastern Canada). *Marine Pollution Bulletin*, 113219. <https://doi.org/10.1016/j.marpolbul.2021.113219>.
- Cowan, E. A., and Powell, R. D., (1991). Ice-proximal sediment accumulation rates in a temperate glacial fjord, southeastern Alaska, in Anderson, J. B., and Ashley, G. M., eds. *Glacial marine sedimentation; Paleoclimatic significance*: Boulder, Colorado, Geological Society of America Special Paper 261.
- Crespin, E., H. Goosse, T. Fichefet, and M. E. Mann. (2009). The 15th century Arctic warming in coupled model simulations with data assimilation. *Climate of the Past* 5, 389-401.
- Croudace, I. W., and Rothwell, R. G. (Eds.). (2015). *Micro-XRF Studies of Sediment Cores: Applications of a non-destructive tool for the environmental sciences* (Vol. 17). Springer.

- de Vernal, A., G. Bilodeau, C. Hillaire-Marcel, and N. Kassou. (1992). Quantitative assessment of carbonate dissolution in marine sediments from foraminifer linings vs. shell ratios: Davis Strait, northwest North Atlantic. *Geology* 20, 527-530.
- Debret, M., Sebag, D., Desmet, M., Balsam, W., Copard, Y., Mourier, B., Susperregui, A.-S., Arnaud, F., Bentaleb, I., Chapron, E., Lallier-Vergès, E., and Winiarski, T. (2011). Spectrocolorimetric interpretation of sedimentary dynamics: The new “Q7/4 diagram”. *Earth-Science Reviews*, 109(1-2), 1-19. <https://doi:10.1016/j.earscirev.2011.07.002>.
- Deschamps, C.-E., Montero-Serrano, J.-C., and St-Onge, G. (2018). Sediment Provenance Changes in the Western Arctic Ocean in Response to Ice Rafting, Sea Level, and Oceanic Circulation Variations Since the Last Deglaciation. *Geochemistry, Geophysics, Geosystems*, 19, 2147-2165.
- Dowdeswell, J. A., Hogan, K. A., Arnold, N. S., Mugford, R. I., Wells, M., Hirst, J. P. P., and Decalf, C. (2015). Sediment-rich meltwater plumes and ice-proximal fans at the margins of modern and ancient tidewater glaciers: Observations and modelling. *Sedimentology*, 62, 1665-1692.
- Duboc, Q., St-Onge, G., and Lajeunesse, P. (2017). Sediment records of the influence of river damming on the dynamics of the Nelson and Churchill Rivers, western Hudson Bay, Canada, during the last centuries. *The Holocene*, 27(5), 712-725.
- Dyke, A. S., Andrews, J. T., and Miller, G. H. (1982). Quaternary geology of Cumberland Peninsula, Baffin Island, District of Franklin, Commission géologique du Canada, Mémoires no. 403.
- Eberl, D. D. (2003). User guide to RockJock—A program for determining quantitative mineralogy from X-ray diffraction data. USGS Open File Report 40, 03-78.
- Emmer, A. (2017). Glacier retreat and glacial lake outburst floods (GLOFs). In Oxford Research Encyclopedia of Natural Hazard Science.
- Fisher, D. A., Koerner, R. M., Bourgeois, J. C., Zielinski, G., Wake, C., Hammer, C. U., Clausen, H. B., Gundestrup, N., Johnsen, S., Goto-Azuma, K., Hondoh, T., Blake, E., and Gerasimoff, M. (1998). Penny ice cap cores, Baffin Island, Canada, and the Wisconsinan Foxe Dome connection: two states of Hudson Bay ice cover. *Science*, 279(5351), 692-695.
- Gamboa, A., Montero-Serrano, J.-C., St-Onge, G., Rochon, A., and Desiage, P.-A. (2017). Mineralogical, geochemical, and magnetic signatures of surface sediments from the Canadian Beaufort Shelf and Amundsen Gulf (Canadian Arctic). *Geochemistry, Geophysics, Geosystems*, 18, 488-512.

- Gardner, A. S., Moholdt, G., Wouters, B., Wolken, G.J., Burgess, D.O., Sharp, M.J., Cogley, J.G., Braun, C., and Labine, C. (2011). Sharply increased mass loss from glaciers and ice caps in the Canadian Arctic Archipelago, *Nature*, 473, 357–360.
- Gardner, A., Moholdt, G., Arendt, A., and Wouters, B. (2012). Accelerated contributions of Canada’s Baffin and Bylot Island glaciers to sea level rise over the past half century. *Cryosphere*, 6, 1103–1125.
- Gilbert, R. (1982b). Contemporary Sedimentary Environments on Baffin Island, N.W.T., Canada: Glaciomarine Processes in Fiords of Eastern Cumberland Peninsula. *Arctic and Alpine Research*, 14, 1-12.
- Gilbert, R. (1983). Sedimentary processes of Canadian Arctic fjords. *Sedimentary geology*, 36(2-4), 147-175.
- Gilbert, R. (1985). Quaternary glaciomarine sedimentation interpreted from seismic surveys of fiords on Baffin Island, NWT. *Arctic*, 38(4), 271-280.
- Gilbert, R. (1982a). The Broughton Trough on the continental shelf of eastern Baffin Island, Northwest Territories. *Canadian Journal of Earth Sciences* 19, 1599-1607.
- Gilbert, R., Naldrett, D. L., and Horvath, V. V. (1989). Holocene sedimentary environment of Cambridge fiord, Baffin Island, northwest Territories. *Canadian Journal of Earth Sciences*, 27(2), 271-280.
- Greve, R. (2000). On the response of the Greenland ice sheet to greenhouse climate change. *Climatic Change*, 46(3), 289-303.
- Grobe, H. (1987). A simple method for the determination of ice rafted debris in sediment cores. *Polarforschung*, 57(3), 123-126.
- Harig, C., and Simons, F. J. (2016). Ice mass loss in Greenland, the Gulf of Alaska, and the Canadian Archipelago: Seasonal cycles and decadal trends. *Geophysical Research Letters*, 43(7), 3150-3159.
- Heaton, T. J., Köhler, P., Butzin, M., Bard, E., Reimer, R. W., Austin, W. E., Ramsey, C. R., Grootes, P., Huhgen, K.A., Kromer, B., Reimer, P., Adkins, J., Burke, A., Cook, M. S., Olsen, J., and Skinner, L. C. (2020). Marine20—the marine radiocarbon age calibration curve (0–55,000 cal BP). *Radiocarbon*, 62(4), 779-820.
- Heid, T., and Kääb, A. (2012). Repeat optical satellite images reveal widespread and long term decrease in land-terminating glacier speeds. *The Cryosphere*, 6(2), 467-478.
- Holland, D. M., Thomas, R. H., de Young, B., Ribergaard, M. H., and Lyberth, B. (2008). Acceleration of Jakobshavn Isbræ triggered by warm subsurface ocean waters. *Nature Geoscience*, 1, 659-664.

- Howe, J. A., Austin, W. E., Forwick, M., Paetzel, M., Harland, R., and Cage, A. G. (2010). Fjord systems and archives: a review. Geological Society, London, Special Publications, 344, 5-15.
- Hughes, P. D., and Woodward, J. C. (2008). Timing of glaciation in the Mediterranean mountains during the last cold stage. Journal of Quaternary Science: Published for the Quaternary Research Association, 23(6-7), 575-588.
- Huybrechts, P., Letreguilly, A., and Reeh, N. (1991). The Greenland ice sheet and greenhouse warming. Palaeogeography, Palaeoclimatology, Palaeoecology, 89(4), 399-412.
- IPCC. (2014) Climate Change 2014: Synthesis Report. Contribution of Working Groups I, II and III to the Fifth Assessment Report of the Intergovernmental Panel on Climate Change [Core Writing Team, R.K. Pachauri and L.A. Meyer (eds.)]. IPCC, Geneva, Switzerland, 151 pp.
- IPCC. (2019). Special Report on the Ocean and Cryosphere in a Changing Climate (SROCC). 1170
- Jackson A., Jonkers A. R. T. and Walker M. R. (2000). Four centuries of geomagnetic secular variation from historical records. Philosophical Transaction of Royal Society of London, 358, 957–990.
- Jackson, G. D., and Berman, R. G. (2000). Precambrian metamorphic and tectonic evolution of northern Baffin Island, Nunavut, Canada. The Canadian Mineralogist, 38(2), 399-421.
- Jenner, K. A., Campbell, D. C., and Piper., D. J. W. (2018). Along-slope variations in sediment lithofacies and depositional processes since the Last Glacial Maximum on the northeast Baffin margin, Canada. Marine Geology 405, 92-107.
- Joughin, I., Smith, B. E., Howat, I. M., Scambos, T., and Moon, T. (2010). Greenland flow variability from ice-sheet-wide velocity mapping. Journal of Glaciology, 56(197), 415-430.
- Jones, P. D., and Mann, M. E. (2004). Climate over past millennia. Reviews of Geophysics, 42(2).
- Kaser, G., Cogley, J. G., Dyurgerov, M. B., Meier, M. F., & Ohmura, A. (2006). Mass balance of glaciers and ice caps: Consensus estimates for 1961–2004. Geophysical Research Letters, 33(19).
- Kassambara, A., Mundt, F. (2020). Factoextra: Extract and Visualize the Results of Multivariate Data Analyses. R Package Version 1.0.7. [Available at <https://cran.r-project.org/web/packages/factoextra/>].

- Kaufman, D. S., Schneider, D. P., McKay, N. P., Ammann, C. M., Bradley, R. S., Briffa, K. R., Miller, G. H., Otto-Bliesner, B. L., Overpeck, J. T., Vinther, B. M., and Arctic Lakes 2k Project Members. (2009). Recent warming reverses long-term Arctic cooling. *Science*, 325(5945), 1236-1239.
- Ketterer, M. E., Watson, B. R., Matisoff, G., and Wilson, C. G. (2002). Rapid dating of recent aquatic sediments using Pu activities and 240Pu/239Pu as determined by quadrupole inductively coupled plasma mass spectrometry. *Environmental science & technology*, 36(6), 1307-1311.
- Ketterer, M.E., Hafer, K.M., Jones, V.J., and Appleby, P.G. (2004). Rapid dating of recent sediments in Loch Ness: inductively coupled plasma mass spectrometric measurements of global fallout Plutonium. *The Science of the Total Environment* 322, 221-229. <https://doi.org/10.1016/j.scitotenv.2003.09.016>
- Kinnard, C., Zdanowicz, C. M., Fisher, D. A., Isaksson, E., de Vernal, A., and Thompson, L. G. (2011). Reconstructed changes in Arctic sea ice over the past 1,450 years. *Nature* 479, 509-512.
- Kirschvink, J. L. (1980). The least-squares line and plane and the analysis of palaeomagnetic data. *Geophysical Journal International*, 62, 699-718.
- Korte, M., and Constable, C. (2011). Improving geomagnetic field reconstructions for 0–3 ka. *Physics of the Earth and Planetary Interiors*, 188(3-4), 247-259.
- Lacourse, T., and Gajewski, K. (2020). Current practices in building and reporting age-depth models. *Quaternary Research* 96, 28–38. <https://doi.org/10.1017/qua.2020.47>
- Lapointe, F., Bradley, R. S., Francus, P., Balascio, N. L., Abbott, M. B., Stoner, J. S., St-Onge, G., De Coninck, A., and Labarre, T. (2020). Annually resolved Atlantic sea surface temperature variability over the past 2,900 y. *Proceedings of the National Academy of Sciences*, 117(44), 27171-27178.
- Lenaerts, J. T., van Angelen, J. H., van den Broeke, M. R., Gardner, A. S., Wouters, B., and van Meijgaard, E. (2013). Irreversible mass loss of Canadian Arctic Archipelago glaciers. *Geophysical Research Letters*, 40, 870 –874.
- Lévesque, Y., St-Onge, G., Lajeunesse, P., Desiage, P.-A., and Brouard, É. (2020). Defining the maximum extent of the Laurentide Ice Sheet in Home Bay cross-shelf trough during the Last glacial episode. *Boreas* 49, 52-70.
- Liu, D., Bertrand, S., Vandekerkhove, E., and Renson, V. (2021). Provenance of Baker River sediments (Chile, 48° S): Implications for the identification of flood deposits in fjord sediments. *Earth Surface Processes and Landforms*, 1-13.
- Mazaud, A. (2005). User-friendly software for vector analysis of the magnetization of long sediment cores. *Geochemistry, Geophysics, Geosystems*, 6, Q12006,

McBean, G., Alekseev, G., Chen, D., Foerland, E., Fyfe, J., Groisman, P.Y., King, R., Melling, H., Vose, R., and Whitfield, P.H. (2005). Chapter 2. Arctic Climate: past and present, impact of a warming Arctic. Arctic Climate Impact Assessment (ACIA), Arctic Climate Impact Assessment (ACIA). Cambridge.

McCave, I. N., and Andrews, J. T. (2019a). Distinguishing current effects in sediments delivered to the ocean by ice. I. Principles, methods and examples. Quaternary Science Reviews, 212, 92-107.

McCave, I. N., and Andrews, J. T. (2019b). Distinguishing current effects in sediments delivered to the ocean by ice. II. Glacial to Holocene changes in high latitude North Atlantic upper ocean flows. Quaternary Science Reviews, 223, 105902.

McKenna Neuman, C., Gilbert, R., and Nickling, W. G. (1986). Aeolian processes and landforms in glaciofluvial environments of southeastern Baffin Island, NWT, Canada.

Miller, G. H. (1973). Late Quaternary Glacial and Climatic History of Northern Cumberland Peninsula, Baffin Island, NWT, Canada1. Quaternary Research, 3(4), 561-583.

Miller, G. H., Brigham-Grette, J., Alley, R. B., Anderson, L., Bauch, H. A., Douglas, M. S. V., and Funder, S. V. (2010). Temperature and precipitation history of the Arctic. Quaternary Science Reviews, 29, 1679-1715.

Miller, G. H., Geirsdóttir, Á., Zhong, Y., Larsen, D. J., Otto-Bliesner, B. L., Holland, M. M., Bailey, D. A., Refsnider, K. A., Lehman, S. J., Southon, J. R., Anderson, C., Björnsson, H., and Thordarson, T. (2012). Abrupt onset of the Little Ice Age triggered by volcanism and sustained by sea-ice/ocean feedbacks. Geophysical Research Letters, 39(2).

Moffa-Sánchez, P., Hall, I.R. (2017). North Atlantic variability and its links to European climate over the last 3000 years. Nature Communications 8, 1726. <https://doi.org/10.1038/s41467-017-01884-8>

Montero-Serrano, J.-C., Föllmi, K. B., Adatte, T., Spangenberg, J. E., Tribouillard, N., Fantasia, A. and Suan, G. (2015). Continental weathering and redox conditions during the early Toarcian Oceanic Anoxic Event in the northwestern Tethys: Insight from the Posidonia Shale section in the Swiss Jura Mountains. Palaeogeography, Palaeoclimatology, Palaeoecology, 429, 83-99.

Montero-Serrano, J.-C., Palarea-Albaladejo, J., Martin-Fernandez, J.-A., Martinez-Santana, M., Gutierrez-Martin, J. V. (2010). Sedimentary chemofacies characterization by

- means of multivariate analysis. *Sedimentary Geology*, 228, 218–228, <https://doi:10.1016/j.sedgeo.2010.04.013>.
- Montero-Serrano, J-C, Brossard, J., Corminboeuf, A. (2018). Collecting sedimentary sequences for paleoclimate, paleoceanographic and environmental studies in the eastern Canadian Arctic Archipelago and Baffin Bay. ArcticNet Leg 3 Cruise Report - CCGS Amundsen expedition (16 August to 9 September). ArcticNet 14 p.
- Montero-Serrano, J-C., Bout-Roumazeilles, V., Tribouillard, N., Sionneau, T., Ribouleau, A., Bory, A., and Flower, B. (2009). Sedimentary evidence of deglacial megafloods in the northern Gulf of Mexico (Pigmy Basin). *Quaternary Science Reviews*, 28, 3333-3347.
- Montero-Serrano, J-C., Palarea-Albaladejo, J., Martín-Fernández, J. A., Martínez-Santana, M., and Gutiérrez-Martín, J. V. (2010). Sedimentary chemofacies characterization by means of multivariate analysis. *Sedimentary Geology* 228, 218-228.
- Moore, J. J., Hughen, K. A., Miller, G. H., and Overpeck, J. T. (2001). Little Ice Age recorded in summer temperature reconstruction from varved sediments of Donard Lake, Baffin Island, Canada. *Journal of Paleolimnology*, 25(4), 503-517.
- Mulder, T., Syvitski, J. P., Migeon, S., Faugères, J. C., and Savoye, B. (2003). Marine hyperpycnal flows: initiation, behavior and related deposits. A review. *Marine and Petroleum Geology*, 20(6-8), 861-882.
- Mulder, T., and Syvitski, J. P. M. (1995). Turbidity currents generated at river mouths during exceptional discharges to the world oceans. *Journal of Geology*, 103, 285–299.
- Münchow, A., Falkner, K. K., and Melling, H. (2015). Baffin Island and west Greenland current systems in northern Baffin Bay. *Progress in Oceanography*, 132, 305-317.
- Narancic, B., Saulnier-Talbot, É., Meyer, H. and Pienitz, R. (2021), A 5000-year paleoclimate record from Nettilling Lake (Baffin Island) based on diatom assemblages and oxygen isotope composition. *Journal of Quaternary Science*. <https://doi.org/10.1002/jqs.3366>
- Noël, B., van de Berg, W. J., Lhermitte, S., Wouters, B., Schaffer, N., & van den Broeke, M. R. (2018). Six Decades of Glacial Mass Loss in the Canadian Arctic Archipelago. *Journal of Geophysical Research: Earth Surface*, 123, 1430-1449.
- Normandeau, A., MacKillop, K., Macquarrie, M., Richards, C., Bourgault, D., Campbell, D. C., Maselli, V., Philibert, G., and Clarke, J. H. (2021). Submarine landslides triggered by iceberg collision with the seafloor. *Nature Geoscience*, 14(8), 599-605.
- Normandeau, A., Broom, L.M., Carson, T., and Trottier, A.-P., 2019. CCGS Amundsen 2019804 expedition: marine geohazards and sediment transport processes in Baffin

Bay, Nunavut; Geological Survey of Canada, Open File 8649, 25 p.  
<https://doi.org/10.4095/321054>

Normandeau, A., Dietrich, P., Hughes Clarke, J., Van Wychen, W., Lajeunesse, P., Burgess, D., and Ghienne, J. F. (2019). Retreat pattern of glaciers controls the occurrence of turbidity currents on high-latitude fjord deltas (eastern Baffin Island). *Journal of Geophysical Research: Earth Surface*, 124(6), 1559-1571.

Ó Cofaigh, C., Dowdeswell, J. A., Jennings, A. E., Hogan, K. A., Kilfeather, A., Hiemstra, J. F., Noormets, R., Evans, J., McCarthy, D. J., Andrews, J. T., Lloyd, J. M., and Moros, M. (2013). An extensive and dynamic ice sheet on the West Greenland shelf during the last glacial cycle. *Geology*, 41(2), 219-222.

Oerlemans, J. (2005). Extracting a climate signal from 169 glacier records. *Science*, 308, 675–677.

Overland, J. E., Hanna, E., Hanssen-Bauer I, Kim SJ, Walsh J, Wang M, Bhatt US, Thoman RL (2016) Surface air temperature [in Artic Report Card 2016], <http://www.arctic.noaa.gov/Report-Card>.

Palarea-Albaladejo J., and Martin-Fernandez J.A. (2015). zCompositions — R package for multivariate imputation of left-censored data under a compositional approach. *Chemometrics and Intelligence Laboratory Systems* 143, 85-96.

Philippe, Édouard (2019). Acquisition de l'aimantation remanente dans les sédiments. Thèse. Rimouski, Québec, Université du Québec à Rimouski, Institut des sciences de la mer de Rimouski (ISMER), 171 p

Philippe, É. G.H., Valet, J.-P., Lopes, F., St-Onge, G. (2018). Are paleomagnetic records from U-channels appropriate for studies of reversals and excursions? *Geochemistry, Geophysics, Geosystems* 19, 4130-4142.

Pendleton, S. L., Miller, G. H., Anderson, R. A., Crump, S. E., Zhong, Y., Jahn, A., and Geirsdottir, Á. (2017). Episodic Neoglacial expansion and rapid 20th century retreat of a small ice cap on Baffin Island, Arctic Canada, and modeled temperature change. *Climate of the Past*, 13, 1527-1537.

Pope, E. L., Normandeau, A., Cofaigh, C. Ó., Stokes, C. R., and Talling, P. J. (2019). Controls on the formation of turbidity current channels associated with marine-terminating glaciers and ice sheets. *Marine Geology*, 415, 105951.

Powell, R. D. (1981). A model for sedimentation by tidewater glaciers: *Annals of Glaciology*, v. 2, p. 129-134.

Powell, R. D. (1985). Iceberg calving and its influence on ice-proximal, subaqueous glacigenic lithofacies, in Abstracts of the 14th Arctic Workshop on Arctic Land- Sea Interaction: Canada, Bedford Institute of Oceanography, p. 101-103.

R Core Team. (2021). R: A language and environment for statistical computing. R Foundation for Statistical Computing, Vienna, Austria. [Available at <https://www.R-project.org/>]

Radić, V., and Hock, R. (2010). Regional and global volumes of glaciers derived from statistical upscaling of glacier inventory data. *Journal of Geophysical Research: Earth Surface*, 115, F01010.

Reimer, R. W., and Reimer, P. J. (2017). An online application for  $\Delta R$  calculation. *Radiocarbon*, 59(5), 1623-1627.

Reimnitz, E., Kempema, E. W. and Barnes, P. W. (1987). Anchor ice, seabed freezing, and sediment dynamics in shallow Arctic seas. *Journal of Geophysical Research-Oceans* 92, 14671–14678.

Reyss, J.-L., Schmidt, S., Legeleux, F., and Bonté, P. (1995). Large, low background well-type detectors for measurements of environmental radioactivity. *Nuclear Instruments and Methods in Physics Research Section A: Accelerators, Spectrometers, Detectors and Associated Equipment* 357, 391–397. [https://doi.org/10.1016/0168-9002\(95\)00021-6](https://doi.org/10.1016/0168-9002(95)00021-6).

Rignot, E., Box, J. E., Burgess, E., and Hanna, E. (2008). Mass balance of the Greenland ice sheet from 1958 to 2007. *Geophysical Research Letters*, 35(20).

Russell, N., Cook, G.T., Ascough, P.L., Scott, E.M., and Dugmore, A.J. (2011). Examining the inherent variability in  $\Delta R$ : new methods of presenting  $\Delta R$  values and implications for MRE studies. *Radiocarbon* 53, 277–288. <https://doi.org/10.1017/S003382220005654X>.

Sanchez-Cabeza, J. A., and Ruiz-Fernández, A. C. (2012).  $^{210}\text{Pb}$  sediment radiochronology: an integrated formulation and classification of dating models. *Geochimica et Cosmochimica Acta*, 82, 183-200.

Sarnthein, M., Balmer, S., Grootes, P. M., and Mudelsee, M. (2015). Planktic and benthic  $^{14}\text{C}$  reservoir ages for three ocean basins, calibrated by a suite of  $^{14}\text{C}$  plateaus in the glacial-to-deglacial Suigetsu atmospheric  $^{14}\text{C}$  record. *Radiocarbon*, 57(1), 129-151.

Schaffer, N., Copland, L., and Zdanowicz, C. (2017). Ice velocity changes on Penny Ice Cap, Baffin Island, since the 1950s. *Journal of Glaciology*, 63: 716-730.

Schatz, E. R., Mángano, M. G., Aitken, A. E., and Buatois, L. A. (2013). Response of benthos to stress factors in Holocene Arctic fjord settings: Maktak, Coronation, and North Pangnirtung Fjords, Baffin Island, Canada. *Palaeogeography, Palaeoclimatology, Palaeoecology*, 386, 652-668.

Schmidt, M., Leipe, C., Becker, F., Goslar, T., Hoelzmann, P., Mingram, J., Müller, S., Tjallingii, R., Wagner, M., Tarasov, P.E. (2019). A multi-proxy palaeolimnological

record of the last 16,600 years from coastal Lake Kushu in northern Japan. *Palaeogeography, Palaeoclimatology, Palaeoecology* 514, 613–626. <https://doi.org/10.1016/j.palaeo.2018.11.010>

Serreze, M. C., and Francis, J. A. (2006). The Arctic Amplification Debate. *Climatic Change*, 76, 241-264.

Sharp, M., Burgess, D. O., Cawkwell, F., Copland, L., Davis, J. A., Dowdeswell, E. K., Dowdeswell, Gardner, A. S., Mair, D., Wang, L., Williamson, S. N., Wolken, G. J., & Wyatt, F. (2014). Remote sensing of recent glacier changes in the Canadian Arctic. In *Global land ice measurements from space*. Springer, Berlin, Heidelberg, pp. 205-228.

Shaw, J. (1987). Glacial sedimentary processes and environmental reconstruction based on lithofacies. *Sedimentology*, 34, 103-116.

Stevenard, N., Montero-Serrano, J.-C., Eynaud, F., St-Onge, G., Zaragosi, S. and Copland, L. (2022). Lateglacial and Holocene sedimentary dynamics in northwestern Baffin Bay as recorded in sediment cores from Cape Norton Shaw Inlet (Nunavut, Canada). *Boreas*. <https://doi.org/10.1111/bor.12575>.

Stoner, J. S., and St-Onge, G. (2007). Chapter Three Magnetic Stratigraphy in *Paleoceanography: Reversals, Excursions, Paleointensity, and Secular Variation*, p. 99-138. In C. Hillaire-Marcel and A. De Vernal [eds.], *Developments in Marine Geology*. Elsevier.

Stoner, J. S., Channell, J. E., Mazaud, A., Strano, S. E., and Xuan, C. (2013). The influence of high-latitude flux lobes on the Holocene paleomagnetic record of IODP Site U1305 and the northern North Atlantic. *Geochemistry, Geophysics, Geosystems*, 14(10), 4623-4646.

St-Onge, G., Mulder, T., Francus, P., and Long, B. (2007). Chapter Two Continuous Physical Properties of Cored Marine Sediments, p. 63-98. In C. Hillaire-Marcel and A. De Vernal [eds.], *Developments in Marine Geology*. Elsevier.

St-Onge, G., Mulder, T., Piper, D. J., Hillaire-Marcel, C., and Stoner, J. S. (2004). Earthquake and flood-induced turbidites in the Saguenay Fjord (Québec): a Holocene paleoseismicity record. *Quaternary Science Reviews*, 23(3-4), 283-294.

St-Onge, M. R., Van Gool, J. A., Garde, A. A., and Scott, D. J. (2009). Correlation of Archaean and Palaeoproterozoic units between northeastern Canada and western Greenland: constraining the pre-collisional upper plate accretionary history of the Trans-Hudson orogen. *Geological Society, London, Special Publications*, 318(1), 193-235.

- Syvitski, J. P. (1989). On the deposition of sediment within glacier-influenced fjords: oceanographic controls. *Marine Geology*, 85: 301-329.
- Syvitski, J. P., and Shaw, J. (1995). Sedimentology and geomorphology of fjords. In *Developments in sedimentology* (Vol. 53, pp. 113-178). Elsevier.
- Syvitski, J. P., and Shaw, J. (1995). Sedimentology and geomorphology of fjords. In *Developments in sedimentology* (Vol. 53, pp. 113-178). Elsevier.
- Syvitski, J.P. and Piper, D.J. (1990). Baffin Island Fiords; in Chapter 10 of *Geology of the Continental Margin of Eastern Canada*, M.J. Keen and G.L. Williams (ed.); Geological Survey of Canada, *Geology of Canada*, no. 2, p. 563-566.
- Tang, C. C. L., Ross, C. K., Yao, T., Petrie, B., DeTracey, B. M. and Dunlap, E. (2004). The circulation, water masses and sea-ice of Baffin Bay. *Progress in Oceanography*, 63, 183-228.
- Tanty, C., Valet, J. P., Carlut, J., Bassinot, F., and Zaragosi, S. (2016). Acquisition of detrital magnetization in four turbidites. *Geochemistry, Geophysics, Geosystems*, 17(8), 3207-3223.
- Telford, R. J., Heegaard, E. and Birks, H. J. B. (2004). All age-depth models are wrong: but how badly? *Quaternary science Reviews* 23, 1-5, <https://doi:10.1016/j.quascirev.2003.11.003>.
- Thomas, E. K., and Briner, J. P. (2009). Climate of the past millennium inferred from varved proglacial lake sediments on northeast Baffin Island, Arctic Canada. *Journal of Paleolimnology*, 41(1), 209-224.
- Thomas, E. K., Briner, J. P., Axford, Y., Francis, D. R., Miller, G. H., & Walker, I. R. (2011). A 2000-yr-long multi-proxy lacustrine record from eastern Baffin Island, Arctic Canada reveals first millennium AD cold period. *Quaternary Research*, 75(3), 491-500.
- Trachsel, M. and Telford, R. J. (2017). All age-depth models are wrong, but are getting better. *The Holocene* 27, 860-869, <https://doi:10.1177/0959683616675939>.
- Van den Boogaart, K. G., and Tolosana-Delgado, R. (2008). “Compositions”: a unified R package to analyze compositional data. *Computers & Geosciences*, 34(4), 320-338.
- van den Broeke, M., Bamber, J., Ettema, J., Rignot, E., Schrama, E., van de Berg, W. J., van Meijgaard, E., Velicogna, I., and Wouters, B. (2009). Partitioning recent Greenland mass loss. *science*, 326(5955), 984-986.
- Van Wychen, W., Copland, L., Burgess, D., Gray, L., and Schaffer, N., (2015). Glacier velocities and dynamic discharge from the Ice masses of Baffin Island and Bylot Island, Nunavut, Canada. *Canadian Journal of Earth Sciences*, 52, 980–989.

- Van Wychen, W., Copland, L., Gray, L., Burgess, D., Danielson, B., and Sharp, M. (2012). Spatial and temporal variation of ice motion and ice flux from Devon Ice Cap, Nunavut, Canada. *Journal of Glaciology*, 58(210), 657-664.
- Vandekerckhove, E., Bertrand, S., Torrejon, F., Kylander, M. E., Reid, B., and Saunders, K. M. (2021). Signature of modern glacial lake outburst floods in fjord sediments (Baker River, southern Chile). *Sedimentology*, 68(6), 2798-2819.
- von Eynatten, H., Barcelo-Vidal, C. and Pawlowsky-Glahn, V. (2003). Composition and Discrimination of sandstones: a statistical evaluation of different analytical methods. *Journal of Sedimentary Research* 73, 47–57.
- von Eynatten, H., Tolosana-Delgado, R., Karius, V. (2012). Sediment generation in modern glacial settings: grain-size and source-rock control on sediment composition. *Sedimentary Geology* 280, 80–92.
- Weeks, R., Laj, C., Endignoux, L., Fuller, M., Roberts, A., Manganne, R., Blanchard, E., Goree, W. (1993). Improvements in long-core measurement techniques: applications in palaeomagnetism and palaeoceanography. *Geophysical Journal International*, 114(3), 651-662.
- Weltje, G. J., and Tjallingii, R. (2008). Calibration of XRF core scanners for quantitative geochemical logging of sediment cores: Theory and application. *Earth and Planetary Science Letters*, 274(3-4), 423-438.
- Wilhelm, B., Vogel, H., Crouzet, C., Etienne, D., and Anselmetti, F. S. (2016). Frequency and intensity of palaeofloods at the interface of Atlantic and Mediterranean climate domains. *Climate of the Past*, 12(2), 299-316.
- Wu, L., Wilson, D. J., Wang, R., Yin, X., Chen, Z., Xiao, W., & Huang, M. (2020). Evaluating Zr/Rb ratio from XRF scanning as an indicator of Grain-Size variations of glaciomarine sediments in the Southern Ocean. *Geochem Geophys Geosyst*, 21, e2020GC009350. <https://doi.org/10.1029/2020GC009350>.
- Xu, B., Bianchi, T. S., Allison, M. A., Dimova, N. T., Wang, H., Zhang, L., Diao, S., Jiang, X., Zhen, Y., Yao, P., Chen, H., Yao, Q., Dong, W., Sui, J., and Yu, Z. (2015). Using multi-radiotracer techniques to better understand sedimentary dynamics of reworked muds in the Changjiang River estuary and inner shelf of East China Sea. *Marine Geology*, 370, 76-86.
- Zdanowicz, C., Smetny-Sowa, A., Fisher, D., Schaffer, N., Copland, L., Eley, J., and Dupont, F., (2012). Summer melt rates on Penny Ice Cap, Baffin Island: Past and recent trends and implications for regional climate. *Journal of Geophysical Research: Earth Surface*, 117(F2).

Zweng, M. M., and Münchow, A. (2006). Warming and freshening of Baffin Bay, 1916–2003. *Journal of Geophysical Research: Oceans*, 111, C07016.